# “Imaging diagnostics study for structure identification in MHD equilibrium and instability”

Ph.D. thesis

Submitted for the 3-year doctoral course

To

School of Physical Science

Department of Fusion Science

**‘SOKENDAI’**

**The Graduate University for Advanced Studies**


By

**Shishir PUROHIT**

(Year of submission: 2019)

Under supervision of
Prof. Yasuhiro Suzuki
Prof. Katsuji Ichiguchi
Prof. Yoshiro Narushima

# Abstract

Future Fusion grade plasma will be created in large and complex fusion reactors and MHD equilibrium reconstructions will be one of the important requirements which will prevail. MHD equilibrium reconstructions give the realization of the plasma boundary shape and mode structure, which are critical to the reliable fusion grade plasma. Identification of plasma boundary shape is a challenging problem, especially in the three-dimensional (3D) plasma geometry of the stellarator. Traditionally realized via indirect methods like kinetic fitting/ magnetic diagnostic etc. However such supportive diagnostic my not be too effective for fusion grade plasma environment. Alternatively by tomographic reconstructions from imaging diagnostic data describes plasma boundary shape and mode structures. This is near to a direct approach for realizing plasma boundary shape and subsequent MHD equilibrium reconstructions. Imaging diagnostic is expected to work efficiently in the fusion grade plasma environment. Tomographic reconstruction for fusion grade plasma from a large and complex device offers a lot of challenges like the partial viewing of the plasma from the imaging diagnostic which is a very critical issue. The motivation for this thesis is to design and develop a tomographic reconstruction method capable enough to recover the 3D plasma shape with the partial plasma viewing.

Currently the tomographic reconstruction is performed by either series expansion (SE), where the emission is expanded in terms of orthogonal functions/patterns, or by regularized least-squares approximations (RLS). The mentioned methodologies are having some serious limitations. The RLS is not applicable to the partial viewing/ restricted viewing geometries. On the other hand the SE takes geometry specific orthogonal patterns, for example Fourier –Bessel (FB) functions which are defined on a fixed shape. As the fusion grade plasma, it is expected to have an irregular shape so in order to employ SE with such functions flux surface information is required prior. Secondly SE assumes the emission along the field line is constant which reduces the efficiency of SE capability at the edge regions where the parallel and perpendicular component of transport are highly anisotropic. An orthogonal function is required which can withstand the requirements of the fusion grade plasma such as plasma shape independent, no prior requirements of flux surfaces, able to recover the plasma shape from restricted view.

The Laplacian Eigenfunctions (LEF) is adopted here in this thesis which fulfills the above-mentioned requirements and demonstrates a robust reconstruction procedure for tangential as well as radial viewing imaging diagnostic. The LEF is an orthogonal function which only depends on the distance between two points over the domain/plasma. Thus only requires rough information about the computation boundary, no need for flux surfaces. Interestingly can handle the highly anisotropic regions of the plasma. The reconstruction procedure is tested for different emission profiles and viewing geometries, full view and restricted view, for tangential viewing tokamak plasma. The reconstruction process is able to recover the 2D emission profile

efficiently. The LEF based reconstruction procedure is also applied to 3D plasma with radial and tangential viewing geometries. The LEF based reconstruction is able to recover the 2D emission profile for the Heliotron J device, radial viewing soft X-ray diagnostic, and successfully demonstrate the magnetic axis location. The results are similar to the Phillip-Tikhonov regularization method. The LEF reconstruction method is applied to the LHD 3D plasma. The LEF patterns, due to their 3D nature enabled the construction of the 3D plasma emission for LHD. LEF based reconstruction is performed and a general realization of plasma emission in 1D/2D and 3D is been achieved.

The key take away is, the Laplacian Eigen Function (LEF) based tomographic reconstruction is capable enough to recover the plasma emission shape in 1D/2D/3D. For the first time the LEF is successfully implemented for tokamak plasma / Heliotron plasma. The LEF was found capable enough to work well even in the restricted viewing geometry, where the standard method fails. This is one of the strongest points of this method. However the lengthy calculation, although easy and straight-forward, demand expensive computing.

A minor project was also carried out as a part of the Ph.D. project in which a new design for the soft X-ray tomographic diagnostic at Heliotron J (H-J) device was given in order to improve the capability of tomographic diagnostic, especially addressing the identification of the higher poloidal mode number structures in the plasma The current Heliotron J soft X-ray system (installed at toroidal angle, $\varphi = 45^{o}$) design harbors a triad of soft X-ray arrays looking to the plasma in a radial configuration from nearly $90^{o}$ degrees apart poloidally with effectively 60 lines of sight. The diagnostic is found to be capable of generating the 2D equilibrium emission profile. The major challenge was the identification of the higher mode structures. Most likely associated with the low number of arrays. The reconstruction was conducted with seven arrays for $m=2/n=1$. An improved image is received with a clearly identifiable mode structure, however the shape of mode structures was not impressive. Which is attributed to the flux compression at this toroidal location, $\varphi = 45^{o}$. A new location was identified, $\varphi = 0^{o}$, where the flux surfaces are triangular and flux compression is absent. Tomographic reconstruction for this new location with seven arrays is then performed, with simulated emission profile for $m=2/n=1$ and $m=3/n=2$. The resultant images clearly represent the input mode structures. The new design includes seven arrays looking to the plasma in the normal direction of the magnetic field, **B,** at $\varphi = 0^{o}$ location. This exercise was carried out by standard L2 type Philip-Tikhonov regularization and singular-value decomposition assisted least-squares fitting.

# Acknowledgment

Expressions come to stand still when it comes to acknowledgments. I find myself to be fortunate enough that 'The Life' has given me a chance to pursue research, in a field of my choice. None other than 'The Life', I wish to acknowledge first and foremost for allowing me to complete the task.

Words fall short and language becomes inadequate for expressing my heartfelt gratitude for Prof. Yasuhiro Suzuki, Prof. Katsuji Ichiguchi and Prof. Yoshiro Narushima my 'Reverend Teachers'. The constant support from Prof. Satoshi Ohdachi was one of the driving force to carry out my work for the Ph.D. project, without him the Ph.D. project would have been more than difficult. My extended thanks and gratitude are to Dr. S.Yamamoto and Prof. K. Nagasaki, Institute of Advanced Energy, Kyoto University for their constant support for my research work.

I am extremely grateful to Shri Y. Shankara Joisa (Rtd-SOG), Head, X-ray diagnostic and Prof. Dhiraj Bora (ex-DDG-ITER, ex-director IPR) for providing necessary official support for applying to the doctoral program at SOKENDAI. I am highly gratified to Dr. Joydeep Ghosh (IPR) and Dr. Malay Bikas Chowdhuri (IPR) for constantly encouraging me to contribute in plasma research.

I record my sincere thanks to Padma Shri Prof. Jitendra Nath Goswami (Principle investigator – Chandryaan-1, first Indian moon mission) and Prof. Santosh Vadawale (Physical Research Laboratory) for persistently motivating me for scientific research.

An acknowledgment for this work will not be completed without mentioning web platforms like Google, YouTube, Wikipedia, WolframAlpha, GitHub, StackOverflow and many more. They have been the best friends to support my work in many ways. I sincerely extend my gratitude to these web platforms.

Last but not least, I express my deep sense of gratitude to my family. To my father and mother for making me what I am today. I deeply express heartfelt thanks to my wife and son, who had to endure a great deal of inconvenience in these years. They were the strongest support throughout and raised my morale for addressing the complex nature of the researcher's life.

A special thanks to my tutor Shri. Junki Morimoto and H. Kawase for helping me in my Sokendai life.

**Shishir Purohit**

# Content


Abstract ii
Acknowledgment v
Content vi

**I Introduction 1**
1 Energy scenario 2
2 Nuclear Fusion 3
2.1 Plasma containment 5
2.2 Challenges with MCF 6
3 Plasma Instabilities 7
3.1 Internal and External instabilities 7
3.2 Pressure driven instabilities 8
3.3 Current driven instabilities 10
4 Plasma boundary shape 11
5 Experimental observations for PSB and MHD instabilities 12
6 Motivation 16
7 Outline of the thesis 17

**II Introduction to Tomography 21**
1 What is tomography 22
2 Plasma tomography 23
3 Mathematics of Tomography 24
3.1 Series expansion method 26
3.1.1 Expansion Functions 26
3.1.2 Fourier Bessel Functions (FB) 27
3.2 Discreet pixel method 28
3.2.1 Singular value decomposition 29
3.2.2 Regularizations-concept 30
3.2.3 Regularizations- types 31
3.2.3.1 Phillips-Tikhonov (PT) regularization 31
3.2.3.2 Minimum Fisher regularization 32
3.2.3.3 Maximum entropy regularization 34
3.3 Contribution matrix 35

**III Laplacian Eigen Functions 43**
1 Introduction 44
1.1 Laplacian Eigen Function (LEF) 44
2 Why LEF for plasma Tomography 49
3 Tomographic reconstruction LEF based 50

**VI LEF for Tokamak** **57**
1 Introduction 58
2 Viewing geometry 58
3 The reconstructions 61
3.1 Complete view 61
3.2 Restricted view 67
**V LEF for Heliotron J** **73**
1 Heliotron J device 74
2 Heliotron J – The Concept 75
2.1 Physics concept 75
2.2 Engineering design 78
3 Heliotron J – Diagnostics 79
4 Soft X-ray tomographic reconstructions 82
**VI LEF for LHD** **94**
1 Introduction 95
2 Large Helical Device (LHD) 95
3 Laplacian Eigenfunctions (LEF) 97
4 LEF capability estimation 99
5 LEF reconstruction 101
5.1 Complete view 102
**VII Conclusions** **109**
1 Conclusions 110
2 Future work 112
**Appendix**
**I New design of SX system for Heliotron J** **113**
1 Introduction 114
2 Reconstruction procedure 114
3 Design Modification 116
4 New Design 121
4.1 Design details 121

# Chapter I

# Introduction

Abstract:

The background, motivations and an abstract of the thesis are presented in this chapter. The realization of fusion-grade plasma boundary shape and plasma instabilities described via Magneto-hydrodynamic (MHD) for large plasma devices, tokamak/stellarator are the prime objectives of the study by employing the imaging diagnostics.

## 1. Energy scenario

A clean and sustainable energy source is the primary need for the survival of any economy. Global environmental concerns have added supplementary specifications for the future energy source. Some of the key characteristics of future energy source are listed as economical, environment-friendly and abundant in nature. Currently a wide variety of energy resources are employed, which are evaluated on the above-mentioned criterion, namely the petroleum, coal, biofuels, nuclear (non- renewable source) and solar, hydro, wind tidal (a renewable source) for power generation. Current scenario of global electricity generation and the projection trajectory is shown in figure 1, which predicts 12.4 trillion kilowatt-hours of electricity requirement, by 2050, and expected to meet with the current sources [1].

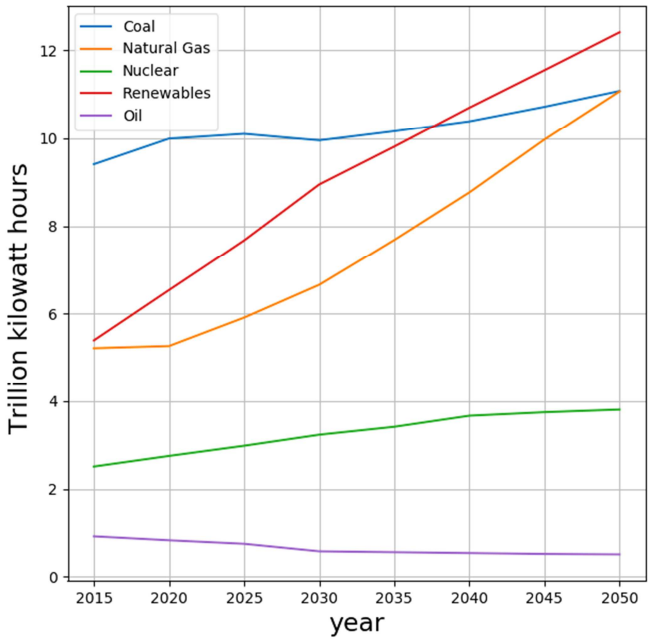


Figure 1: Global power projection (EIA 2017).

The projection trajectory suggests a strong and consistent increase in the renewable and natural gas-based power generation in the coming years, however the coal base power will remain almost stable. The coal contributes the largest share nearly ~40%, whereas the petroleum and natural gas combined contribute ~26% in the global

power production. Fortunately coal and petrol products are conveniently available in terms of extraction and processing along with considerable abundance. However these sources are significantly underlined for their contribution to environmental degradation and subsequent global warming. The $CO_2$ emission from a coal-fired plant is estimated to be nearly 970 $ton/GW_eh$, which is alarming [2]. The renewable sources presently contribute to ~23% of the power generation, and promises a bright future. They are more or less environment-friendly (accept hydro which affects the local eco-system). Mostly these resources have a significant or unlimited abundance. The prime concern associated with these sources is, the extraction technology which is expensive and needs complex instrumentation. Another prominent option is nuclear –fission. Where a heavy nucleus is split into two lighter nuclei. In this process a considerable amount of energy, majorly thermal, is released which is then used for generating power via steam. The energy extraction process is also complex for nuclear fission. Nuclear power does not emit much greenhouse gases to the environment but the waste product is extremely hazardous due to the residual radiation emission.

Every power source currently employed do have some limitations in terms of abundance, environmental impact, unit cost etc. In recent years the idea of power generation via nuclear fusion has picked up interest across the globe due to reporting of some exciting results[3–5]. Nuclear fusion is a process by which two light nuclei are fused to form a heavy nucleus. This process emits a significant amount of energy which is employed for the power generation. The characteristics associated with nuclear fusion are encouraging in terms of the environmental concerns and abundance of the raw material. Coming sections describe different aspects of nuclear fusion.

## 2. Nuclear Fusion

The Sun and stars are perfect examples of uncontrolled nuclear fusion where the hydrogen atoms majorly serve as the fueling agent. Hydrogen atoms fuse together under very high temperatures to form helium along with that a small amount of mass is converted into energy. The fusion happens when the hydrogen is in the plasma state.

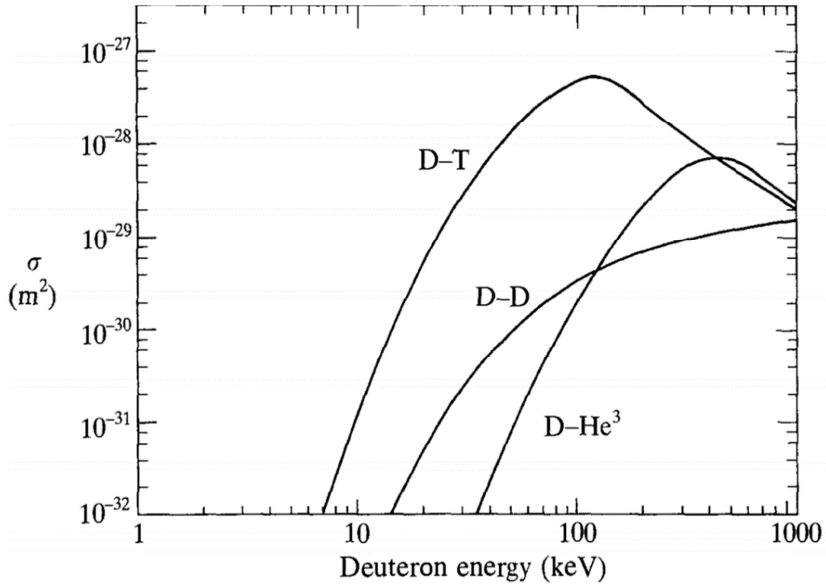


Figure 2: Reaction cross-section for different fusion reactions.

At such mentioned conditions, high temperature and densities, the mutually repulsive forces between the nuclei are overwhelmed by the temperature, density and pressure altogether in the plasma state and the nuclear fusion takes place. The nuclear reaction leading to nuclear fusion is given below along with the energy produced, in MeV.

$$H^1 + H^1 \rightarrow D^2 + \beta^+ + \upsilon + 1.44\,MeV \quad (1.1)$$

$$D^2 + D^2 \rightarrow He^3 + n^1 + 3.27\,MeV \quad (1.2)$$

$$D^2 + D^2 \rightarrow T^3 + H^1 + 4.03\,MeV \quad (1.3)$$

$$D^2 + T^2 \rightarrow He^4 + n^1 + 17.59\,MeV \quad (1.4)$$

The hydrogen-hydrogen fusion, equation 1.1, yields the lowest energy while the deuterium-tritium reaction, equation 1.4, is on the higher side of the energy scale. The reaction cross-section for these reactions is shown in figure 2 as the function of temperature [6]. The D-T reaction exhibits a relatively large reaction cross-section at a lower temperature, ~10 *keV*, whereas reactions for the light isotopes of the hydrogen require a higher temperature to perform the nuclear fusion. This facts

slightly relaxes the engineering requirements. Thus the D-T reaction, equation 1.4, turns to be a natural choice for the controlled nuclear fusion for any fusion device.

## 2.1 Plasma confinement

Harnessing nuclear fusion for power generation is an impressive idea but offers very stringent engineering and physics challenges. This majorly includes the confinement of the high density and temperature plasma, efficient extraction of the energy generated by the fusion, high temperature and corrosion-resistant materials, sophisticated diagnostic, operational complications etc. The confinement of the plasma is an important aspect of successful fusion operations. There are a couple of methods by which such plasma can be confined systematically for power generation, magnetic confinement fusion (MCF) [7] and inertial confinement fusion (ICF)[8] are two popular methodologies. The MCF is based on the fact that plasma has charged particles and when subjected to the magnetic field they follow the magnetic field lines. Thus ion movement trajectory can be governed, depending on the magnetic field geometry. The tokamaks, stellarator and reversed field pinch (RFP) devices are a couple of examples which follows MCF principle. The ICF is another approach for achieving the fusion where a small fuel pellet is heated by exposing to high power laser or ion beam. The heated outermost layers of the pellet explode outwards and generate a kind of inward-directed compression, implosion. This cages the heat at inner layers of the pellet. The compression pressure at the core/ inner-layers of the pellet, is when sufficiently large, offers the conditions of fusion. The preliminary energy release initiates a chain reaction leads to ignition. ICF concept offers a pulse of energy as it depends on the pellet while MCF energy generation can be continuous depending on the plasma duration. The most promising option for the realization of nuclear fusion is the MCF tokamak configuration and extensive work currently carried out all across the globe in this direction.

## 2.2 Challenges with MCF

The un-interrupted fusion reaction requires a consistently higher temperature environment, see figure 2, therefore any loss in temperature has to be avoided. One of the key tasks is to avoid a thermal loss to the wall containing the plasma, which is achieved by completely detaching the plasma from the wall with the introduction of a sufficiently strong magnetic field.

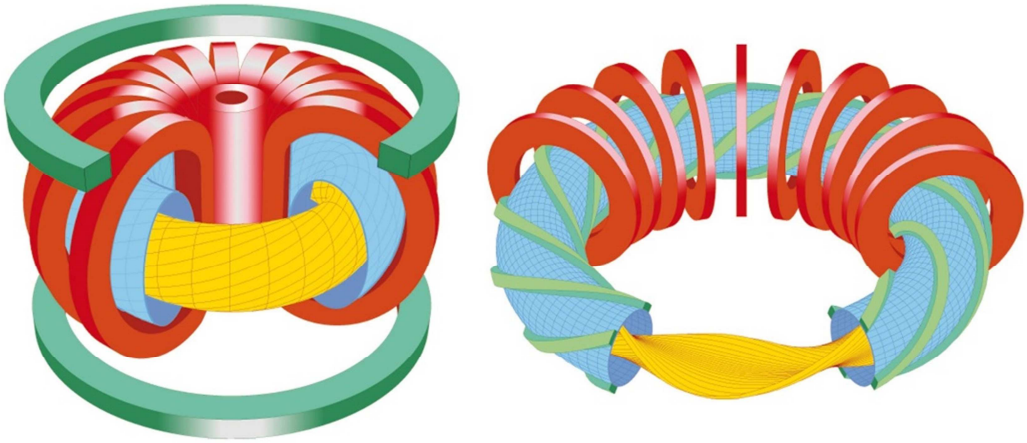

Figure3: Tokamak (left) and stellarator (right) devices.

The MCF devices are having a toroidal magnetic field generated from the external coils which enable the ionized plasma particle to follow the magnetic field lines and the plasma is contained under the Lorentz force. This Lorentz force prevents any movement in the perpendicular direction to the toroidal field. However the gyrating plasma particle will experience $B \times \nabla B$ force and exhibit some divergence which generates a subsequent electric field. This electric field drives the particles to drift outward. This drifting is addressed by introducing helicity in the field lines. For tokamak, figure 3(left), the particle drifting is checked by twisting the magnetic field lines. This is done by producing toroidal plasma current, via transformer action, which results in twisted flux lines. In the case of the stellarator devices, figure *3*(right), the typical design of the coils ensures the helical field without application of the toroidal current. Such kind of measures contains the plasma and guarantees minimal leakage of temperature and density to the wall. The thermal losses are not

only caused by the particle movement under the **E**x**B** force but also can happen due to the strong presence of Magneto-hydrodynamic (MHD) cooler edge regions, and influences the overall plasma stability and particle/impurity transport. Handling of such plasma instabilities instabilities which permits the interaction of the hot plasma core with the relatively is paramount for un-interrupted plasma operation.

## 3. Plasma Instabilities

The plasma instabilities can be defined crudely by the regions, within the plasma, where the distribution of the plasma energy is not the same as the background plasma[9]. This situation arises due to any alteration in the plasma characteristics such as temperature, density, electric fields, and magnetic fields. Plasma always harbors some amount of instabilities and the amplitude, at a given time, of these instabilities may differ with the plasma and machine condition. The amplitude of the instabilities place a considerable threat to the fusion plasma and the proper monitoring/mitigation of such phenomenon is of prime interest. The most commonly employed plasma description given by Magneto-Hydro-Dynamics (MHD), or Ideal MHD, considering plasma as a fluid of electrons and ions. Therefore, these instabilities are referred to as MHD instabilities. Under any prominent MHD instability the plasma termination or enhanced thermal transport is expected. MHD instabilities mostly appear as mode structures defined by poloidal mode number ($m$) and toroidal mode number ($n$)[10].

The MHD instabilities are classified by two basic characteristics the first is MHD instabilities is internal (fixed boundary) or external (free boundary) mode. The second characteristics are the driving source, pressure-driven or current driven, as the total MHD fluid energy is a function of the plasma pressure gradient ($\nabla p$) and the parallel plasma current[10][11].

### 3.1 Internal and External instabilities

The mode structure for internal MHD instabilities does not require any motion of the plasma-vacuum interface away from its equilibrium position. Furthermore if

the plasma-vacuum interface moves from the equilibrium position during an unstable MHD perturbation then the mode structure is referred to as an external mode.

## 3.2 Pressure driven instabilities

The pressure-driven MHD instabilities appear in the plasma due to a pressure gradient ($\nabla p$) which leads to the increase in the perpendicular current density ($\mathbf{J}_\perp$). These modes can exist in the absence of parallel plasma current and have a considerably shorter wavelength in the perpendicular direction to the magnetic field and longer wavelength along the magnetic field. The category of instabilities are further divided into two major classes namely interchange mode and ballooning mode [10].

The plasma is confined by the magnetic field lines and the plasma particles, which are ionized, moves along the field lines. The bending of the flux line in a toroidal system offers a unique situation if the field line, at the plasma-vacuum interface, bends inward to the plasma, opposite to the plasma pressure sign, a fluted kind of plasma surface appears.

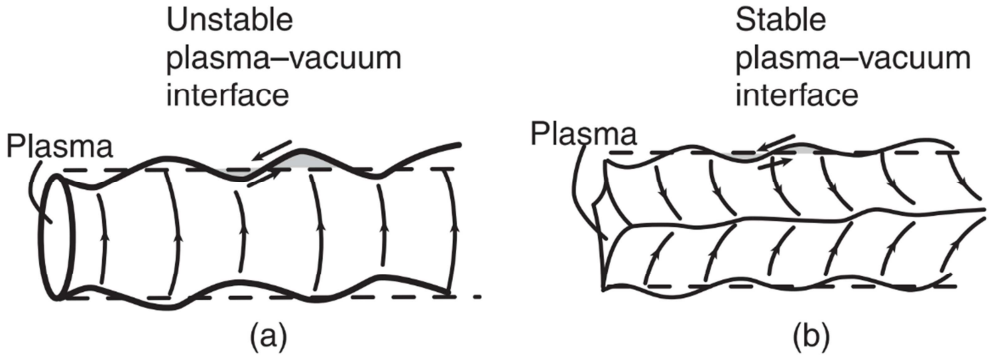


Figure 4: Unstable interchange mode scenario (a) and outward bending leads to a stable configuration (b).

The perturbation is constant along the field line but in the perpendicular direction to the field line the perturbation wavelength is short and is localized in the plasma radii. This mode is often referred to as localized interchange mode or the flute mode. Larger the inward bending of the line more unstable plasma, whereas the outward

bending of the field line adds to the stability of the plasma. The figure 4(a) represents the unstable state where the line bending is in the inward direction and the stable case figure 4(b), the line bending is outward direction, in line to the plasma pressure's expanding tendency. The ballooning mode is also an important instability which arises due to the good and bad curvature of the magnetic field. The perturbation here is not constant along the field line they change slowly along the line so that the perturbations can be concentrated only in the un-favorable curvature.

The strong ballooning mode makes plasma more unstable than the interchange mode.

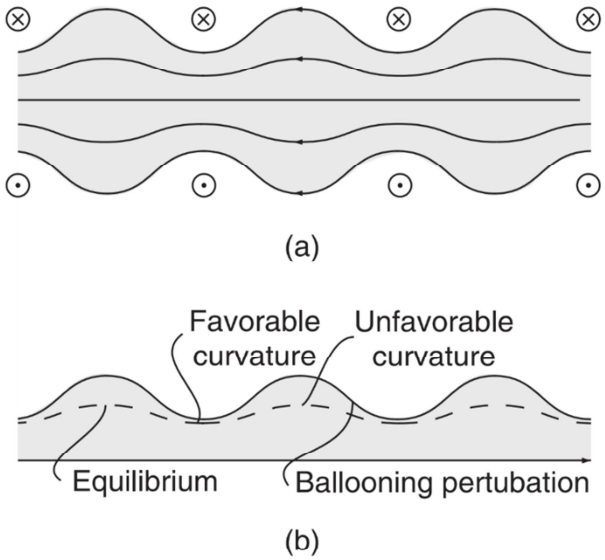


Figure 5: The toroidal cut of the plasma with plasma curvature (a) and the ballooning mode arising to the un-favorable curvature (b).

Referring to figure 5(a) is the toroidal cut of the plasma, the magnetic field with curvature is available, which is moving toroidally. The inward curvature is considered as favorable and outward as unfavorable curvature. The ballooning takes place at un-favorable curvature location in toroidal space as shown in figure 5(b). Generally this feature sets the limit for the highest achievable beta. The ballooning mode is commonly addressed by changing the magnetic shear or by increasing the magnetic strength[12,13].

## 3.3 Current driven instabilities

The current-driven MHD instabilities are associated with the parallel current ($\mathbf{J}_{\|}$) in the plasma. Under current-driven instabilities the plasma surface "*kinks*" into a helix, as shown in figure 6. The typical kinky shape has earned these instabilities name of Kink modes. The kink modes do have a long parallel wavelength whereas the perpendicular wavelength is somewhat macroscopic. Current-driven modes can be either internal or external depending on the location of the singular surface [6][10]. The internal kink mode is of the prime concern which can lead to a major disruption in the worst case.

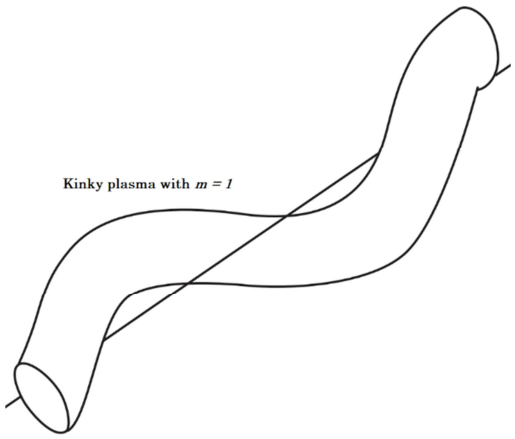


Figure 6: The kink instability for m= 1, long wave length.

At low beta the radial gradient of the parallel current at the plasma edge prompts external kink mode for high *m* mode numbers. Under this mode the kink structure is enhanced and leads to a ballooning kind of structure making the plasma highly unstable. At high beta plasma a significant ballooning shape is observed which make the plasma unstable even at the lower parallel current, lower than low beta safety limit [6][10]. The mitigation of such instability is important and a set of procedures are formalized for handling such events. This includes tighter aspect ratio which ensures the shorter kink mode wave-length, doctoring the current profile which is peaked at the center and extremely small gradient at the edge.

There are internal kink modes too which corresponds to the *m = 1*, and weaker than the external kink mode. A well-known example of internal kink mode is the saw-tooth oscillation often reported for different devices[6][10][14]. Commonly internal kink modes are stabilized via tighter aspect ratio and low current, this leads to a condition where the safety factor is high. This procedure is not effective at the RFP device as the safety factor is small, thus the stabilization is performed via broadening the current profile[14].

## 4. Plasma boundary shape

The plasma boundary shape (PBS) prescribes the magnetic flux surfaces and shafranov shift, is studied by flux surface information for a given plasma therefore PBS have a direct effect over the MHD plasma equilibrium and stability. Any violation of the MHD stability and equilibrium will greatly alter the exhaust of plasma power and particles to the walls, the effect of recycling neutrals, impurities, and edge turbulence on the core plasma. This peculiar character of the PBS makes it

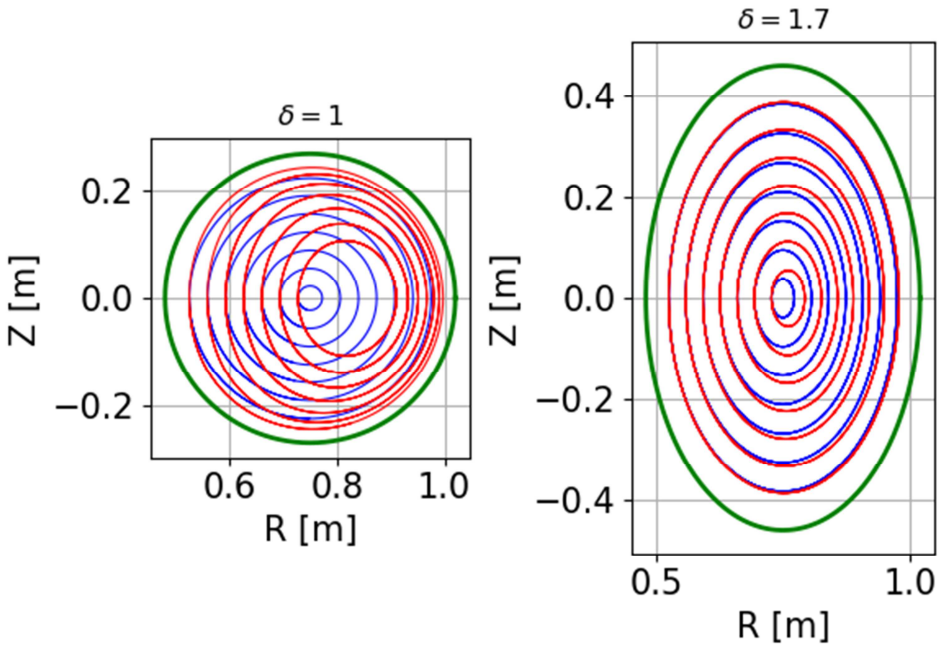


Figure 7. The flux surface for with low (blue) and high (red) beta plasma of circular tokamak (left) and elongated (right) shape for limiter (green) configuration is shown

extremely important to have a proper understanding of the plasma boundary shape. PBS studies mainly include a precise description of the plasma equilibrium profiles in *2-D* and sometimes *3-D* in case of stellarator device. The direct measurement of the plasma boundary shape is very difficult. Usually the MHD equilibrium reconstruction (estimation of plasma flux surface and equilibrium profiles) is estimated mathematically by coupling the kinetic profile measurements along with the magnetic diagnostics information[15,16].

Referring to the figure 7, the plasma flux surfaces for two different elongated plasma ($\delta$ = 1 circular and $\delta$ = 1.7 elliptical) with low beta (blue) and high beta (red) configuration are shown. The limiter like object, green, is shown for reference. This kind of changes is required to be known for a given plasma. The flux-surface under different configuration and geometry changes considerably and subsequently affect the equilibrium and stability of the plasma. In principle MHD instabilities and plasma boundary shape both are potential enough to affect the MHD plasma equilibrium and stability, thus proper understanding including the mitigation (of instabilities) is of prime importance for fusion-grade plasma.

## 5. Experimental observations for PBS and MHD instabilities

The experimental study of PBS and instabilities is carried out via sophistic diagnostic supported with strong numerical tools. A range of diagnostic like magnetic probes, soft X-ray, vacuum ultra-violate is often employed for these tasks. The magnetic probes and soft X-ray are extensively used to study MHD instabilities, more specific the mode structures. The typical output from the analysis of magnetic diagnostic for Large Helical Device (LHD) plasma is shown in figure 8, along with heating power and beta. The magnetic fluctuation for different mode structure is shown from 8*(e-f)* and the power spectrum of magnetic fluctuations are represented in 8*(g)* respectively[17]. The strong presence of the MHD instabilities affects the plasma equilibrium and magnetic diagnostic is a vital tool to understand the MHD instabilities within the plasma.

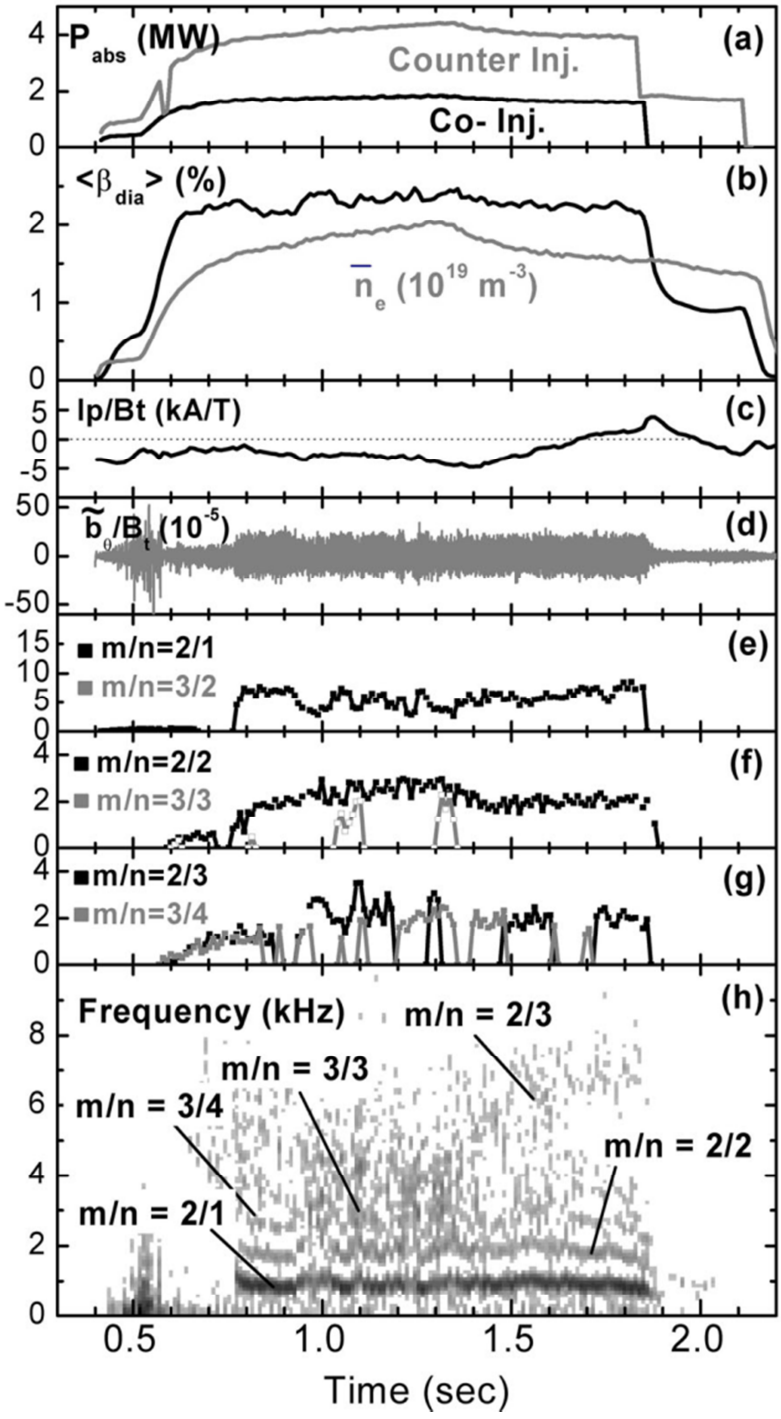


Figure8: Temporal changes of (a) absorbed heating power, (b) volume < $\beta$> value and line averaged electron density, (c) plasma current, (d) magnetic fluctuation, amplitudes of (e) m/n = 2/1, 3/2, (f) 2/2, 3/3, (g) 2/3, 3/4 and (h) power spectrum of magnetic fluctuation in the high-beta discharge with small plasma current.

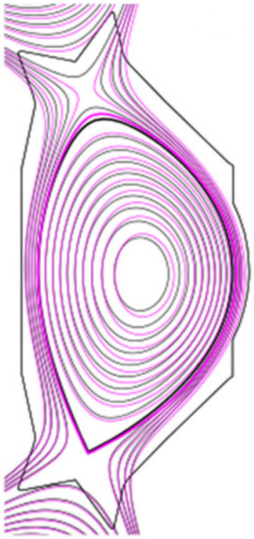

Figure 9. Plasma boundary shape and subsequent flux surfaces estimation from magnetic diagnostic, magnate and from kinetic fitting, in black.

The magnetic diagnostic along with the kinetic E-fitting of the plasma profiles gives the plasma boundary and shape of the flux surfaces. One such example is shown here for the EAST device[18]. The flux surfaces from the magnetic diagnostic, in magenta, and from the kinetic fitting, in black, are shown in figure 9. The plasma boundary shape and the flux surfaces are properly recovered from the magnetic diagnostic. It can be seen that both kinetic fitting and the magnetic data information nearly matches with each other.

The tomographic reconstruction from the imaging diagnostics offers an alternative approach for studying the plasma boundary shape (PBS) and the MHD instabilities[19]. Tomography is a process by which the line integrated emission data from the imaging diagnostic is transformed into local emission. The imaging diagnostics data are magnetic free information, holds important information about the hot plasma core/edge, offers a versatile platform to understand the plasma in a wider context. Figure 10 shows an example of the plasma boundary shape realization from tomographic reconstructions for COMPASS device[20]. Figure 10 (b) shows the line integrated visible image of the EDICAM imaging diagnostic and figure 10 (a) is the tomographic reconstruction. The plasma boundary shape is conveniently realized.

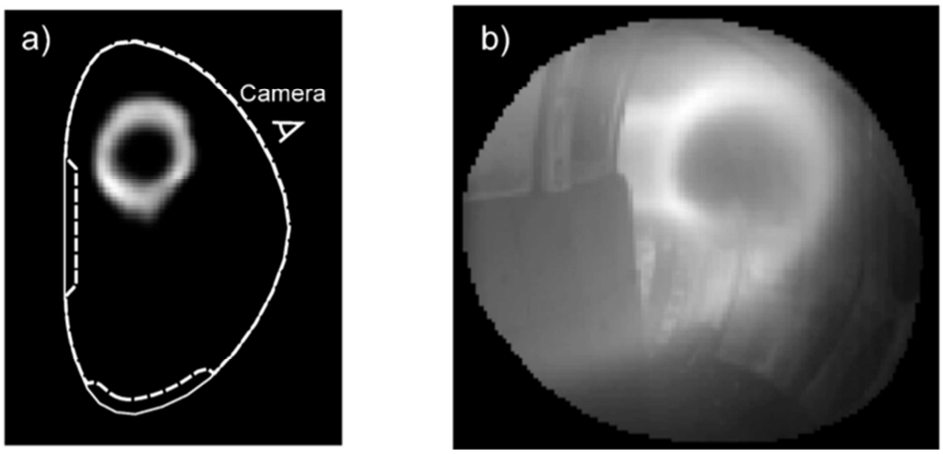


Figure 10. Plasma boundary shape recovery (a) from line integrated visible camera image (b) for COMPASS device.

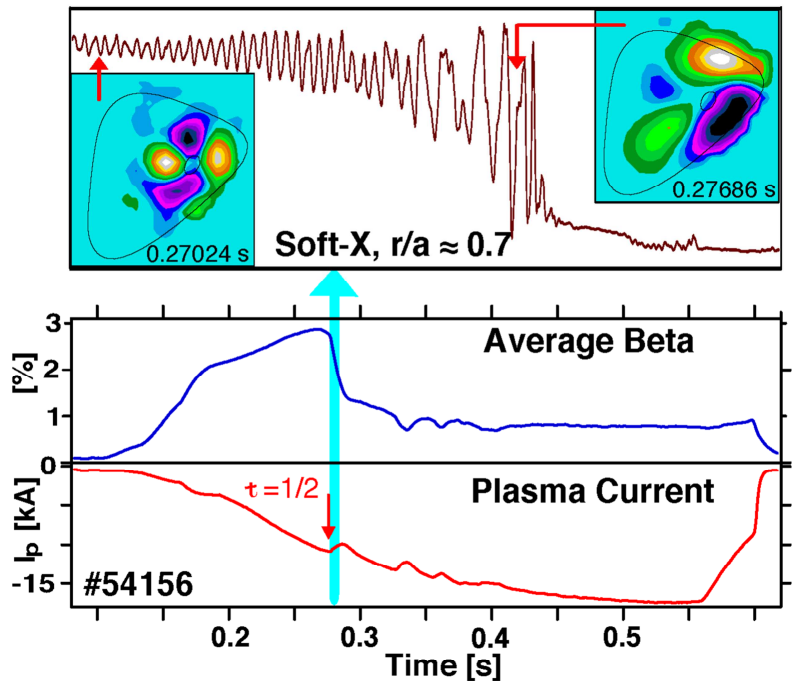


Figure 10: Tomographic reconstruction for the tearing modes leading to plasma thermal collapse.

The soft X-ray tomographic (SXT) reconstruction, as shown in figure 11, for the W7-AS device[21]. Where the mode growth is leading to the thermal collapse of the plasma is represented. The external rotational transform was scanned under OH-current ramp-up scenario for high beta plasma. The MHD mode $m$=2/$n$=1 appears

inside the plasma in the very beginning but as soon as the mode is pushed towards the gradient region, towards the edge. The mode grows and leads to a thermal collapse of the plasma. The realization of the mode and its growth is effectively understood via SX tomography.

## 6. Motivation

The estimation of the plasma boundary shape for fusion-grade plasma produced in large devices possesses a set of challenges. The large plasma devices are expected to have a huge array of peripheral systems like magnetic coils, heating and pumping systems. This situation increases the constraints in terms of the diagnostic installation for viewing the plasma properly, full plasma cross-section. Neutron flux from the fusion plasma will add to such complexities. Along with that the operation of traditional diagnostic like magnetic diagnostic, Thomson scattering or electron cyclotron emission (ECE) may not be efficiently possible. However the imaging diagnostic may still be operational efficiently with proper care, shielding. With such a contested scenario, for large plasma devices, the imaging diagnostic may not be able to view the full plasma, only the part of the plasma will be available in the field of view of the imaging diagnostic. This kind of viewing situation is referred to as a restricted viewing case. The tangential viewing imaging diagnostics will be affected more due to such constrained viewing. Along with the restriction in the plasma viewing the fusion-grade plasma cross-section shape will not be very simple, not a simple circle or ellipse or D-shape, it is expected to be complex. Especially for the 3D plasma systems like stellarator or heliotron.

The tomographic reconstruction for this advanced plasma will be challenging. The traditional methods of tomographic reconstruction, like the global orthogonal expansion patterns namely Fourier –Bessel (FB) functions are successful enough to determine the local emission profile from the imaging diagnostic, in specific to the circular cross-sections [22]. FB functions do have a limitation, when applied to the non-circular cross-section plasma due to some inherent properties like the domain dependency, depends on the plasma cross-section[23]. The other famous

reconstruction approach is the least square approximation assisted with regularizations. However being a very effective method regularization assisted Least square approximation is not capable to handle the restricted view[24]. Thus a tomographic reconstruction method is required which can recover the plasma boundary shape for a fusion-grade plasma for a bigger and more complex plasma device, especially with the constrained view and can withstand with the non-conventional plasma shapes. This is the basic motivation behind the work presented here in this thesis.

## 7. Outline of the thesis

The thesis is divided into 7 chapters which include the introduction and the conclusions with one appendix. The first chapter establishes the basic motivation and gives a brief overview of the scope of this PhD thesis. The second chapter 'Introduction to tomography', describes the different aspect of tomographic reconstructions and challenges. The chapter also explains different approaches to have tomographic reconstruction and its shortcomings. The third chapter 'Laplacian Eigen Functions' introduces the Laplacian Eigenfunctions(LEF) in general and gives a detailed account of the LEF based tomographic reconstruction procedure. The fourth chapter 'LEF for Tokamak', in this chapter the LEF based tomographic reconstruction is explained for the symmetrical, tokamak plasma, and the viewing geometry is tangential to the magnetic field. The fifth chapter 'LEF for Heliotron J' address to the reconstruction for the experimental soft X-ray data set for 3D Heliotron J plasma where the viewing geometry is perpendicular to the magnetic field direction, with the objective of the realization of the magnetic axis location. The sixth chapter 'LEF for LHD' explains the tomographic reconstruction for the tangential viewing 3D plasma of LHD. This is followed by conclusions, chapter seven. The appendix addresses the minor project in which a new Soft X-ray diagnostic design is being discussed for the Heliotron J device. The new design holds a better performance in terms of the realization for the mode structures in the plasma via tomographic reconstructions.

## References

[1] Anon EIA - Annual Energy Outlook 2018

[2] White S W and Kulcinski G L 2000 Birth to death analysis of the energy payback ratio and CO2 gas emission rates from coal, fission, wind, and DT-fusion electrical power plants *Fusion Eng. Des.* **48** 473–81

[3] Wesson J 1999 *THE SCIENCE OF JET*

[4] Flakus F-N, Cleveland J C and Dolan T J *Nuclear fusion: Targeting safety and environmental goals Analyzing fusion power's potential for safe, reliable, and environmentally friendly operation is integral to ongoing research*

[5] Rebut P-H 1992 The JET preliminary tritium experiment *Plasma Phys. Control. Fusion* **34** 1749–58

[6] Wesson J and Campbell D J 2011 *Tokamaks* (Oxford University Press)

[7] Ongena J, Koch R, Wolf R and Zohm H 2016 Magnetic-confinement fusion *Nat. Phys.* **12** 398–410

[8] Craxton R S, Anderson K S, Boehly T R, Goncharov V N, Harding D R, Knauer J P, McCrory R L, McKenty P W, Meyerhofer D D, Myatt J F, Schmitt A J, Sethian J D, Short R W, Skupsky S, Theobald W, Kruer W L, Tanaka K, Betti R, Collins T J B, Delettrez J A, Hu S X, Marozas J A, Maximov A V., Michel D T, Radha P B, Regan S P, Sangster T C, Seka W, Solodov A A, Soures J M, Stoeckl C and Zuegel J D 2015 Direct-drive inertial confinement fusion: A review *Phys. Plasmas* **22** 110501

[9] Lehnert B 1972 *BASIC FEATURES OF PLASMA INSTABILITIES*

[10] Freidberg J P 2014 *Ideal MHD* (Cambridge University Press)

[11] Stacey W M and Petrie T W 2000 The role of thermal instabilities in limiting the density in DIII-D *Phys. Plasmas* **7** 4931

[12] Webster A J, Szwer D J and Wilson H R 2005 The stability of ballooning modes in tokamaks with internal transport barriers *Phys. Plasmas* **12** 092502

[13] Hameiri E and Chun S-T 1990 Stability of ballooning modes in a rotating plasma *Phys. Rev. A* **41** 1186–9

[14] Campbell D J, Start D F H, Wesson J A, Bartlett D V., Bhatnagar V P, Bures M, Cordey J G, Cottrell G A, Dupperex P A, Edwards A W, Challis C D, Gormezano C, Gowers C W, Granetz R S, Hammen J H, Hellsten T, Jacquinot J, Lazzaro E, Lomas P J, Cardozo N L, Mantica P, Snipes J A, Stork D, Stott P E, Thomas P R, Thompson E, Thomsen K and Tonetti G 1988 Stabilization of sawteeth with additional heating in the JET tokamak *Phys. Rev. Lett.* **60** 2148–51

[15] Miyata Y, Hahn S H, Suzuki T, Ide S, Chung J, Bak J G and Ko W H 2014 Validation of plasma shape reconstruction by Cauchy condition surface method in KSTAR *Phys. Plasmas* **21** 032502

[16] Wang F, Nakamura K, Mitarai O, Kurihara K, Kawamata Y, Sueoka M, Sato K, Zushi H, Hanada K, Sakamoto M, Idei H, Hasegawa M, Kawasaki S, Nakashima H and Higashijima A 2007 Plasma Shape Reconstruction of Spherical Tokamak using CCS Method **2** 1095

[17] Sakakibara S, Watanabe K, Yamada H, Narushima Y, Toi K, Ohdachi S, Yamaguchi T, Narihara K, Tanaka K, Tokuzawa T, Ida K, Kaneko O, Kawahata K, Komori A and Group L E 2006 Effects of Resonant Magnetic Fluctuations on Plasma Confinement in Current Carrying high-β Plasmas of LHD *Plasma Fusion Res. Regul. Artic.* **1** 3

[18] Li G Q, Ren Q L, Qian J P, Lao L L, Ding S Y, Chen Y J, Liu Z X, Lu B and Zang Q 2013 Kinetic equilibrium reconstruction on EAST tokamak *Plasma Phys. Control. Fusion* **55** 125008

[19] Purohit S, Suzuki Y, Ohdachi S and Yamamoto S 2018 Improved design for

Heliotron J soft X-ray diagnostic for tomographic reconstruction studies *Rev. Sci. Instrum.* **89** 10G102

[20] Odstrčil M, Mlynář J, Weinzettl V, Háček P, Odstrčil T, Verdoolaege G, Berta M, Szabolics T and Bencze A 2014 Plasma tomographic reconstruction from tangentially viewing camera with background subtraction *Rev. Sci. Instrum.* **85** 013509

[21] Weller A, Geiger J, Zarnstorff M, Sallander E, Klose S, Werner A, Baldzuhn J, Brakel R, Burhenn R, Ehmler H, Gadelmeier F, Giannone L, Hartmann D, Jaenicke R, Knauer J, Laqua H P, Nührenberg C, Pasch E, Rust N, Speth E, Spong D A, Wagner F and Wenzel U 2001 Investigation of the β-Limit in the W7-AS Stellarator *19th Fusion Energy Conference 14-19 October, Lyon, FRANCE* p EX/S3-1

[22] Nagayama Y 1987 Tomography of *m* =1 mode structure in tokamak plasma using least□square□fitting method and Fourier–Bessel expansions *J. Appl. Phys.* **62** 2702–6

[23] Ohdachi S, Yamamoto S, Suzuki Y and Purohit S 2019 Tomographic inversion technique using orthogonal basis patterns *Plasma Fusion Res.* **14** 3402087

[24] Tingfeng M 2012 *Development of High-speed Vacuum Ultraviolet Imaging Camera System for High-temperature Plasma Diagnostics* (The Graduate University for Advanced Studies, Japan)

# Chapter II

# Introduction to Tomography

Abstract:

Chapter introduces the concept of the tomography via line integrated data obtained from the imaging diagnostic to study Magneto – Hydro - Dynamic (MHD) equilibrium and stability. An overview of different tomographic reconstruction methodologies and their respective characters are presented here.

## 1. What is tomography?

The word tomography is originated from the Greek language where *Tomo* means to cut. The computed tomography was introduced by Godfrey Hounsfield and Allan Cormack in 1972. The work was very revolutionary in terms of medical diagnosis and earned the Nobel Prize in Physiology or Medicine in 1979 [1,2]. The tomography, or computed tomography, is a non-destructive testing procedure where a number of the line integrated measurements (i.e. projections) are employed to reconstruct internal structures, *2D* or *3D*, of an object. A very common example of tomography is a CT scan of human body parts. The output of the CT scan is the 3D image of the internal structures of the body, which is very helpful in diagnosing any abnormal feature within, especially in comparison to the available techniques like general X-ray.

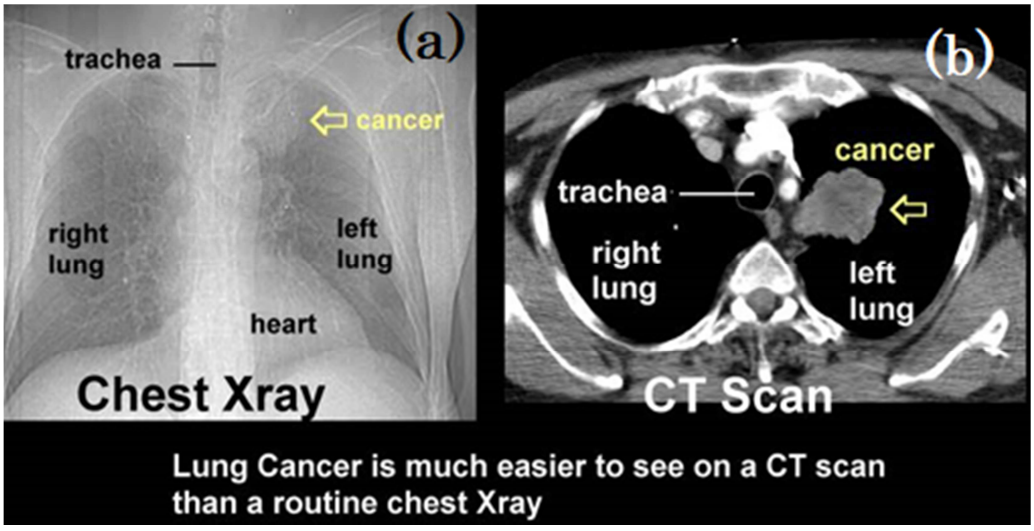


Figure 1: Medical imaging results from normal X-ray exposure (a) is not efficient enough to demonstrate the cancer affected cells, whereas the CT scan image (b) convincingly stablishes the presence of cancer cells.

Referring to figure 1(a) [3] which represents a general X-ray of a human chest where cancer cells are shown, yellow arrow. The image quality is not sufficient to conclude the presence of cancer in the body. In contrast to general X-ray the CT scan image, figure 1(b), which is *3-D* in nature, offers clear visualization of the cancer cells at the lungs. This kind of visualization greatly affects the treatment of any required medical

assistance. Along with medical imaging tomography is hired for the industrial and scientific project too, namely Ocean acoustic tomography[4], Ultrasound computer tomography[5] etc.

## 2. Plasma tomography

Understanding the plasma interior has always been a priority for plasma physicist to keep plasma equilibrium and stability at a high plasma temperature and density. Tomography is one of the important tools to extract plasma interior information from experimentally obtained line integrated measurements in different wavelengths, addressing different aspects of the plasma. The soft X-ray and VUV reconstruction have been successful in prescribing plasma behavior under different plasma operation regimes[6–8]. Unlike medical imaging, the plasma tomography object, the plasma, changes with time and it is not possible to have measurements from all possible direction at a given time. Thus sometimes the plasma tomography is referred to as limited angle tomography, due to the fact that the number of line integrated measurements are limited, limitation from the plasma and machine conditions.

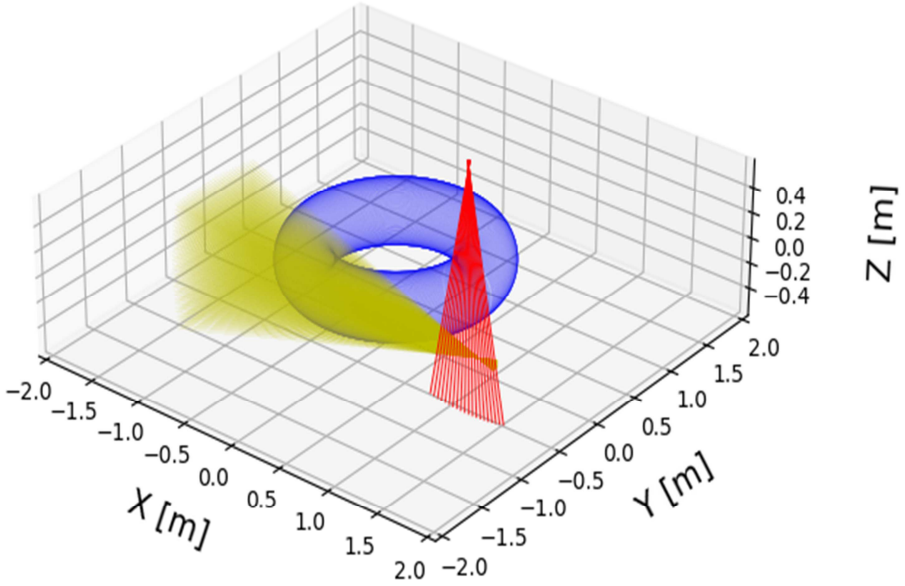


Figure 2: The perpendicular view (red) and the tangential viewing (yellow) geometry for a circular tokamak case.

Plasma tomography is divided majorly into two major class considering the detector - plasma viewing geometry, refer to figure *2*. The detector views the plasma in the perpendicular direction to the magnetic field direction then it is referred here as normal viewing tomography (NV), viewing geometry is shown by red. The detector system for NV is mostly linear array and multiple detector arrays are required for successful tomographic reconstruction. Whereas the detector viewing the plasma tangential to the magnetic field direction then it is termed as tangential viewing tomography (TV), viewing geometry is shown by yellow. TV, generally, employs 2D detector arrays for the plasma emission measurements. The TV is relatively new techniques which perform better than NV. The reason lies in the fact that the tomography is performed on the line integrated signals not with the local measurement. As a consequence, plasma fluctuations having relatively small poloidal wavelengths are averaged out in the process of integration, the simple reason is that there are several wavelengths on the line of sight. This point is critical for the NV configuration as the integration is done in the perpendicular directions. The TV configuration, the line integration is along the magnetic field. The fluctuations tend to have very long wavelengths in the direction of the magnetic field. Thus the phase of the fluctuation does not change and consequently no averaging takes place.

## 3. Mathematics of Tomography

The mathematical treatment of the tomographic problem is the most important part of tomographic reconstructions. The line integrated signal from plasma measurements is summation of all the plasma emission seen by the detector along the line of sight. The mathematical representation of this expression is shown in equation 2.1 and subsequently in 2.2. The $E_1$, $E_2$… $E_n$ is the local emission seen by the detector from the plasma and $A_1$, $A_2$, $A_3$ ….$A_n$ is the weight of the particular location for from where the emission E's is appearing.

$$S = A_1E_1 + A_2E_2 + A_3E_3 \dots\dots\dots\dots\dots A_nE_n \qquad (2.1)$$

$$S = \sum_{j=1}^{n} A_j E_j \tag{2.2}$$

$$S = AE \tag{2.3}$$

The physical representation of this mathematical analogy is shown in figure 3. Where different '*j*' location is represented by '*'.All the measurements corresponding to different detectors will constitute a matrix of S, line integrated data, and subsequently A and E, equation 2.3, where '*j*' runs on the number of location *0* to '*n*'. The S values are achieved from the experiments while A is referred to as contribution matrix, is calculated prior to the tomographic reconstruction.

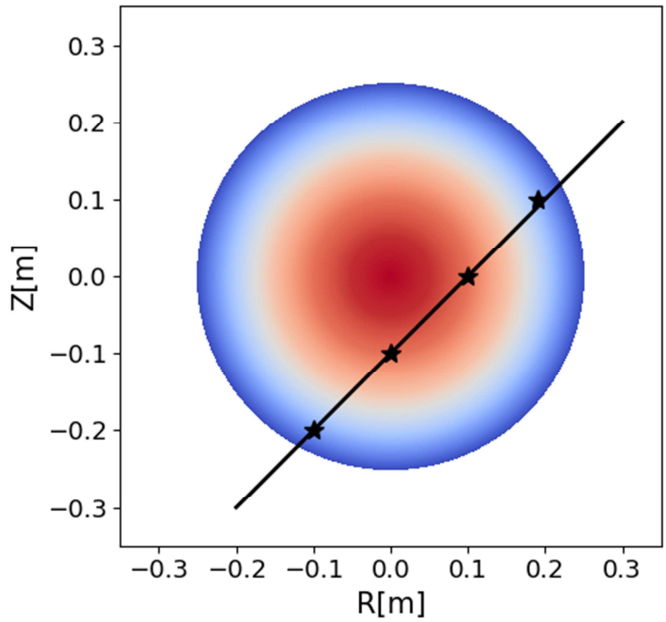


Figure 3: The line integrated SX signals(*S*) are the summation of the local emission ($E_j$) and the weight factor ($A_j$).

The tomographic reconstruction is the process to recover of all the E's that is the local emission information from line integrated measurements, S and the contribution matrix, A. Very straight forward method is treating the experimental measurement (S) with the inverse of the contribution matrix($A^{-1}$). As discussed earlier the plasma tomography is a limited angle tomography, which means that the measurements are limited in number so weight estimation can be made for the limited

number of locations. This fact makes the contribution matrix spars, mostly having zeros or less information in the contribution matrix. These facts make the tomographic reconstruction as a mathematically ill-posed problem[9–11] and the direct inversion cannot be performed. The ill-posedness is typically a situation whereas matrix X (or $X^T X$) is having many small eigenvalues or singular values[12], thus in order to have a well- behaved solution it is necessary to regularize inversion expression.

There are two major approaches for the tomographic reconstructions. First one is series expansion method and second is the discrete pixel method or the least square approximation assisted with the regularizations.

## 3.1 Series expansion method

The series expansion schemes consider the fact that the local emission can be approximated by an expansion on a suitable set of basis functions, equation 2.4. Where $e_k$ is the expansion parameter and $b_k$ is the basis functions and $k$ is the expansion id.

$$E = \sum e_k b_k \tag{2.4}$$

$$S_i = \sum \grave{A_j} e_k \tag{2.5}$$

$$\grave{A_j} = \iint A_j b_k \tag{2.6}$$

So the contribution matrix can be redefined by equation 2.6 where it is directly associated with the basis function.

### 3.1.1 Expansion functions

A range of basis functions are employed for tomographic reconstruction local basis functions, global basis functions, and natural basis functions. The local basis functions (LBF) are defined on a grid and poses some kind of shape so that the Emissivity, E, can be described efficiently. The functions can be square-shaped which is a very simple approach[13]. A classic example of LBF is a rounded corner pyramid

which overlaps halfway with the neighboring basis functions[14]. At this situation it is convenient to define emissivity in a continuous and smooth manner. The global basis function (GBF) was proposed by Cormack in 1963 discussing the computed tomography for medical applications[15]. Where GBF are constituted by of *sine* and *cosine* function, basically circular harmonics, in the poloidal and Zernike polynomials or Bessel functions for toroidal directions[16–18]. The circular nature of GBF facilitates a clear description of the circular cross-section plasma, tokamak[7,17]. However the higher-order harmonics fails to define emissivity fine structures for non-circular plasma, like D-shaped or elongated plasma, thus limits the applicability of this method for the complex plasma shapes. The Natural basis functions (NFB) are not orthogonal in nature rather then they are more associated with viewing geometry. So with NFB complex viewing geometry or improper coverage will be difficult to handle. The selection of the basis function and its number is very important for the tomographic reconstruction as it directly influences the computational time and accuracy of the final results. The LBS function is most commonly employed function for the plasma tomography due to the fact that LBS is quite convenient with arbitrary sightline distributions.

### 3.1.2 Fourier–Bessel functions (FB)

Traditionally the reconstruction from the global orthogonal pattern, such as Fourier–Bessel functions, are employed extensively in the past[19]. The success of these global orthogonal patters lies in the fact that with the limited information, the emission profile is recovered successfully, especially for circular cross-section plasma. These patterns also satisfy the boundary conditions like the Dirichlet's boundary condition, patterns are zero at the boundary. Fourier–Bessel functions (FB) are defined by the equation 2.7. The FB has a fast decaying nature. The typical patterns FB for the circular cross-section are shown in figure 4.

$$\psi_l^m = e^{im\theta} J_m(\epsilon_m^l \rho) \qquad (2.7)$$

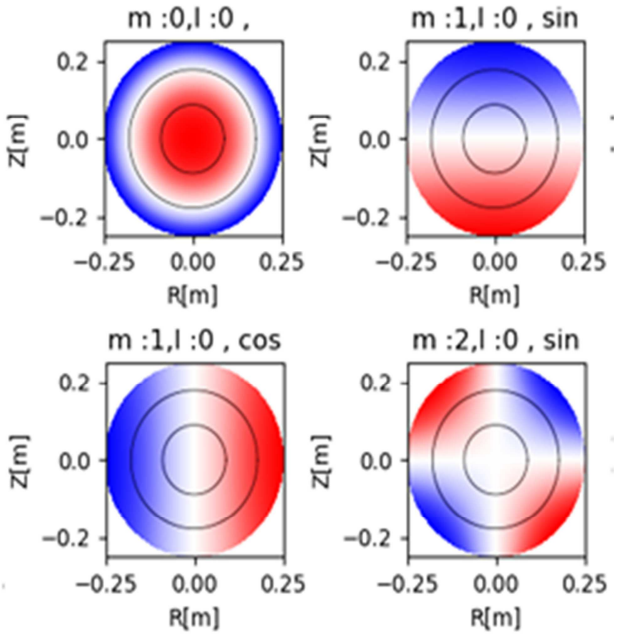


Figure 4: Different Fourier–Bessel functions corresponding to different *m,l* and *sine / cosine* values, circular cross-section.

The FB patterns are orthogonal when aligned to the flux surface, for circular cross-sections, gives robust reconstruction results for the magnetic island structures too. Figure 5 shows the FB pattern calculated for the Heliotron J plasma cross-section at $\varphi = 45^{o}$ degree. For the non-circular cross-sections FB patterns are estimated over the flux surface. The reason is to achieve the near-orthogonality of the functions and secondly to accommodate the noncircular aspect of the plasma. Since the FB are defined on the circular domain, a non-circular reconstruction can only be possible when the patterns are calculated over the flux surface, flux surface aligned patterns[20].This is a big limitation of the FB as the availability of the flux surfaces may not be there for every time step to which the reconstruction is attempted.

## 3.2 Discreet pixel method

Discreet pixel method (DPM), sometimes also referred as finite element method, considers the discretization of the reconstruction area into small subregions commonly termed as ‘pixel’ and emission within this pixel is assumed to be constant, which is a strong assumption. In other words the emission information is restricted by

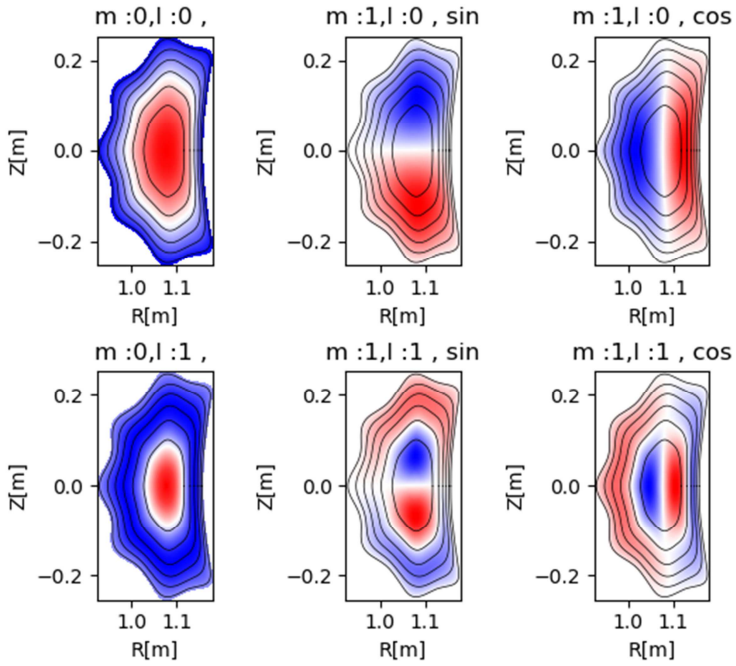


Figure 5: Different Fourier–Bessel functions corresponding to different *m*, *l* and *sine/cosine* values, for Heliotron J.

the pixel shape and size. The quality of the image now directly depends on the shape and size of the pixel. The pixel can have different shapes like square, rectangular, circle or hexagonal depending on the requirements, however for plasma tomography square or the rectangular shape is commonly used.

As discussed the ill-posedness of the contribution matrix, having many small eigenvalues or singular values, so regularization is required for a well-behaved solution. The well-behaved solution can be achieved by ignoring less important eigenvalues. The analysis of Eigenvalues of the matrix gives in-depth information[18], however the singular value decomposition (SVD) is a better option to employ for ill-posed problems analysis[21].

### 3.2.1 Singular value decomposition

The singular value decomposition is a very standard way of eliminating the small singular values which are related to smaller eigenvalues in the contribution matrix. This elimination regularizes the inversion problem. The cutoff level of the singular values is set by the user and depend on the range of singular values and

prevalent noises in the measurements[12,21]. The Kaczmarz method is one of the famous example of truncation via SVD. The SVD gives the Least-Square-Error solution for equation 2.2 when the problem is overdetermined and minimum – norm solution for the underdetermined problem[12,21,22]

### 3.2.2 Regularizations-concept

Regularization procedure is adopted when the experimental measurements, S and the contribution matrix, A, contain insufficient information for physically meaningful reconstruction, for example MFE diagnostics. Under regularization, the problem is converted in a different form which does not have smaller singular values or the eigenvalues, this relaxes the ill-posedness and a smooth result is obtained. The conversion is done by some prior information about the expected plasma emission profile, like no emission beyond vacuum. As said plasma tomography is a limited angle tomography so the information of the plasma measurement between two lines of sights (LOS) is somewhat missing. So the prior information fills this gap of information with-in two measurements and leads to a meaningful tomographic reconstruction. The prior information is added to the problem by a desired property of the plasma emission by an objective or penalty functional, PF (E), where E is in discrete form. The equation 2.2 can be re-written in the following form, equation 2.8.

$$J(E) = \gamma PF(E) + \|S - AE\|^2 \qquad (2.8)$$

Equation 2.8 is the mathematical representation of the tomographic reconstruction via regularizations. The γ is the regularization parameter which decided the amount of the regularization for a given tomographic reconstruction problem. The estimation of regularization parameter is carried out by the L-curve[23], predicted sum of squares (PRESS)[24], or Generalized Cross-Validation (GCV)[25][6]. Once the regularization parameter and the penalty function is known, a meaningful reconstruction is performed. The optimized solution that is *E*, will be achieved by the constrained minimization of equation *2.8*. At the minimum value of equation *2.8* the corresponding *E* will be the optimum solution.

### 3.2.3 Regularizations- types

There is a range of regularization procedures depending on the definition penalty function (PF). PF can be linear or non- linear function of the emission, *E*. The linear category of the PE is further classified into L1 and L2 type of regularizations. The L1 type, also known as Lasso regularization, of PF considers are the sum of the absolute values of emission *E* for penalization. The L1 regularization completely removes non-essential components, which results in to a sparse result[26]. L2 regularization employs the sum of the squares of the emission, $E^2$ for penalization. The non-essential components are not removed under L2 regularization unlike the L1. The result from L2 still holds non-essential components but higher components are penalized more in comparison to the L1.

#### 3.2.3.1 Phillips-Tikhonov (PT) regularization

The Phillips-Tikhonov (PT) regularization, linear L2 type regularization, is one famous method opted for the tomographic reconstruction. The penalty function, equation *2.9*, includes a Laplacian operator which relaxes the sparseness of the contribution matrix and gives out very smooth results [10][24].

$$PF(E) = \iint |\nabla^2 E(x,y)|^2 dxdy \tag{2.9}$$

$$J(E) = \gamma \|CE\|^2 + \|S - AE\|^2 \tag{2.10}$$

The constrained minimization equation for the PT regularization is given by equation *2.10*, where C is a Laplacian matrix. This matrix is *N* x *N* square matrix and $N = N_x * N_y$. $N_x$ and $N_y$ are the numbers of pixels in the reconstructed image in X and Y direction. Generally the C matrix looks like equation 2.11[27]. There are two ways to perform the PT regularization, first is the constraint minimization of equation *2.10* which is a very standard way.

$$C = \begin{pmatrix} \overbrace{\overbrace{-4 & 1 & 0 & \dots & \dots & 0 & 1 & 0 & \dots & \dots & \dots & 0}^{N_x}}^{N_x \, x \, N_y} \\ 1 & -4 & 1 & 0 & \dots & \dots & 0 & 1 & 0 & \dots & \dots & 0 \\ 0 & 1 & -4 & 1 & 0 & \dots & \dots & 0 & 1 & 0 & \dots & 0 \\ \dots & \dots & \dots & \dots & \dots & \dots & \dots & \dots & \dots & \dots & \dots & \dots \\ \dots & \dots & \dots & \dots & \dots & \dots & \dots & \dots & \dots & \dots & \dots & \dots \\ 0 & \dots & \dots & 0 & 1 & 0 & \dots & \dots & 0 & 1 & -4 & 1 \\ 0 & \dots & \dots & \dots & 0 & 1 & 0 & \dots & \dots & 0 & 1 & \underbrace{-4}_{N_x} \end{pmatrix} \qquad 2.11$$

Second is, due to the nature of the penalty function the emissivity can be analytically calculated by equation *2.12*, where *M* is the number of the line of sights. This analytical solution is a straight forward way to obtain the emissivity, *E*.

$$E(\gamma) = (A^T A + \gamma M C^T C)^{-1} A^T S \qquad (2.12)$$

The emissivity solution from equation *2.12* considers all the singular values of the eigenvalues from the A, although in a penalized form. The emissivity calculation can be restricted to specific singular values via performing SVD. The emissivity is then given by equation *2.13*.

$$\mathrm{E}(\gamma) = \frac{1}{\mathrm{M}} \sum_{j=1}^{M} \frac{\sigma_j}{\sigma_j^2 + M\gamma} v_{kj}^{`} (U^T b)_j \qquad (2.13)$$

Where $V` = C^{-1}V$, SVD $(AC^{-1}) = U\Sigma V^T$ and $\sigma$ is the singular values. The *k* stands for the pixel[24][28]. Equation *2.13*gives more freedom in restricting the use of singular values which eventually improves the reconstruction quality especially with the noisy data[28].

### 3.2.3.2 Minimum Fisher regularization

The Fisher information ($I_f$) is widely employed in statistics for the estimation of the distribution function and defined by equation *2.14*, where *L(x)* is the probability distribution and prime represents the derivative with respect to *x*.

$$I_f = \int \frac{\grave{L}(x)^2}{L(x)} \tag{2.14}$$

Fisher information $I_f$ is related to the variance of the distribution $\sigma$ by the well-known Cramer–Rao inequality[29].

$$\sigma^2 \geq \frac{1}{I_f} \tag{2.15}$$

Minimum Fisher information (MFI) is smoothening or a penalizing method. It is very clear from equation *2.14* and *2.15* the maximum information and minimum variance ($\sigma$) will be obtained where the probability distribution is low in the given space. In other words high probability regions will be less penalized (smooth) while the low probability regions will observe higher smoothening. The emissivity, *E*, is considered as the probability distribution function (*L*), under MFI regularization for plasma tomography. MFI, particularly for soft x-ray tomography problem, is very useful as it performs smoothening the low emissivity regions rather than the high emissivity regions, the core region, where in-principle smoothing is not required[30][31].

The MFI assisted least-square-error solution for the tomographic problem is given by equation *2.16* and the MFI penalty function is defined in equation *2.17*.

$$J(E) = \gamma \frac{\|CE\|^2}{E} + \|S - AE\|^2 \tag{2.16}$$

$$PF(E) = \iint \frac{|\nabla^2 E(x,y)|^2}{E}\, dxdy \tag{2.17}$$

The constrained minimization expression, equation *2.16*, is solved in an iteration method, due to the non-linear nature of the penalization function. The final solution corresponding to the emissivity is given by[32]

$$E(\gamma) = (A^T A + \gamma M C^T W C)^{-1} A^T S \tag{2.18}$$

$$W_{ij}^{(n)} = \frac{1}{E_i^{(n)}}.\delta_{ij} \qquad E_i^{(n)} > 0\,, n > 0 \tag{2.19}$$

$$W_{ij}^{(n)} = W_{max}.\delta_{ij} \qquad E_i^{(n)} \leq 0\,, n > 0 \tag{2.20}$$

Where *n* is a number of iteration *i* and *j* correspond to the pixel number. Thus the iteration starts from assumed *W* (often considered to be identity matrix) and with every iteration the *W* is updated as defined in *2.19* and *2.20*. The iteration continues until the difference between successive *W* is less than a predefined tolerance. The regularization parameter, *γ*, is estimated the same way as for the PT regularization.

### 3.2.3.3 Maximum entropy regularization

Maximum entropy (ME) regularization is widely respected tool for tomographic reconstructing from noisy and incomplete data in different fields such as radio astronomy, medical tomography, and X-ray imaging; and fluorescence spectroscopy [33]. There are different ways to define entropy however Shannon–Jaynes expression of entropy is often employed, equation *2.21*.

$$PF(E) = \sum_{i=0}^{N} E_i \ln(E_i) \tag{2.21}$$

Where *i* represent the pixel number and a total number of pixels in the reconstructed image is *N*. Maximum entropy (ME) concept address the entropy for the different regions of emissivity distribution and maximize the same to get a good fit to the data. The constrained minimization expression for ME is given by equation *2.22*[30].

$$J(E) = \gamma \sum_{i=0}^{N} E_i \ln(E_i) + \|S - AE\|^2 \tag{2.22}$$

The ME regularization ensures the non-negative solution for emissivity which is there due to the logarithmic nature of the penalty function. An efficient algorithm is required to handle the complicity offered by the non-linear nature of the problem[34][35].

## 3.3 Contribution matrix

The contribution matrix (CM) or the weight matrix is one of the pillars of the tomographic reconstruction. CM is a prerequisite for the tomographic reconstruction and precise estimation of CM ensures a good quality image. CM always have a rectangular shape where the columns represent the pixels (*N*) of the reconstructed image and rows corresponds to the Line of sights (*M*). CM reconstruction depends on the viewing geometry of the detector, different for perpendicular and tangential viewing.

The contribution matrix for the perpendicular viewing configuration is relatively easy to estimate. Referring to figure *6*, let's consider a circular plasma, black flux surfaces, and the line of sight, represented by red color, for the perpendicular viewing geometry. The plasma cross-section is divided into *5* x *5*-pixel configuration, shown with blue color. The contribution has to be calculated of every pixel for each line of sight (LOS). Consider the pixel which is marked by *1*, do not interacts with the line of sight. In other words the line of sight does not pass through the pixel at all. So the contribution of this pixel for this given line of sight is zero. Now consider the pixel which is marked as *2*.The LOS passes through this pixel, so this pixel will have a non –zero contribution. The amount of contribution can be estimated in different manners. One straight forward method is to consider the contribution as *'1'* if the LOS passes through the pixel. This kind of approach overlooks to the minute details of the emissivity distribution, however it is a good approximation for bulk plasma. The other method is to consider the length of LOS within the pixel, this kind of contribution estimation is more sensitive toward the minute details of the emissivity distribution and the viewing geometry. The line-length for pixel marked '*2*' is shown with green color. These two approaches do not consider the solid angle of plasma viewing. If their solid angle is considered then the pixel area seen by the solid cone is one of the best choices for the amount of contribution for a respective pixel. One important point which improves the quality of the CM is about the plasma boundary. Without considering the plasma boundary,

pixel beyond the plasma boundary will give a non-zero contribution. In that condition it is very difficult to have a meaningful reconstruction. This issue can be handled by considering some facts from the fusion device side. If the plasma is created in a limiter device then the limiter can be considered as the plasma boundary. With diverter configuration or more complex shaped stellarator plasma, the idea of flux surfaces is required to define a rough plasma boundary. In the case of unavailability of such information a judicious omission of pixel contribution is required. Reconstruction produced via judicious omission might not give good results to study the plasma boundary shape, however they can be useful to study the internal plasma structures.

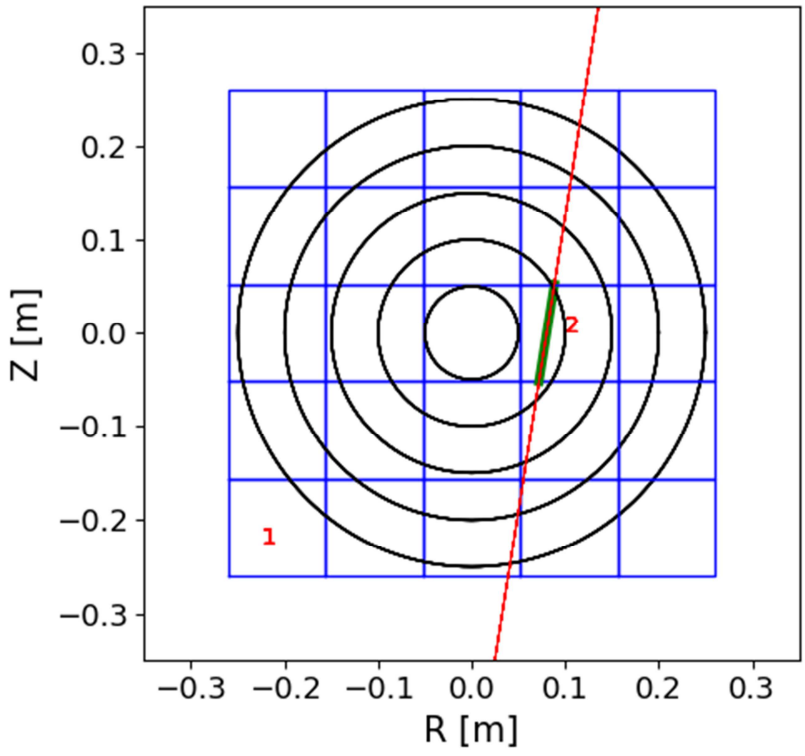


Figure 6: Calculation of the contribution for a circular cross-section plasma.

Estimation of the contribution matrix for tangential viewing geometry is an involved and complex procedure. Plasma flux surface (a typical VMEC output) or magnetic geometry information or the flux function are necessarily required for the estimation of contribution matrix[28][6][36].

Consider viewing geometry given in figure 7 (considering the Cartesian coordinate system), a circular tokamak case defined by table *2.1*.

Table 2.1: The table defining a circular tokamak

| Parameter | Unit | Value |
|---|---|---|
| Major Radio | Meters | 0.75 |
| Minor Radii | Meters | 0.25 |
| No. Line of sight | - | 30x30 = 900 |
| Location of the Image Plane | Degree | 270 |
| Number of image pixel | - | 5x5 = 25 |
| q* | - | 3.1 |
| $\beta$ | - | 0.0001 |

The image plane, where the tomographic image is being created, here $\varphi = 270^{o}$, is shown with the black grid and the viewing cone through a pinhole, shown in yellow,

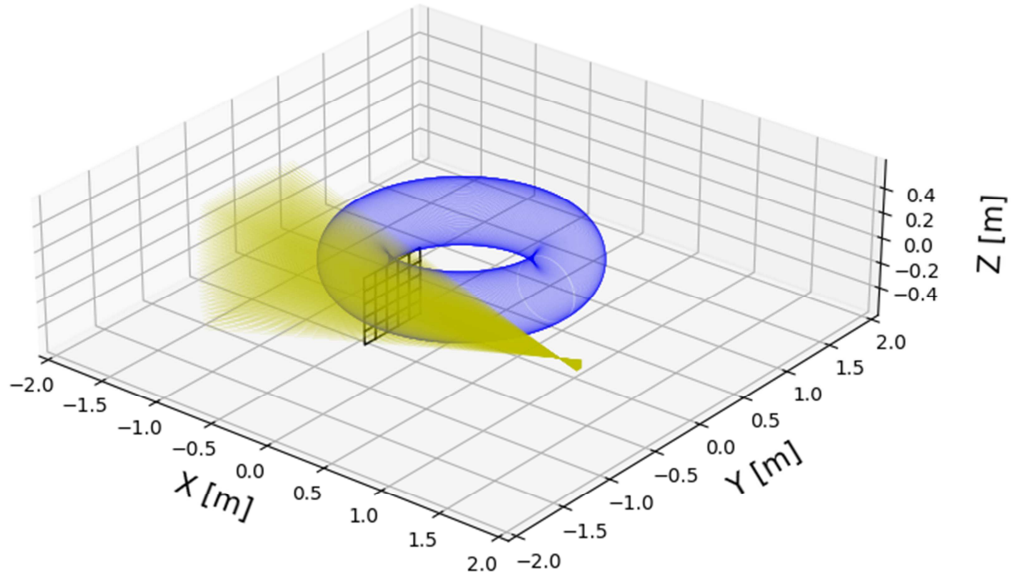


Figure 7: The viewing geometry for the tangential viewing tomography, where the Images plane is shown by black grid at toroidal location $270^{o}$.

views the plasma tangentially. The contribution matrix contains the information of the contribution of the particular image pixel for a given line of sight. The contribution for image pixel in tangential viewing tomography is the number of the total LOS point projections within an image pixel.

A magnetic field line is traced from every point on the line of sight which is terminating of the image plane. The termination point is the projection of the LOS point on the image plane. Consider the figure 8where the line of sight, in yellow, is passing through the plasma. The projection of points (black dots) on the line of sight (yellow) is shown by red dots on the image plane (black grid), at $\varphi = 270^{o}$ degree. The magnetic field line traced for every point on the line is shown by different colors (line joining black and red dots). The total number of black dots in a given pixel will be the contribution for that particular pixel.

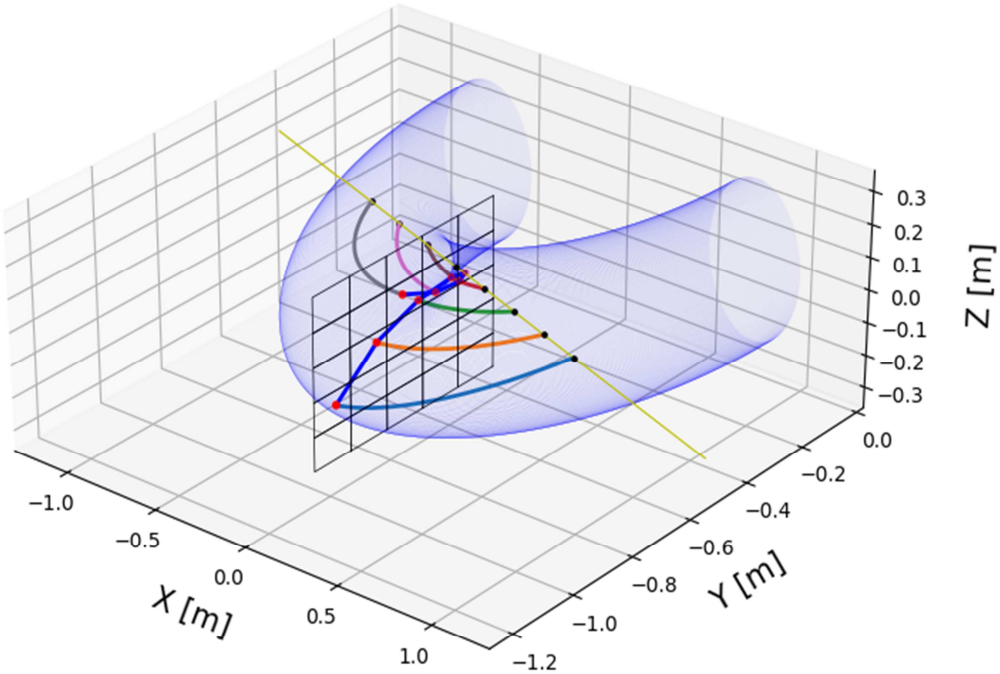


Figure 8: Projection generated by magnetic field line tracing.

## References

[1] Anon Allan M. Cormack - Facts

[2] Anon Godfrey N. Hounsfield - Facts - NobelPrize.org

[3] Anon Xrays and CT Scans of Lung Cancer

[4] Lewandowski C M, Co-investigator N, Lewandowski C M, Fallis A . and Bash E 2015 ocean acoustic tomography *course* **1** 1689–99

[5] Lluveras Núñez D, Molero-Armenta M Á, Izquierdo M Á G, Hernández M G and Anaya Velayos J J 2017 Ultrasound Transmission Tomography for Detecting and Measuring Cylindrical Objects Embedded in Concrete. *Sensors (Basel).* **17** 1085

[6] Ming T, Ohdachi S and Suzuki Y 2013 Estimate of the deposition profile of carbon pellets using a high-speed VUV imaging system in the LHD *Plasma Sci. Technol.* **15** 1178–83

[7] Granetz R S and Smeulders P 1988 X-ray tomography on JET *Nucl. Fusion* **28** 457–76

[8] Ohdachi S, Toi K and Fuchs G Tangential SX imaging for visualization of fluctuations in toroidal plasmas

[9] Ingesson L C, Alper B, Peterson B J and Vallet J C 2008 Chapter 7: Tomography diagnostics: Bolometry and soft-X-ray detection *Fusion Sci. Technol.* **53** 528–76

[10] Iwama N and Takamura S 1995 プラズマ・核融合研究におけるCT計測 *Med. Imaging Technol. ,(In Japanese)* **13** 132

[11] Iwama N and Ohdachi S 2006 Numerical Methods of Tomography for Plasma Diagnostics *J. plasma fusion Res.* **82** 399–409

[12] Hansen P C 1992 Numerical tools for analysis and solution of Fredholm

integral equations of the first kind *Inverse Probl.* **8** 849–72

[13] Ingesson L 2000 The mathematics of some tomography algorithms used at JET

[14] Cormack A M 1963 Representation of a Function by Its Line Integrals, with Some Radiological Applications *J. Appl. Phys.* **34** 2722–7

[15] Wang L and Granetz R S 1991 A simplified expression for the Radon transform of Bessel basis functions in tomography *Rev. Sci. Instrum.* **62** 842–3

[16] Nagayama Y, Büchse R, Cavallo A, Fredrickson E D, Janos A, McGuire K M, Petravic G K, Sule C and Taylor G 1990 Image reconstructions of ECE and x□ ray signals for high β plasmas on TFTR *Rev. Sci. Instrum.* **61** 3265–7

[17] Granetz R S and Camacho J . 1985 Soft-X-ray tomography on Alcator C *Nucl. Fusion* **25** 727–32

[18] Fehmers G C, Kamp L P J and Sluijter F W 1998 An algorithm for quadratic optimization with one quadratic constraint and bounds on the variables *Inverse Probl.* **14** 893–901

[19] Nagayama Y 1987 Tomography of *m* =1 mode structure in tokamak plasma using least□square□fitting method and Fourier–Bessel expansions *J. Appl. Phys.* **62** 2702–6

[20] Ohdachi S, Yamamoto S, Suzuki Y and Purohit S 2019 Tomographic inversion technique using orthogonal basis patterns *Plasma Fusion Res.* **14** 3402087

[21] Golub G H and Van Loan C F 2013 *Matrix computations.* (Johns Hopkins Univ Press)

[22] Deans S R 2007 *The radon transform and some of its applications* (Dover Publications)

[23] Hansen P C 1992 Analysis of Discrete Ill-Posed Problems by Means of the L-

Curve *SIAM Rev.* **34** 561–80

[24] Iwama N, Yoshida H, Takimoto H, Shen Y, Takamura S and Tsukishima T 1989 Phillips–Tikhonov regularization of plasma image reconstruction with the generalized cross validation *Appl. Phys. Lett.* **54** 502–4

[25] Golub G H, Heath M and Wahba G 1979 Generalized Cross-Validation as a Method for Choosing a Good Ridge Parameter *Technometrics* **21** 215–23

[26] Terasaki N, Hosoda Y, Teranishi M and Iwama N 1997 Linear algebraic algorithms for high speed and stable reconstruction of plasma image *Fusion Eng. Des.* **34**–**35** 801–4

[27] Anon ch11 2. System of Linear Equations for Discrete Laplace Equation with FDM. Wen Shen - YouTube

[28] Ohdachi S, Toi K, Fuchs G, Team TEXTOR and Group LHD Experimental 2006 Magnetic Islands Observed by a Fast-Framing Tangentially Viewing Soft X-Ray Camera on LHD and TEXTOR *Plasma Sci. Technol.* **8** 45–9

[29] Frieden B R 1988 Applications to Optics and Wave Mechanics of the Criterion of Maximum Cramer-Rao Bound *J. Mod. Opt.* **35** 1297–316

[30] Anton M, Weisen H, Dutch M J, Linden W von der, Buhlmann F, Chavan R, Marletaz B, Marmillod P and Paris P 1996 X-ray tomography on the TCV tokamak *Plasma Phys. Control. Fusion* **38** 1849–78

[31] Chattopadhyay A K, Anand A and Rao C V S 2005 Tomography for SST-1 tokamak with pixel method *Rev. Sci. Instrum.* **76** 063502

[32] Gao J M, Liu Y, Li W, Lu J, Dong Y B, Xia Z W, Yi P and Yang Q W 2013 Minimum Fisher regularization of image reconstruction for infrared imaging bolometer on HL-2A *Rev. Sci. Instrum.* **84** 093503

[33] Livesey A K and Brochon J C 1987 Analyzing the distribution of decay constants in pulse-fluorimetry using the maximum entropy method. *Biophys. J.*

**52** 693–706

[34] Skilling J and Bryan R K 1984 Maximum entropy image reconstruction: general algorithm *Mon. Not. R. Astron. Soc.* **211** 111–24

[35] Denisova N V 1998 Maximum-entropy-based tomography for gas and plasma diagnostics *J. Phys. D. Appl. Phys.* **31** 1888–95

[36] Wingen A, Shafer M W, Unterberg E A, Hill J C and Hillis D L 2015 Regularization of soft-X-ray imaging in the DIII-D tokamak *J. Comput. Phys.* **289** 83–95

# Chapter III

# Laplacian Eigen Functions


## Abstract

A new tomographic reconstruction process via series expansion method considering orthogonal Laplacian Eigen Function (LEF) patterns is introduced here in this chapter. The peculiar features of the LEF are elaborated as a justification for employing the LEF for the plasma tomographic reconstruction. The chapter also gives a detailed recipe of the reconstruction process.

## 1. Introduction

Traditionally the reconstruction from the global orthogonal pattern, such as Fourier–Bessel functions, are employed extensively in the past[1] . The success of these global orthogonal patters lies in the fact that with the limited information the emission profile is recovered successfully, especially for circular cross-section plasma[2]. These patterns also satisfy the boundary conditions like the Dirichlet's boundary condition, patterns are zero at the boundary. The case where patterns are aligned to the magnetic surface, in other words calculated on the magnetic surface, the island structure can be expressed convincingly for circular cross-section. However near orthogonality of these patterns, like Fourier–Bessel functions, observed for a non – circular plasma cross-section when aligned with flux surface. The requirement of a robust tomographic reconstruction method is required which is capable to handle the complexities of the viewing geometries, complex plasma shape without detailed equilibrium information, not so expensive computing and satisfies the different mathematical requirements to have a stable result.

### 1.1 Laplacian Eigen Function (LEF)

The objective is to find the genuine orthonormal basis functions which are domain-shape independent and easy to calculate. The eigenfunction of the Laplacian is one of the good choices.

Consider the $\mathcal{L}$ as the Laplacian operator, defined by equation 3.1, and represented by either $-\Delta$ or $\nabla^2$ . Laplacian operator is a differential operator defined as the divergence of the gradient of a function on Euclidean space. Physically Laplacian represents the quantitative measure of the "spreading out" of the change of the field in space. Large values of Laplacian shows a considerable change in the field. Likewise for the smaller values, not much change. Crudely is can be said Laplacian represent the 'change in change ' for any parameter.

$$\mathcal{L} = -\Delta = -\frac{\partial^2}{\partial {x_1}^2} - \frac{\partial^2}{\partial {x_2}^2} - \frac{\partial^2}{\partial {x_3}^2} - \frac{\partial^2}{\partial {x_4}^2} \tag{3.1}$$

The direct estimation of the Eigenfunction of the $\boldsymbol{\mathcal{L}}$ is difficult due to its unboundedness, however a simpler way is, employing the Green's function. A Green's function is just $\boldsymbol{\mathcal{L}}^{-1}$ of the Laplacian. The Green's functions are the compact and self-adjoint operator and offer a prominent control of $\boldsymbol{\mathcal{L}}$ spectral properties Along with that $\boldsymbol{\mathcal{L}}$ have a complete orthonormal basis for the domain thus eigenfunction expansion of the domain, is possible conveniently. Although having such qualities the direct computation, solving the Helmholtz equation on a general domain, of the eigenfunctions is not so easy, at least in this form. Finding the non-trivial solution $u = \varphi$ for equation 3.2, which satisfy $\xi\lambda = 0$, $\xi$ specifies the boundary condition.

$$-\Delta u = \lambda u \tag{3.2}$$

The Green's function computation for a general domain satisfying the usual boundary condition such as the Dirichlet or the Neumann condition is also very difficult. To avoid such complex situation is an integral operator $\boldsymbol{K}$ which commutes with $\boldsymbol{\mathcal{L}}$ ,without imposing the strict boundary condition. Then the eigenfunctions of the $\boldsymbol{\mathcal{L}}$ are the same as those of the $\boldsymbol{K}$[3]. Considering such mathematical notions kernel /Green's function to estimate the Eigenfunction of Laplacian is given by equation 3.3[2,4–6].

$$K(r,r') \triangleq \begin{Bmatrix} -\frac{1}{2}|r-r'| & if\ d=1 \\ -\frac{1}{2\pi} ln|r-r'| & if\ d=2 \\ \frac{|r-r'|^{2-d}}{(d-2)w_d} & if\ d>2 \end{Bmatrix} \tag{3.3}$$

$$w_d \triangleq \frac{2\pi^{d/2}}{\Gamma(d/2)} \tag{3.4}$$

Equation 3.3 and 3.4 gives the computation of the kernel over a general domain involving two points *r* and *r'*. The kernel defined here is only a function of the distance between the two points *r* and *r'*, thus by nature the kernel is independent of the shape of the domain. A very important character of this kernel which is exploited for the tomographic construction procedure, making the procedure to handle irregular plasma shapes and even for the restricted view of the plasma.

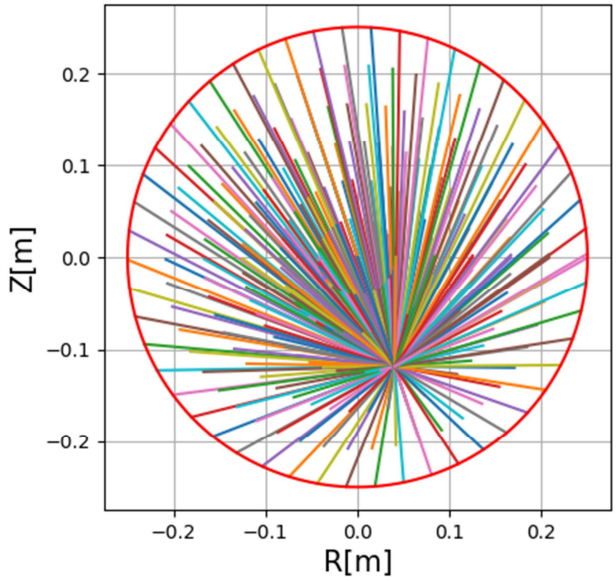


Figure 1. The kernel calculation for a circle domain having a grid of 7x51. Straight lines represents the distance between r any point on the grid (7x51) and r' = [0.0402,-0.118].

Figure 1 shows the kernel calculation over a circle for *r'* point, where the domain is made up of 7x51 grid. The same process is repeated to estimate the kernel matrix, the pictural representation of the kernel matrix is shown in figure 2. The kernel matrix is employed for the estimation of the Laplacian eigenfunction. The first 20 Eigenfunction patterns are shown in figure 3 for the above mentioned circular grid.

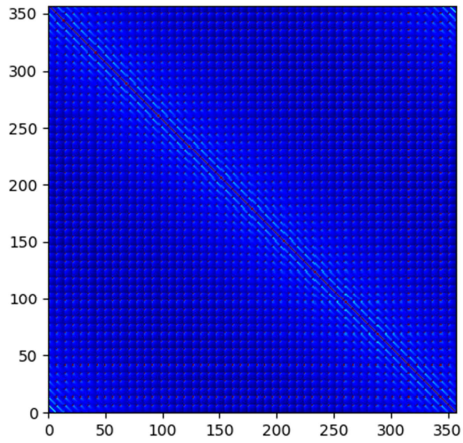


Figure 2. Pectoral representation of the kernel matrix for 7x51 grid, matrix

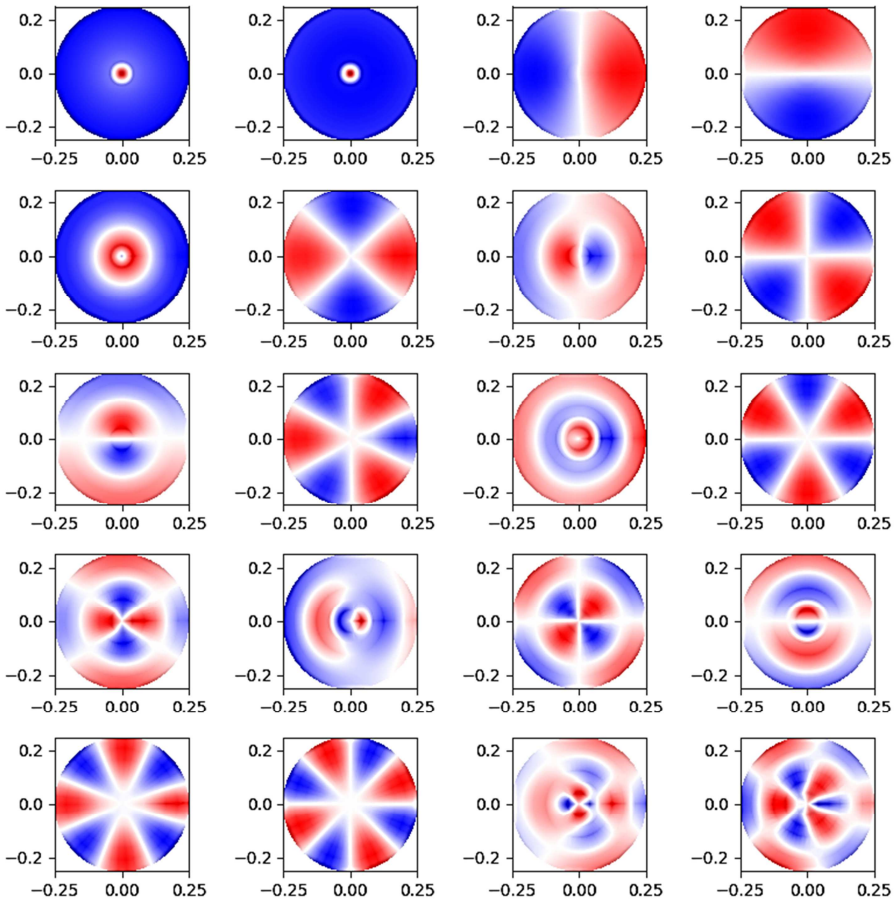


Figure 3. The first 20 laplacian Eigen function pattern for a circular

These eigenfunctions are employed to decompose the image into its different components to study different aspect addressing a range of interest. An interesting example is shown in figure 4 about the retinal ganglion cell (RGC), which is a type of neuron located near the inner surface (the ganglion cell layer) of the retina of the eye **[7]**.

Figure 4(a) represents the location of these cells in the eye and the 4(b) is the 2-D image of the cell taken from the normal direction to the cell plane. This image needs to be decomposed into different spatial frequencies/different spatial components in order to understand the 3-D structure of the cell. The Laplacian Eigenfunction method

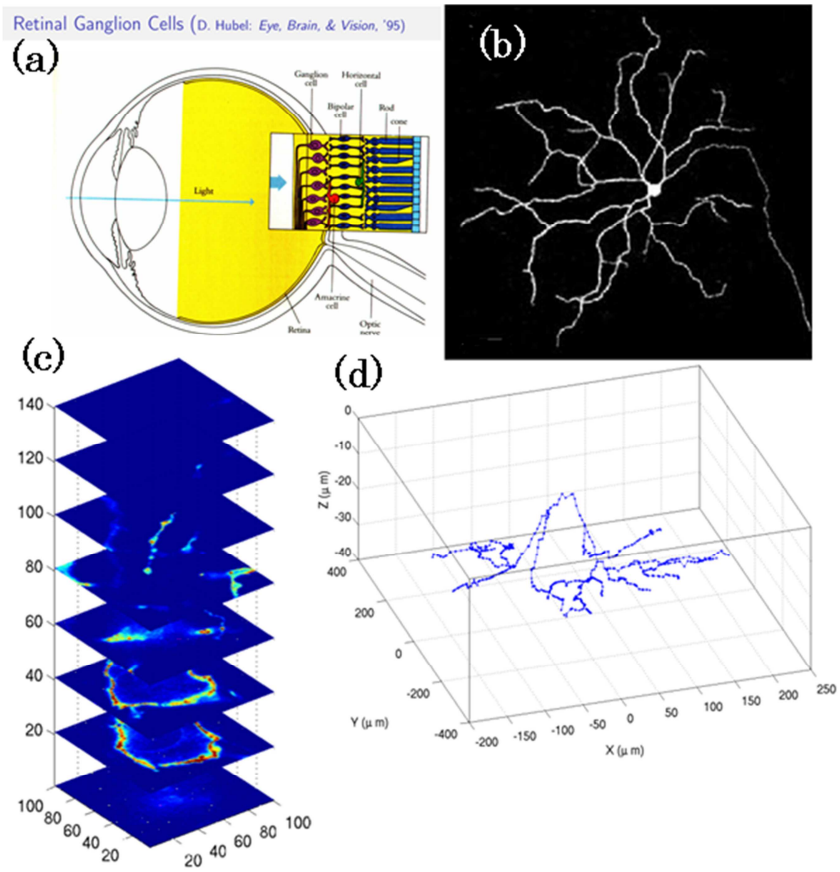


Figure 4. The RGC is located in the eye, 4(a), with a 2-D appearance as, 4(b). LEF can recover the 3-D structure of the RGC 4(c and d) efficiently.

is applied to the 2-D image, figure 4(b) to recover the 3-D structure of the RGC and the result is shown in figure 4( c and d). Figure 4(c) shows the recovery of information at different height whereas figure 4(d) gives the complete realization of the 3-D RGC structure.The methodology is very effective in recovering the 3-D structure of RGC. Strong capabilities such as domain-independent , convenient calculation presents LEF as a natural contender to be employed for the tangential plasma viewing tomographic reconstructions for fusion-grade plasma especially for the constrained/ restricted viewing situations.

## 2. Why LEF for plasma Tomography

The important question arises that why LEF orthogonal basis functions should be employed to the tomographic reconstruction of the plasma emissions recorded by the imaging diagnostics. The advantage of the LEF over the existing basis functions are described systematically to make a strong recommendation of LEF for the reconstructions.

- The Fourier–Bessel (FB) functions are one of the natural choices of the orthogonal basis function for the tomographic reconstruction. These functions perform well for the circular cross-section due to the circular nature of the functions even if aligned on the flux surfaces. While applying to the non – circular case like elongated plasma or the 3D plasma the FB flux surface aligned patterns are not exactly orthogonal but near-orthogonal. In contrast to FB, flux surface aligned LEF patterns retain the orthogonality even for the non-circular plasma cross-sections, which is one of the important characters of LEF.

- As discussed the LEF patterns are calculated via Green's function which is sole function of the distance between two points defined over the domain/ plasma cross-section. This feature establishes the fact that the LEF patterns are independent of the shape of the domain. In other words the patterns do not

depend on the shape of the plasma cross-section. This is one of the advantages of LEF over other methods.

- The Green's function, defined in equation 3.3, clearly shows that the estimation of the LEF patterns is easy to calculate, just estimation of the distance. This relaxes the computation expenses for the tomographic reconstructions.

- The unboundedness of the LEF is one of the prime concerns however it can be addressed by having a computation boundary predefined to the reconstruction. It can be said crudely that if the information of rough computation is available then a realistic reconstruction method can be a device. Evaluating this situation with the FB where the flux surfaces information is always required, LEF seems to be a better choice.

- The LEF patterns are global orthogonal patterns, so when the reconstruction for the restricted viewing geometry with non-circular plasma is performed it is expected that with the restricted view, the LEF reconstruction process can recover the global emission pattern. This kind of capability is required for the next-generation fusion devices where the plasma viewing will be highly contested and full plasma cross-section viewing may not be possible at all.

The above-mentioned discussion strongly suggests that the LEF orthogonal patterns are a good option for the tomographic reconstruction, especially for the tangential viewing imaging diagnostic where the view is plagued with constraints.

## 3. Tomographic reconstruction LEF based

The LEF based tomographic reconstruction procedure is explained in this section, defines the basic steps for the recovery of the tomographic image for any toroidal location within the field of view of the respective tangential viewing imaging diagnostic.

The tomographic reconstruction problem can be written in terms of the line integrated data (B) and the local emission (E), see equation 3.5, where A represents the geometric weight for the location $j^{th}$ along the $i^{th}$ line of sight.

$$\boldsymbol{b_i = \int_{j=1}^{n} A_{ij} E_j} \qquad (\mathbf{3.5})$$

E at any point, defined by ($x$, $y$) can be defined by equation 3.6 and subsequently simplified as equation 3.7, matrix format. Where $X = AC_p$.

$$\boldsymbol{E(x,y) = \sum_{p} \beta_p C_p(x,y)} \qquad (\mathbf{3.6})$$

$$\boldsymbol{B = \beta . X} \qquad (\mathbf{3.7})$$

The objective is the estimation of emission profile E via equation 3.6. Such estimation can be made when the expansion coefficients ($\beta_p$) and the expansion pattern ($\boldsymbol{C}_p$) are known.

Consider the following viewing geometry, figure 5, for a circular tokamak plasma. The imaging diagnostic is having 900 channels, in 30x30 configuration, viewing the

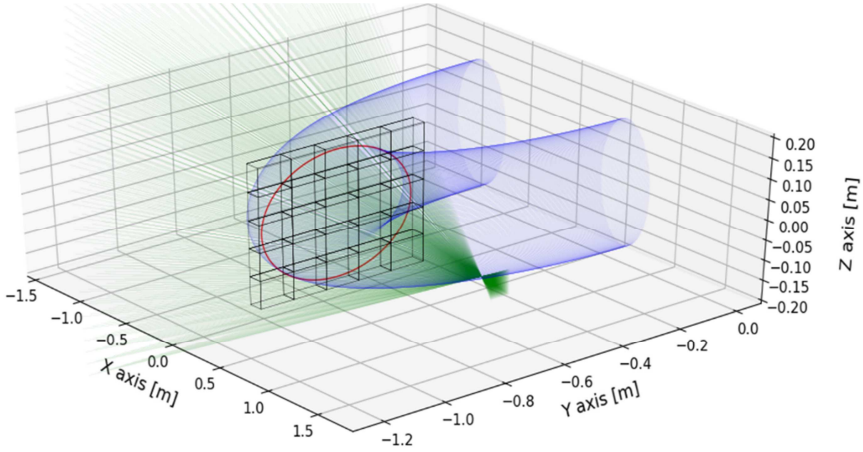


Figure 5. Tangential viewing geometry for the imaging diagnostic for a circular tokamak.

full plasma. The image plane, where the tomographic reconstruction will be performed to recover the 2-D emission profile, is considered at toroidal location $\varphi$= 270$^{o}$.The plasma boundary at this location is shown with the red color. The geometrical weight matrix is made over 3-D pixel commonly referred to as a voxel, shown with black color and with 5x5 configuration. The shape of the voxel is cube here for this problem, however it may vary with different problems. The geometrical weight of a line of sight (LOS) for a given voxel is the length of the LOS within the voxel. For this condition the LEF based tomographic reconstruction is explained step by step.

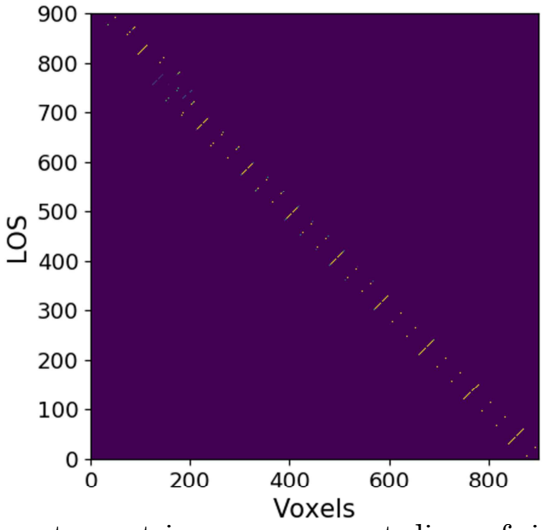


Figure 6. Geometry matrix rows represents lines of sights and columns represents the voxels.

- The first step is the calculation of the geometry matrix, *A*, rows represent the LOS and columns represents the voxel. In order to have a proper tomographic image the number image voxel should be good enough. For the practical purpose we consider the 30x30 voxel grid, total 900. As described after fixing the shape of the voxel, cube in this case, the length of the LOS is estimated for every voxel the determination of *A* is performed. Figure 6 is the image representation of the

geometry matrix. It can be seen that the matrix is sparse, inherent character of the tomographic reconstruction problem, ill-posed problem.

- The next step is the estimation of the Laplacian Eigenfunction pattern for the domain. The LEF patterns are calculated on flux surfaces (r and r' are on flux surface) for tokamak plasma. The near orthogonality of the patterns is satisfied with this mapping. Later the patterns are extrapolated over the voxel mid-point grid.

$$\boldsymbol{K(r,r') = -\frac{1}{2\pi} ln|r - r'|} \qquad (\mathbf{3.8})$$

The estimation of the Eigenfunction for this kernel matrix is done and different Eigenfunction patterns are then achieved and shown in figure 7, over the voxel grid

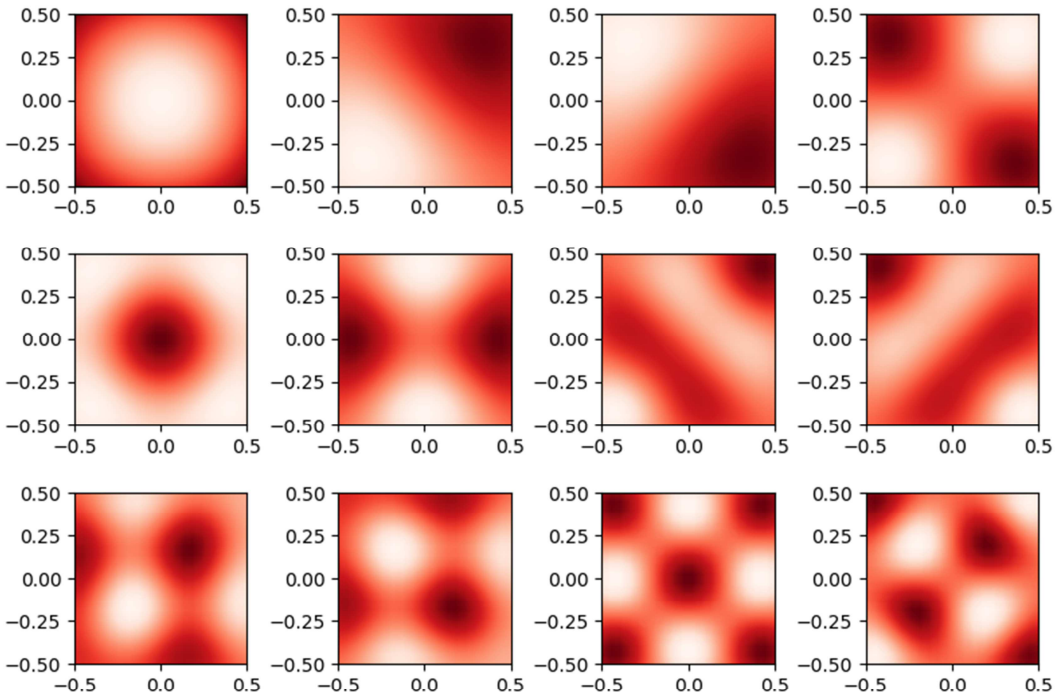


Figure 7. The first 12 laplacian Eigen function patters.

- Next step is the estimation of the expansion coefficients, $\beta$, see equation 3.6 and 3.7. The process starts from the equation 3.7, the expansion coefficients are estimated via simple least-square approximation with regularizations. The mathematical definition of this procedure is expressed by the following equation.

$$\boldsymbol{agri\ min}\left\{\sum_{\boldsymbol{p}}\left(\boldsymbol{b_p} - \boldsymbol{\beta_p X_p}\right)^{\boldsymbol{2}} + \boldsymbol{\gamma R_g}\right\} \qquad (\mathbf{3.9})$$

The term $R_g$ is the regularization function which introduces the smoothness in the

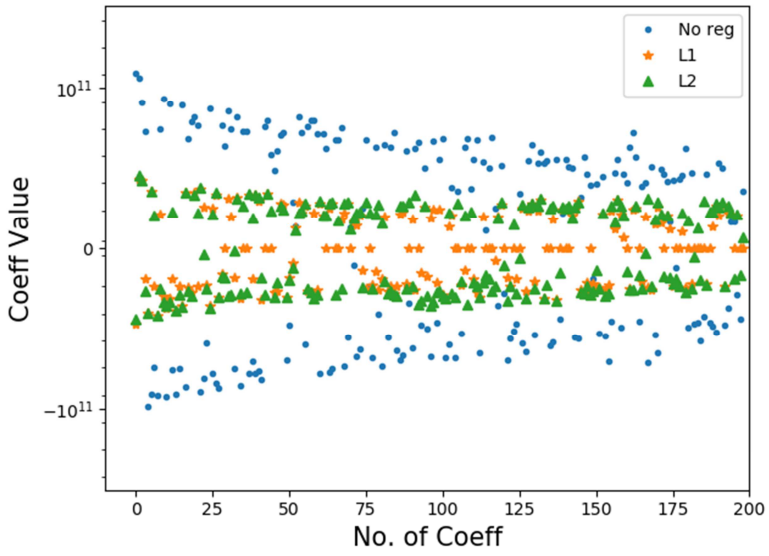


Figure 8. Comparison of L1 and L2 regularization with the least square approximation

least square approximation. The $R_g$ can be either L1 ($|\beta|$) or L2 ($|\beta|^2$), both regularizations provide the smoothness in the least square approximation, however holds different character while smoothening. Referring to the figure 8. The results from the two regularizations are shown. The L1 shrinks less important coefficient to zero, removing some feature altogether. The property works well for feature selection. L2 regularization does not remove features from the data set, less significant information is still available in the fitting. However overall

smoothness is achieved. Due to the special property of shrinking of less important coefficients by L1 regularization, it is employed here for the estimation of expansion coefficients in this new proposed tomographic reconstruction procedure.

- The estimation of the expansion coefficient is followed by the reconstruction of the tomographic image. A selected number of Eigenfunction / or all are employed in equation 3.6 along with the expansion coefficient and subsequently the 2-D emission profile at $\varphi = 270^{o}$ is achieved, see figure 10.

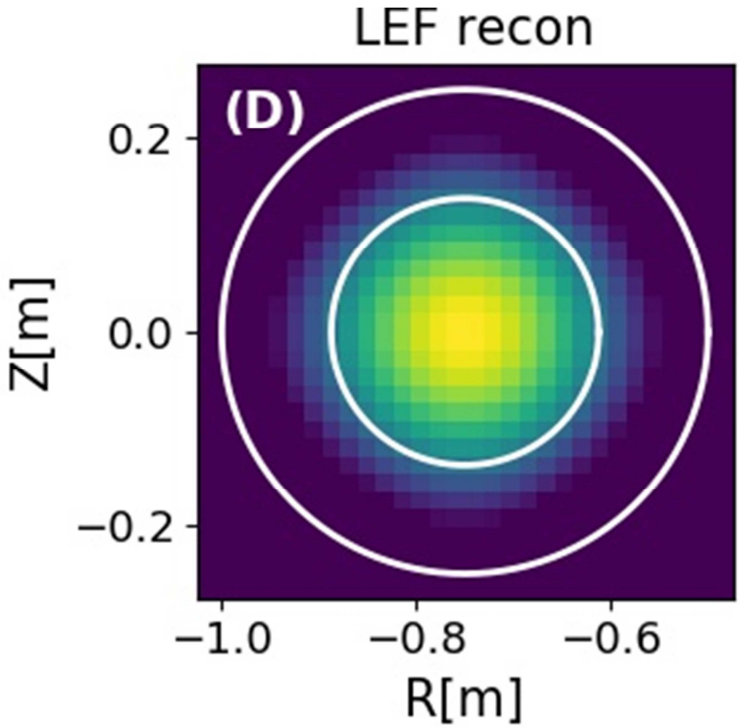


Figure 10. The recovered 2-D emission profile.

## References

[1] Nagayama Y 1987 Tomography of *m* =1 mode structure in tokamak plasma using least square fitting method and Fourier–Bessel expansions *J. Appl. Phys.* **62** 2702–6

[2] Ohdachi S, Yamamoto S, Suzuki Y and Purohit S 2019 Tomographic inversion technique using orthogonal basis patterns *Plasma Fusion Res.* **14** 3402087

[3] Friedman B 1990 *Principles and techniques of applied mathematics* (John Wiley & Sons, Inc., New York, 1956, republished by Dover Publications, Inc. in 1990)

[4] SAITO Naoki 2016 Laplacian Eigenfunctions and Their Application to Image Data Analysis *J. Plasma Fusion Res. (in Japanese)* **92** 904–11

[5] Saito N 2008 Data analysis and representation on a general domain using eigenfunctions of Laplacian *Appl. Comput. Harmon. Anal.* **25** 68–97

[6] Saito N 2005 Geometric harmonics as a statistical image processing tool for images on irregularly-shaped domains *IEEE/SP 13th Workshop on Statistical Signal Processing, 2005* (IEEE) pp 425–30

[7] Saito N *MAT 280: Harmonic Analysis on Graphs & Networks Lecture 6: Graph Laplacian Eigenvalues II*

# Chapter IV

# LEF for Tokamak


## Abstract

The benchmarking for the LEF based reconstruction of tokamak plasma with tangential viewing geometry is discussed in this chapter. Reconstruction for different emission profiles and viewing conditions is also discussed. The main objective of this exercise is to compare the effectiveness of LEF over the standard tomographic reconstruction method.

## 1. Introduction

The tangential viewing geometry, viewing the plasma tangential to the magnetic field, brings a different set of challenges like the complex viewing of the plasma and sometimes partial view, restricted viewing case. Such complications are often faced by the tomographic reconstruction and a reliable tomographic reconstruction procedure is required for the recovery of the emission profile. Here in this chapter the implementation /benchmarking of LEF based reconstruction for the tangential viewing geometry is discussed for the tokamak plasma. The main objective of the exercise is the step by step performance check of LEF and compare with the standard reconstruction methods.

## 2. Viewing geometry

The viewing geometry for the tangential viewing tomographic system is shown in figure 1, for different planes. The plasma and the tomographic diagnostic are defined as per table 1.

**Table1: Plasma, device, and the diagnostic parameters**

| **Parameter** | **Symbol (Unit)** | **Values** |
|---|---|---|
| Major radius | R($m$) | 0.75 |
| Minor radius | a($m$) | 0.25 |
| Limiter radius | $a_{lim}$($m$) | 0.28 |
| Vacuum vessel radius | $a_{ves}$($m$) | 0.3 |
| Toroidal field at center | $B_T = B_0$ (T) | 1 |
| Kink safety factor | q* | 3.1 |
| Tangential viewing tomography (TVT) system | | |
| Lines of sight | | 900 |
| Location | | Focused at $\phi = 270^o$ |

The tokamak plasma , in green , is having a toroidal symmetry, see figure 1. The lines of sight from the detector covers the complete plasma cross-section and $\phi = 270^{o}$ is considered as the image plane, for which the 2D emission profile will be generated. The LEF patterns employed here are shown in figure 2. As discussed due to the symmetry in the plasma, 2D LEF is employed here for the tomographic reconstruction. Referring to the second line of equation 3.3 in chapter 3.

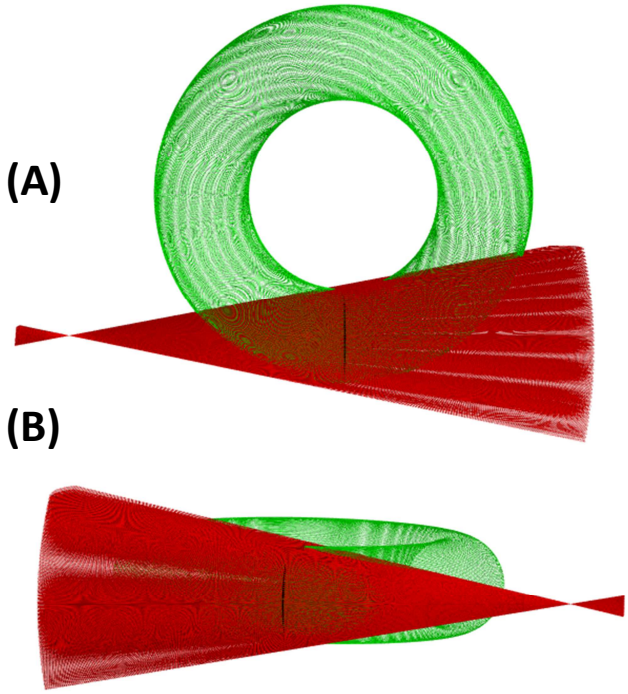


Figure 1. Top view (A) and the horizontal view (B), Z-X plane, is shown for the viewing geometry. Where the plasma is represented by green and lines of sights are shown by red.

The LEF based tomographic reconstruction process is designed independently of the plasma emission wavelength, which means that the process can be applied to the line integrated information for different wave-lenghts. The soft X-ray and VUV/ visible emission profiles are considered herefor benchmarking exercise. The reconstruction results are compared with the so-called Phillips-Tikhonov (PT) regularization reconstruction procedure where regularized least square approximation along with the singular value

decomposition is employed for the estimation of the emission profile. Refer to chapter II for details. The comparison is made by comparing the 1D emission profiles recovered from these two reconstruction methodologies. The contribution matrix is made for the voxels considered on the image plane at $\phi = 270^{o}$ location. The construction procedure is discussed in chapter III.

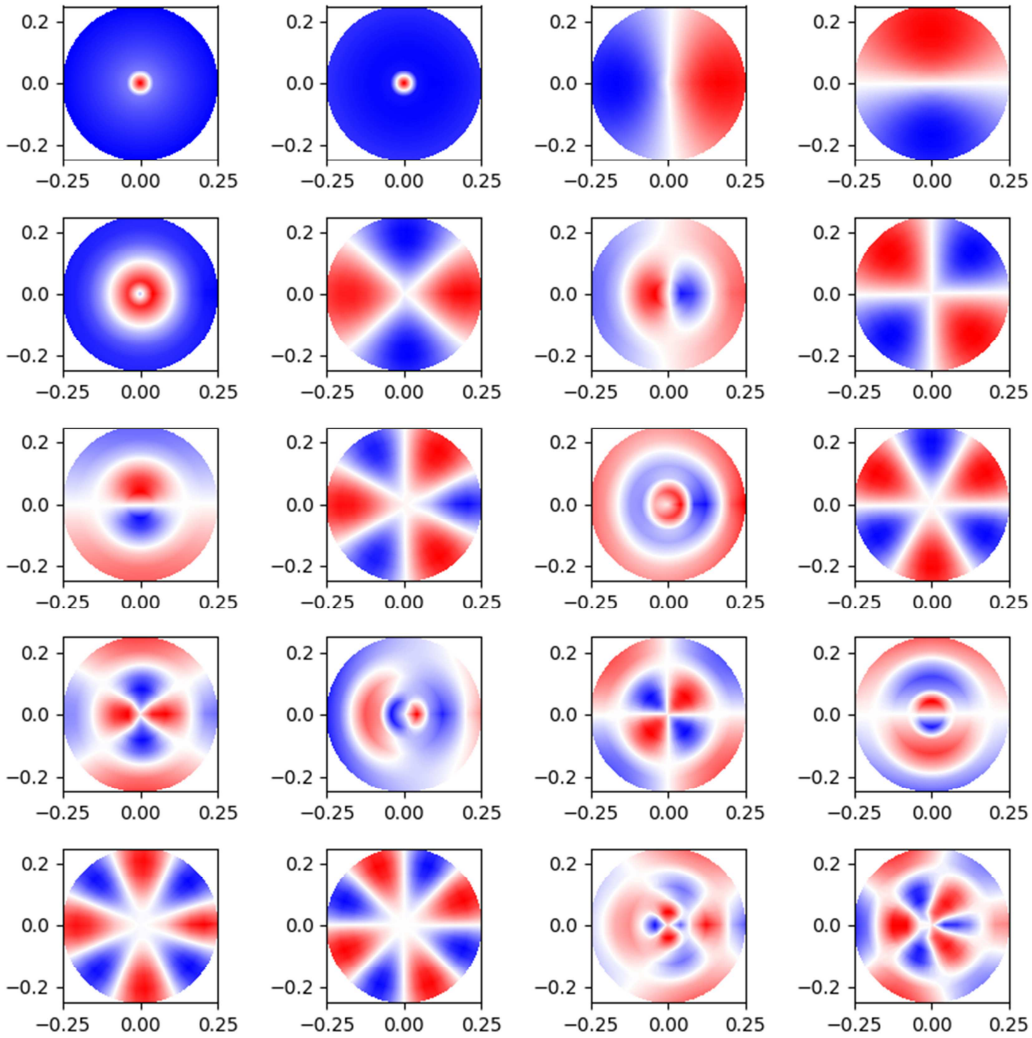


Figure 2. The LEF pattern for the tokamak plasma for first 25 Eigen values.

## 3. The reconstructions

The tomographic reconstruction can be divided into two categories the first category addresses a situation where the diagnostic is able to view the complete plasma. Second is considered as the restricted view where the diagnostic view the plasma partially.

### 3.1 Complete view

The tomographic reconstruction for soft X-ray type of emission profile is discussed here. Figure 3, shows the reconstruction for a Gaussian type of SX emission profile.

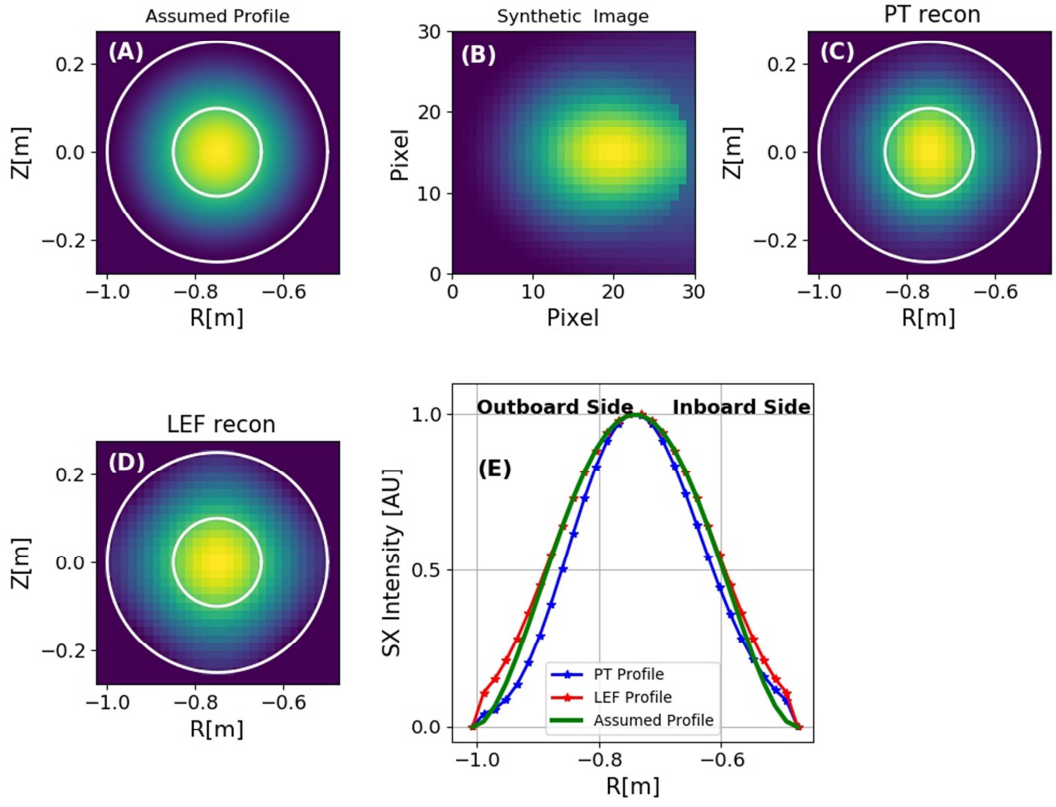


Figure 3. The assumed profile (A), Synthetic image (B), PT reconstruction (C) and the LEF reconstruction (D) are shown. The 1D profiles from the two methods are compared with the assumed profile in (E).

Figure 3(A) shows the assumed Gaussian profile and the outer white circle represents the circular poloidal limiter, 3(B) represents the synthetic image seen by the detector (30x30 pixels). The reconstructed image by the PT and LEF are shown in figure 3(C) and 3(D), respectively. The recovered 1D emission profiles are given in figure 3(E). Considering the two reconstructions 3(C) and 3(D), it can be said qualitatively that both the images represent the assumed emission profile. The qualitative evaluation of the reconstruction can be performed by comparing the 1D emission profile recovered from the reconstructed images with the assumed 1D emission profile, see figure 3(E) The two profiles match with the assumed profile efficiently. The LEF and PT determine the plasma magnetic axis precisely.

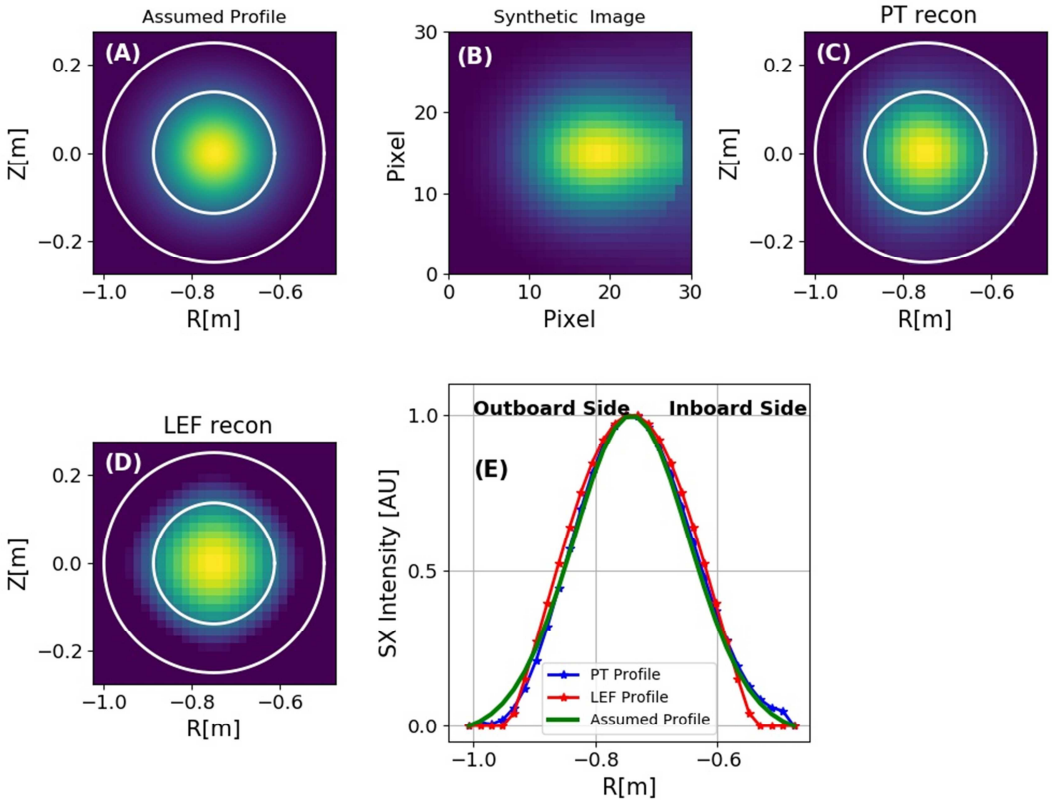


Figure 4. The assumed profile (A), Synthetic image (B), PT reconstruction (C) and the LEF reconstruction (D) are shown. The 1D profiles from the two methods are compared with the assumed profile in (E).

Figure 4(A) shows the assumed peaked profile and the outer white circle represent the circular poloidal limiter, 4(B) represents the synthetic image seen by the detector (30x30 pixels). The reconstructed image by the PT and LEF are shown in image 4(C) and 4(D), respectively. The recovered 1D emission profiles are given in figure 4(E). Considering the two reconstructions 4(C) and 4(D), it can be said qualitatively that both the images represent the assumed emission profile. The 1D profile recovered from the two methods are match with the assumed profile efficiently, see figure 4(E)

The figure 5(A) shows the assumed emission profile which represents VUV type of emission, 5(B) represents the synthetic image seen by the detector (30x30

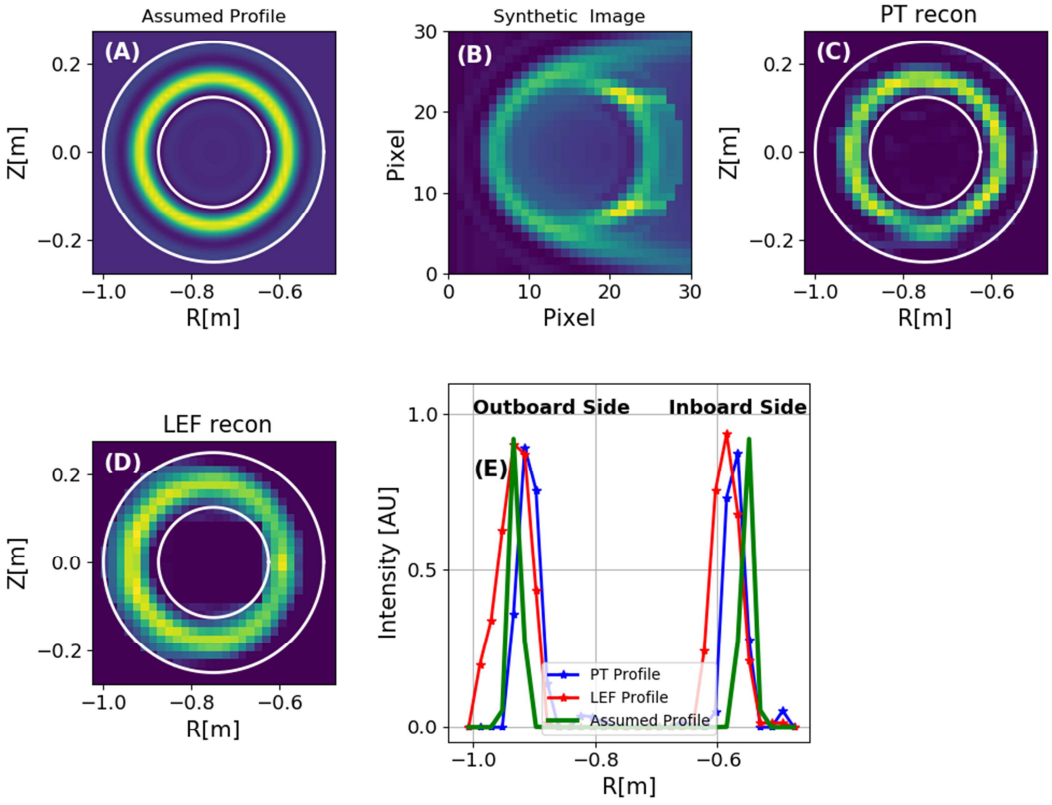


Figure 5. The assumed profile (A), Synthetic image (B), PT reconstruction (C) and the LEF reconstruction (D) are shown. The 1D profiles from the two methods are compared with the assumed profile in (E).

pixels). The reconstructed image by the PT and LEF are shown in image 5(C) and 5(D), respectively. The recovered 1D emission profiles are given in figure 5(E). Considering the two reconstructions 5(C) and 5(D), it can be said qualitatively that both the images represent the assumed emission profile. The 1D profile recovered from the two methods are matching with the assumed profile efficiently, see figure 5(E). The VUV emission location is determined in line to the assumed profile.

The quality of any image reconstruction is defined by the quality parameter ($d^2$)[1]. The mathematical definition of the $d^2$ is given by equation 4.1.

$$\boldsymbol{d^2 = \frac{1}{j}\sum_{j}\frac{(E_{asu} - E_{rec})^2}{E^2_{Masu}}} \qquad (\mathbf{4.1})$$

The $E_{asu}$ is the assumed 2D profile , $E_{rec}$ is the recovered 2D emission profile , $E_{Masu}$ is the maximum value of the assumed profile and *j* represents the number of image pixels in equation 4.1.

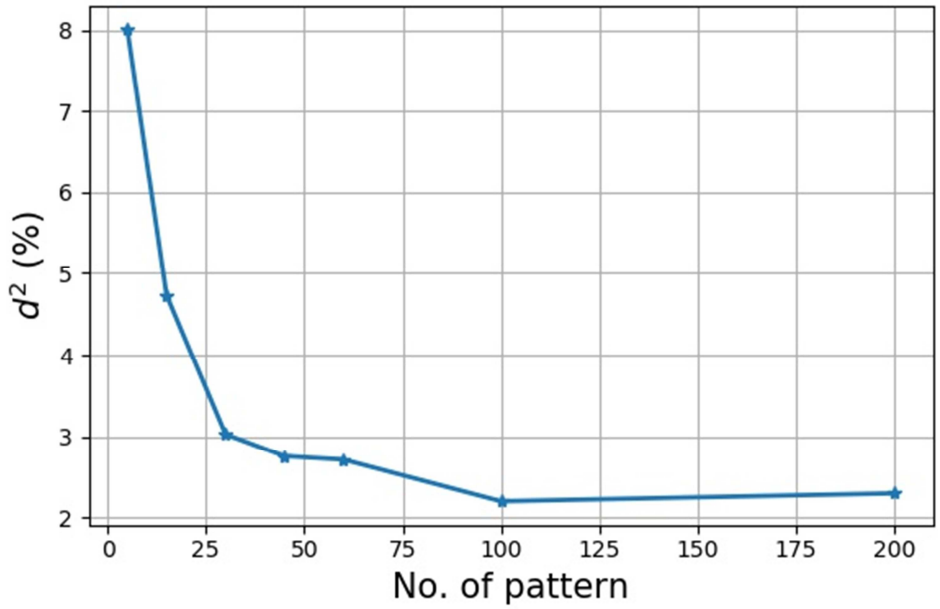


Figure 6. The $d^2$ parameter (%) is presented as a function of the number of patterns employed in reconstruction.

The $d^2$ parameter is shown as the function of the number of LEF patterns employed in image reconstruction. It is clear that the quality of the image increases with the increase in the number of patterns employed in the reconstruction of the tomographic image. However, the $d^2$ does not improve much after a certain number of patterns. Which is attributed to the fact that for a higher number of patterns are associated with smaller eigenvalues and thus have a very small contribution to the reconstructed image. The $d^2$ value for figure 3,4 and 5 are less than 3%.

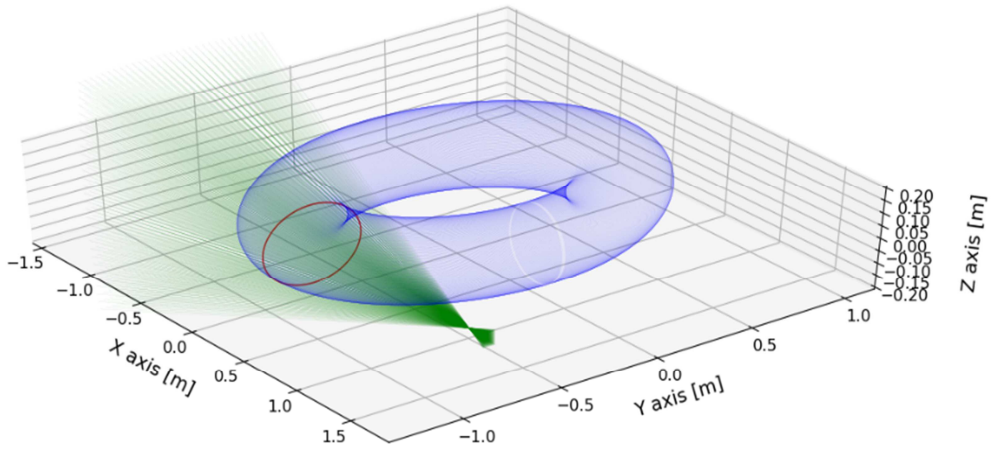


Figure 7. The viewing geometry for horizontally elongated plasma tokamak.

The LEF based tomographic reconstruction was also implemented for the non-circular case. Considering in mind that eventual implementation of LEF based reconstructions to the LHD in VUV wavelength[1].The non-circular tokamak case is taken as horizontally elongated plasma with toroidal symmetry. This situation can be considered as a simplified LHD plasma, without the toroidal asymmetry.The elongation in this case is considered to be $\kappa$ = 1.6. the plasma is shown in figure 7. The machine and plasma parameters are the same as for the circular cross-section tokamak. The image plane is at $\phi = 270^o$ location, shown with the red circle in figure 7. The reconstruction for this kind of plasma is shown in figure 8 and 9 with two assumed profiles representing the soft X-ray and VUV emission profiles.

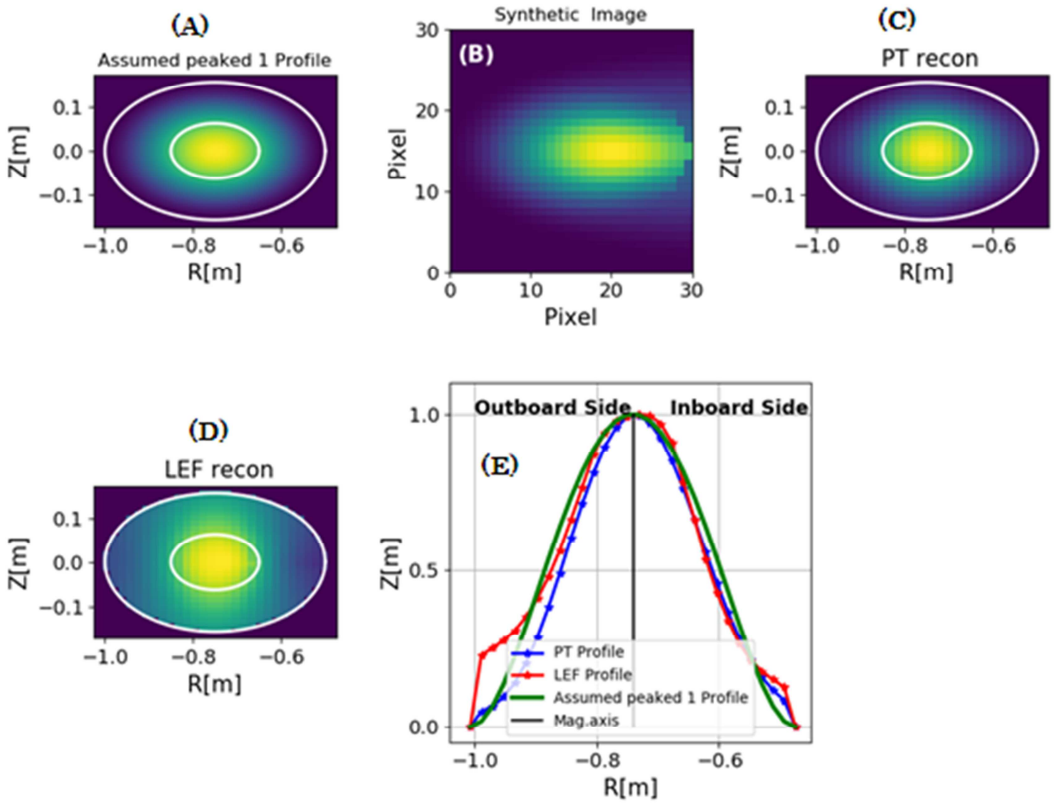


Figure 8. The assumed profile (A), Synthetic image (B), PT reconstruction (C) and the LEF reconstruction (D) are shown. The 1D profiles from the two methods are compared with the assumed profile in (E).

The assumed profile (A), synthetic image (B), reconstructed image by the PT (C) and LEF (D), 1D recovered emission profile (E), are shown, respectively in figure 8 and 9 The reconstructed images from the PT 8(C)/9(C) and LEF 8(D)/9(D) are comparable to the assumed profile for the horizontally elongated plasma. Magnetic axis location, figure 8(E) and the plasma VUV emission location, figure 9(E), are determined precisely and are coherent with the assumed profile by both LEF and PT. The $d^2$ values for these reconstructions are less than 3.5%.

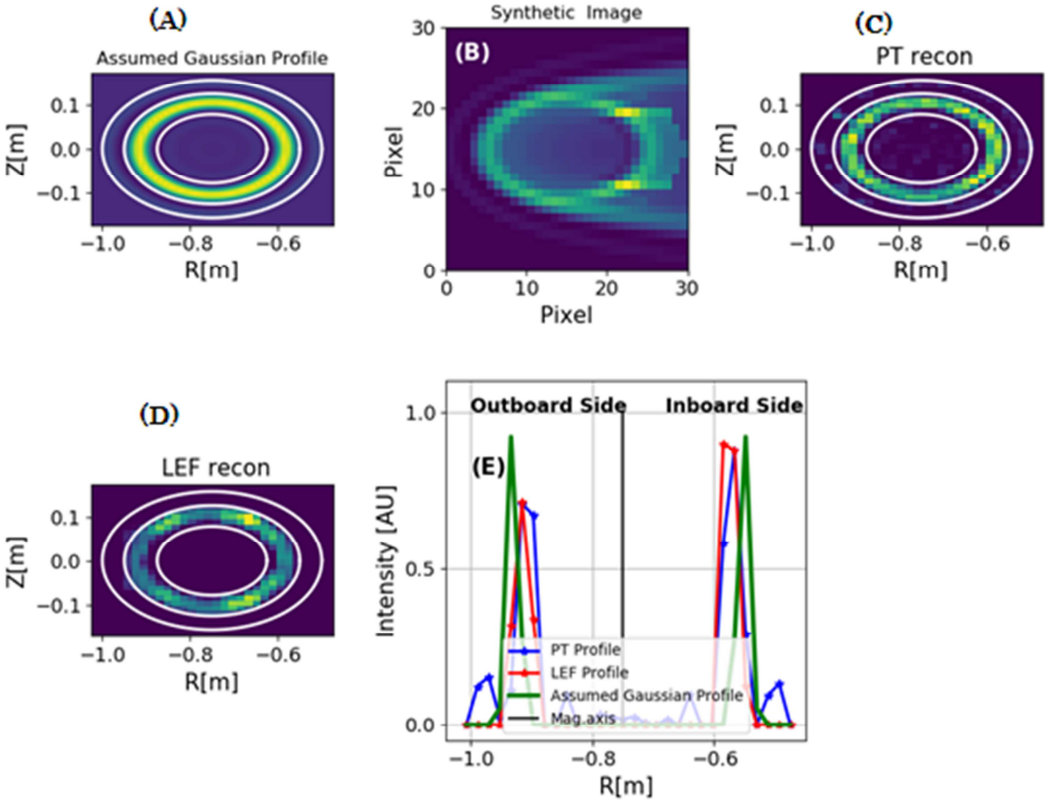


Figure 9. The assumed profile (A), Synthetic image (B), PT reconstruction (C) and the LEF reconstruction (D) are shown. The 1D profiles from the two methods are compared with the assumed profile in (E).

## 3.2 Restricted view

The recovery of 2D emission profile from the restricted viewing geometry is one of the challenges observed by the tomographic reconstructions. The restricted viewing is referred to as the situation where the diagnostic is not able to view the complete plasma cross-section. As a matter of fact the LEF patterns are estimated as global patterns thus it is expected that LEF should be able to recover the 2D emission profile even from the restricted viewing geometries. The capabilities for the recovery of the emission profile for restricted viewing geometry case from LEF is discussed in this section.

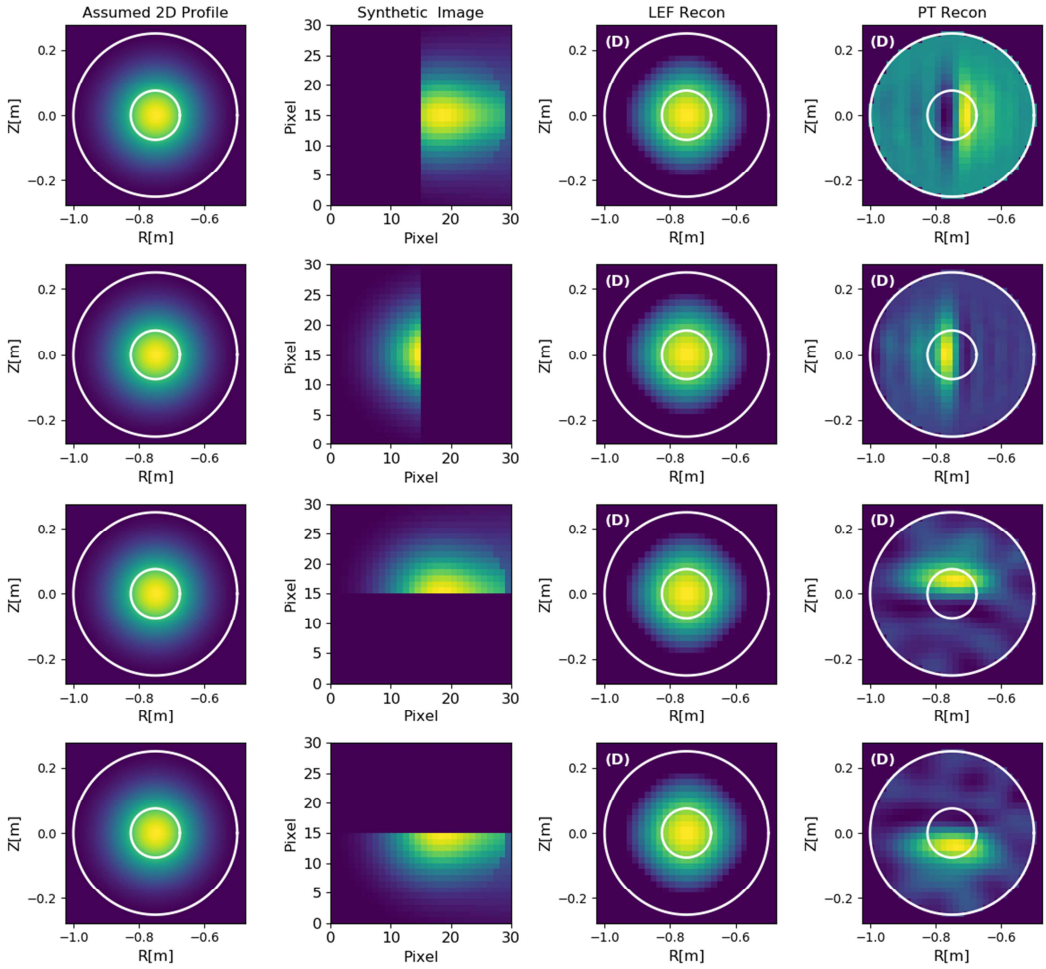


Figure 10. The assumed profile, Synthetic image, the LEF and PT reconstruction are shown in the respective column. The rows represents different synthetic image for the circular cross-section case.

The tokamak plasma is considered for this study and only 50% of the synthetic image of the line integrated emission is employed for the recovery of the 2D emission profile. The results for circular cross-section are shown in figure 10 and horizontally elongated plasma in figure 11, where the different orientation of the restrictions is considered to recover the 2D plasma emission profile. The first column represents the assumed 2D profile the second column shows the synthetic image employed for the reconstruction. The third and fourth column shows the reconstructed 2D emission

profile from LEF and PT, respectively. The images are made over 60x60 pixel grid for the LEF and 30x30 for PT.

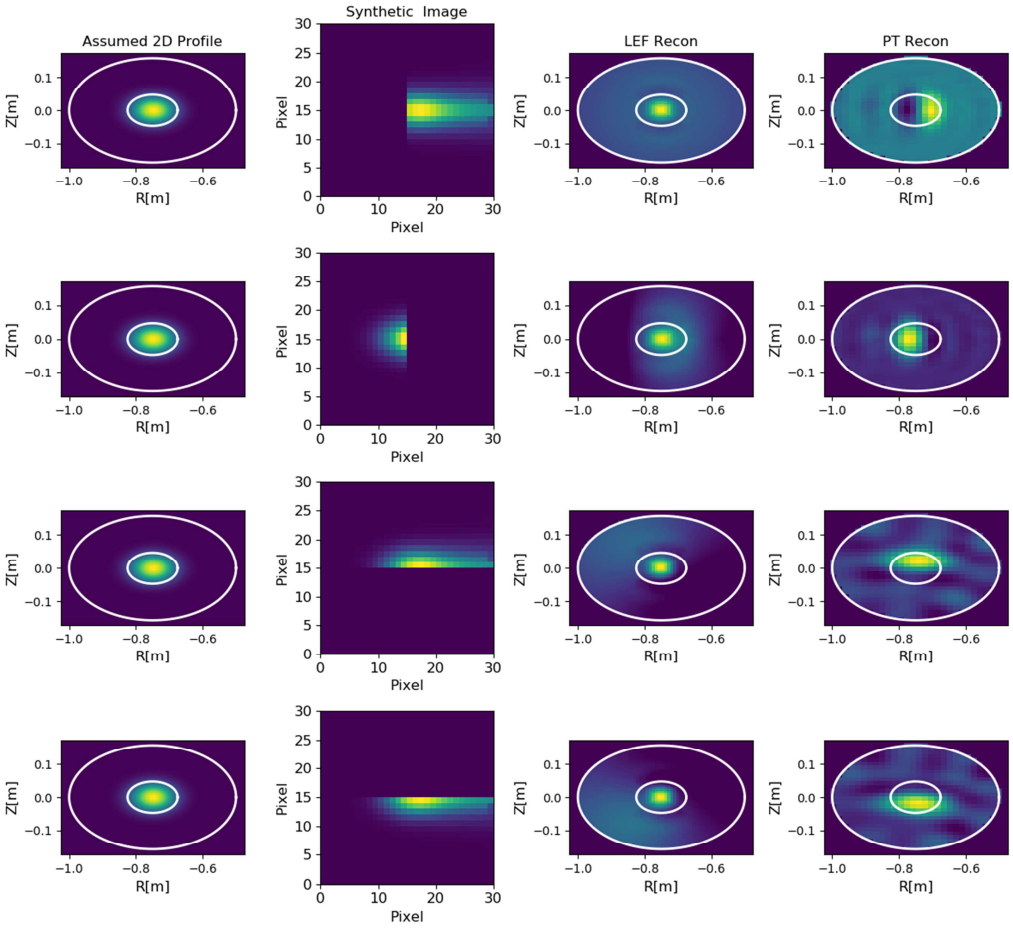


Figure 11. The assumed profile, Synthetic image, the LEF and PT reconstruction are shown in the respective column. The rows represents different synthetic image for the horizontal elongated cross-section case.

The reconstructions for the restricted viewing case, figure 10 and 11, it is clear that the LEF methodology is capable enough to recover the 2D emission profile even with the restricted view of the diagnostic. The standard Philip-Tikhonov regularization does not work well for the restricted viewing conditions. The reason for such behavior is attributed to the fact that the PT is a regularization assisted least square approximations based methodology. So in case of any absence of the diagnostic data,

restricted view, the efficient fitting cannot be made to recover the reliable tomographic image. In contrast the LEF being global patterns are able to recover the 2D emission profile.

Investigating in detail quantitatively the 1D profiles are recovered from these LEF reconstructed images and compared with the assumed profile. The comparison is shown in figure 12. All four images are able to predict the magnetic axis position clearly and are coherent to the assumed profile. The $d^2$ values for the LEF reconstructions are between 2.97% to 4.38%.

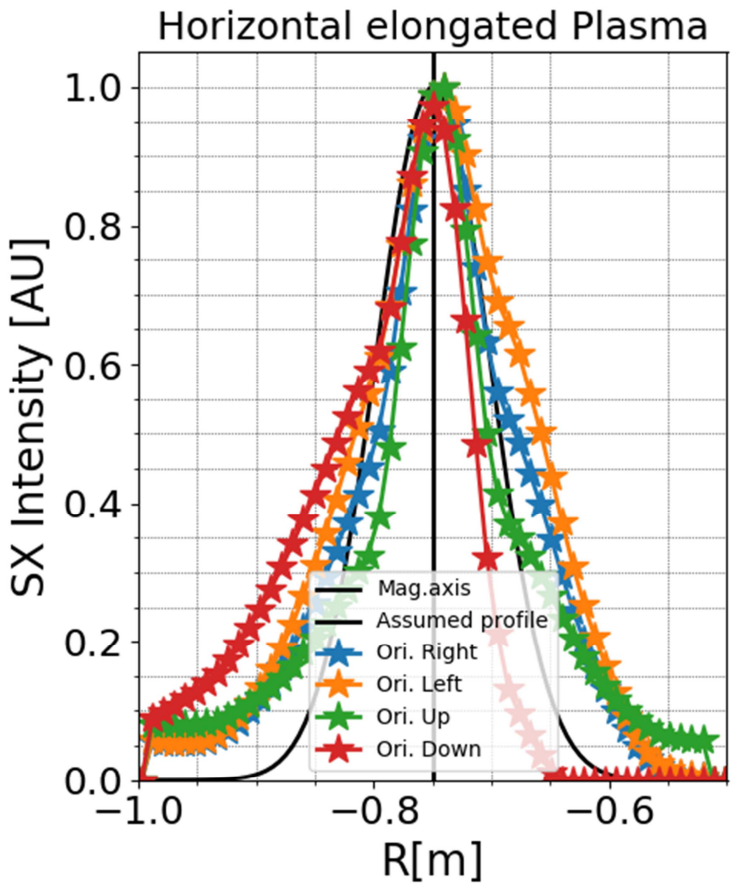


Figure 12. The recovered 1D profiles from the four different LEF reconstructed images, along with the assumed profile and the magnetic axis location.

The LEF method is investigated for the tangential viewing, complete and restricted case. The performance of the LEF is found to be comparable with the standard Philip-Tikhonov regularization for the complete view case. However for the restricted viewing case the LEF performance is far better with respect to the standard Philip-Tikhonov regularization reconstruction method.

## References

[1] Tingfeng M 2012 *Development of High-speed Vacuum Ultraviolet Imaging Camera System for High-temperature Plasma Diagnostics* (The Graduate University for Advanced Studies, Japan)

# Chapter V

# LEF for Heliotron J


## Abstract

LEF based tomographic reconstruction application to the Heliotron J (H-J) device (experimental data) is explained here. The identification of the magnetic axis location at different plasma $\beta$. LEF performance evaluation is also attempted here in this chapter.

High performance and stable plasma leading to fusion stage are prescribed by the nature of particle/energy transport within the plasma, stability towards MHD activities especially at high beta operation, and effective plasma heating. Mentioned parameters are greatly influenced by the design of the magnetic confinement device, in particular the magnetic geometry and the heating strategy. Heliotron J (H-J) device is one of the examples where the magnetic geometry is uniquely designed to enhance the plasma parameters.

## 1. Heliotron J device

The Heliotron J (H-J) device is a single helical axis mid-sized heliotron device which aims to experiment the concept of '*Omnigenity*' and explores the compatibility of the best possible particle confinement and Magneto-Hydro-Dynamic (MHD) stability.

Table 1. The Heliotron J information.

| | | |
|---|---|---|
| Coils for magnetic configuration | | ▪ Single helical coil($l$=1)<br>▪ Two kinds of toroidal coils<br>▪ Inner vertical coil<br>▪ Outer vertical coil |
| Major radius ($R_o$) | *m* | 1.2 |
| Minor radius (a) | *m* | <0.25 |
| Toroidal period | *N* | 4 |
| Toroidal field (B) | *T* | <1.5 |
| ECH Power $P_{ECH}$ | *kW* | <500 |
| NBI Power $P_{NBI}$ | *kW* | <700 x 2 (co. and ctr.) |
| ICRF Power $P_{ICRF}$ | *kW* | <2500 |
| NBI Energy $E_{NBI}$ | *keV* | <30 |
| Working gas | | H,D |
| Rotational transform | | 0.4~0.7 |

Heliotron J device is configured as *L/M* = 1/4 helical coil with a plasma major radius, $R_o$ = 1.2 *m*, and minor radius, a = 0.2-0.3 *m*, respectively. The H-J device is configured to have low shear across the plasma, $\acute{\imath}$ = 0.4-0.7. Two dedicated toroidal coils excite the toroidal field on the magnetic axis to $\boldsymbol{B}_{t0}$ ~1*T* and control the bumpiness in the toroidal field. The plasma heating for H-J is performed by ECH 0.5 *MW*, NBI 1.5 *MW*, and ICRF 2.5 *MW*, which results in high temperature and density plasma. H-J is equipped with a range of diagnostics, facilitating the studies of different aspects of H-J plasma, including MHD equilibrium and stability, Transport and Flow, Turbulence, and Energetic particle. Table 1 formally defines the Heliotron –J device in terms of plasma and device parameters.

## 2. Heliotron J – The Concept

The Heliotron J has three major pillars which make this device as one of the important plasma device, physics concept, engineering design and the diagnostics. Every one of them makes a significant impact on the plasma performance of the H-J.

### 2.1 Physics concept

The Heliotron J belongs to the comprehensive array of the '*Quasi-Poloidally Symmetric Optimization*' devices with the continuous solo helical winding (*L*= 1)[1]. '*Quasi-isodynamic conditions'* is a situation where the poloidally closed contours of $\boldsymbol{B}$ leads to a significant improvement of fast-particle collision-less confinement (by definition) along with shrunken neoclassical transport with small bootstrap current[2]. The trapped particles observe enhanced '*Omnigenity*' especially at the straight section of the vacuum vessel due to degradation in $\nabla\boldsymbol{B}$ and curvature drifts, even at the higher of $\beta$ and presence of finite electric field (within the limits of L-mode operations)[3]. Heliotron J attains a local *quasi-isodynamic configuration* in the straight confinement section with the standard configuration. At this location magnetic field strength in the direction of the major radius is almost constant at the central cross-section, while the magnetic field lines there are found to be nearly straight. Which means that $\boldsymbol{B}$ varies on a flux surface only through a fixed linear

combination of the Boozer angles[4]. This ensures the reduction of the particle drifts and improves the particle confinement.

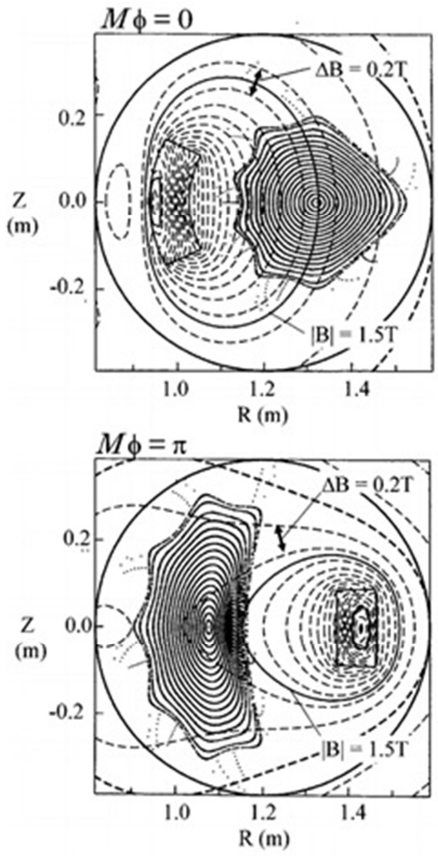


Figure 1: Poincar´e plots of typical vacuum magnetic surfaces (continues curves) at the corner section ($\varphi = 0$) top, and the straight section ($\varphi = \pi$). Broken curves denote contours of $|\boldsymbol{B}|$.

Consider the figure 1, where the vacuum flux surfaces of a typical H-J configuration with $\epsilon_b/\ \epsilon_h \approx -0.5$ at the half-radius, where $\epsilon_b$ is the bumpy component and $\epsilon_h$ is the helical component of the magnetic field strength, is shown for corner section ($\varphi = 0$), top, and the straight section ($\varphi = \pi$) , bottom[1]. The magnetic axis exhibits an excursion of 0.1 *m* within a circular chamber at $R_o = 1.2$ *m* across different $\varphi$ sections. The rotational transform at the magnetic axis is 0.54 and is almost constant in the whole region. As shown in bottom figure 1 the collision-less orbits of the deeply-trapped particles in the inner side of the torus are on the magnetic flux surfaces, thus

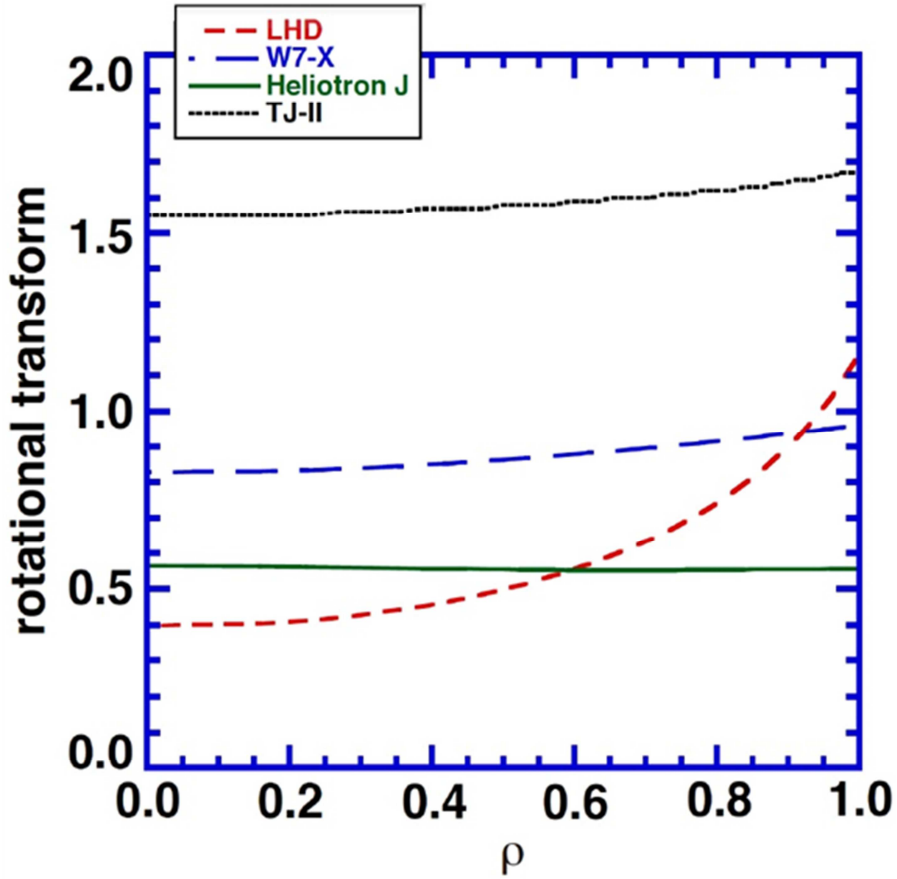


Figure 2. The rotational transform for different plasma devices, H-J magnetic –well span across whole vacuum region.

showing the local '*omnigenity*'. However at the corner section the trapped particles are that the outer side, figure 1 (top), which is one of the main contributors to the transport. The increase in the field at the corner section reduces such transport via trapped particles.

The MHD stability for Heliotron J is one of the important elements of the physics design. The conventional beta limit ($\beta_{eq}$), where magnetic the axis shift one half of the plasma minor radius, is ~ 5%, depending on the pressure profile. As mentioned the H-J has a low shear configuration, magnetic well covers the entire volume, see figure 2 [5]. The good depth naturally increases with increasing beta and the edge rotational transform shows a decreasing characteristic. This situation leads to the shear stabilization which is a comfortable position in terms of MHD stability. The bootstrap current, another agent which directly affects the plasma performance is

approximated to be zero, via adjusting the Fourier components of the magnetic field spectrum. The bumpiness in Heliotron J serves an additional control point for the boot-strap current properties.

## 2.2 Engineering design

The engineering design (ED) of the Heliotron J is very unique so to achieve the above-mentioned physics objectives. The coil arrangement, coil pitch, coil current, and vacuum vessel design are the core points over which the ED revolves.

The magnetic coils are the heart of any magnetic confinement plasma device and proper coil geometry and installation is key to successful plasma operations. H-J possess three different types of coils, helical field coil (HFC), Toroidal field coil (TFC), and poloidal field coil (PFC), respectively. Heliotron J possesses a continuous helical HFC with an L = 1/$M$ = 4 configuration and having a pitch modulation of $\alpha$ = -0.4, see figure 3. The HFC follows the winding law, with the variable $\theta$ ($\varphi$) is a poloidal (toroidal) angle.

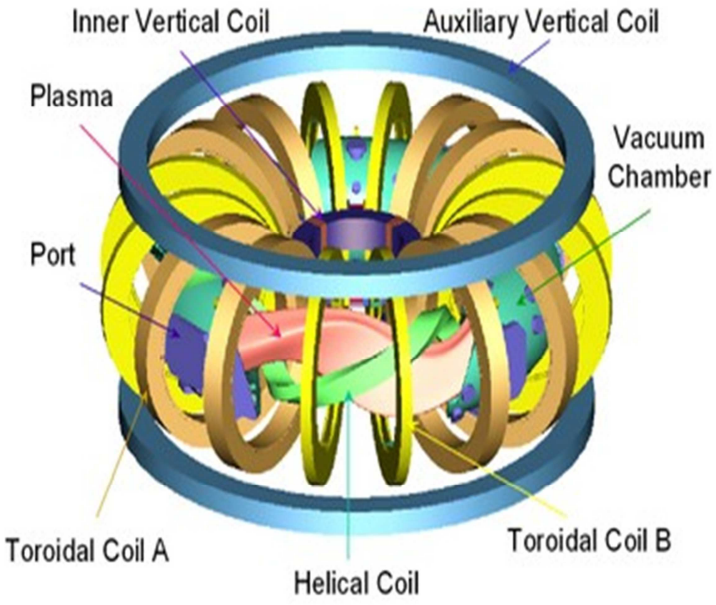


Figure 3: The coil arrangement at the Heliotron J, helical coil, poloidal field coil, and toroidal coil.

$$\theta = \pi + \left(\frac{M}{L}\right)\varphi - \alpha \sin\left\{\left(\frac{M}{L}\right)\varphi\right\} \qquad (5.1)$$

The coil pitch modulation is significant in designing the toroidicity component ($\epsilon_t = B_{1,0}/B_{0,0}$) of the magnetic field. $B_{m,n}$ is a Fourier component of magnetic field strength in the Boozer coordinates, where the subscript $m$ ($n$) denotes poloidal (toroidal) mode number. Positive values of α reduce the toroidicity component and subsequently reducing the Pfirsch-Schlüter current. However, in this situation, positive $\alpha$, the magnetic hill region widens –up and the plasma minor radius reduces. In the case of H-J where the magnetic –well spans across whole vacuum region need to have a negative pitch modulation, which effectively reduces the pressure-driven instabilities even at higher beta values ($\langle\beta\rangle \geq 3\%$). Another advantage of negative $\alpha$ is that the bumpy field component (toroidal mirror ratio) is easily controlled to reduce the neoclassical transport. Two sets of eight toroidal field (TFC) coils installed successively in the toroidal direction, see figure 3. The two sets of TFC coil have current values, $I_{TA}$ and $I_{TB}$, these are instrumental to control the bumpy component of the magnetic field, $\epsilon_b$. the maximum magneto-motive forces are 600 × 8 $k$A $T$ and 218×8 $k$A $T$, respectively, which excite the toroidal field on magnetic axis $B_{t0}$ of about 1$T$. The TFC also contributes to the control of the rotational transform.

The poloidal field coils (PFC) comprises of three types of coils, inner vertical coil (IVC), auxiliary mid-vertical coil (AMVC), and outer main vertical coil (OVC), see figure 3. The PFC is majorly employed for the plasma position and shape control via multipole field components. The vertical component provides a shift of the plasma position, which changes the magnetic well depth as well as the bumpiness. When beta increases, the use of the poloidal coils is a solution to prevent the breakup of the outer magnetic surfaces.

## 3. Heliotron J – Diagnostics

The Heliotron J (H-J) has a range of diagnostic covering different aspect of plasma physics, transport and flow, Turbulence, MHD equilibrium and stability, energetic particle. The typical diagnostic installation sight-map is shown in figure 4, along with

the heating and the pumping systems. Table 2 gives a brief overview of the diagnostics at H-J.

Table 2. The diagnostic for different aspects of plasma physics

| Physics Aspect | Type of diagnostic |
|---|---|
| Transport and flow | Nd: YAG-TS, CXRS, ECE, Hα array, FIR, Reflectometer |
| Turbulence | LP, BES, Fast camera |
| MHD equilibrium and stability | MP, SXCT, BES, ECE, Reflectometer, Saddle loop (SL), Magnetics |
| Energetic particle | NPA(E//B), DLP, Faraday-cup LIP (FLIP) |

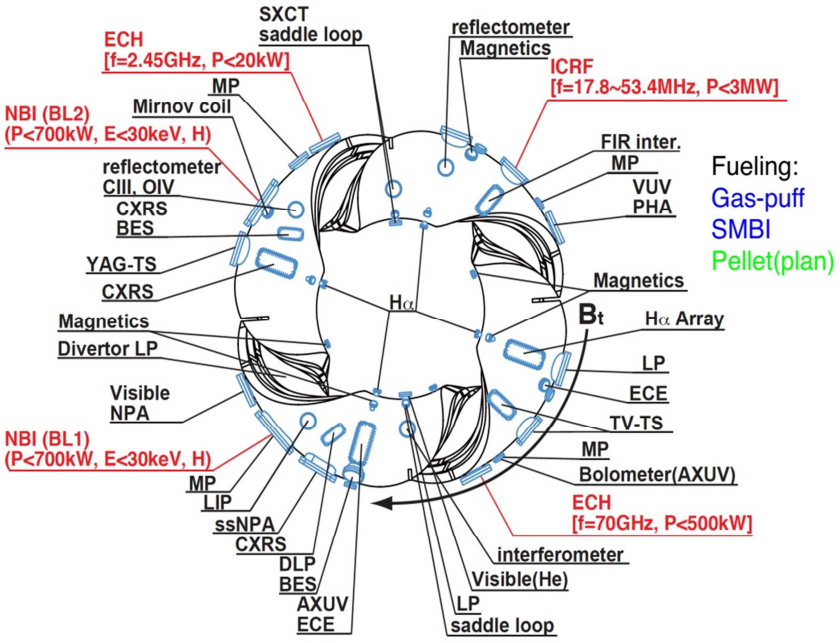


Figure 4: The diagnostic installation at Heliotron-J.

The Soft X-ray tomographic (SXT) system is a triad of SX detector arrays with a field of view (FOV) covering whole plasma cross-section, as shown in figure 5. The H-J plasma is enclosed with the vacuum vessel, shown in green. The SX arrays are installed

at the top, at the bottom, and at radial ports to constitute the complete viewing geometry. The FOV is governed by a rectangular pinhole, installed in front of the detector array, with a submillimeter poloidal opening.

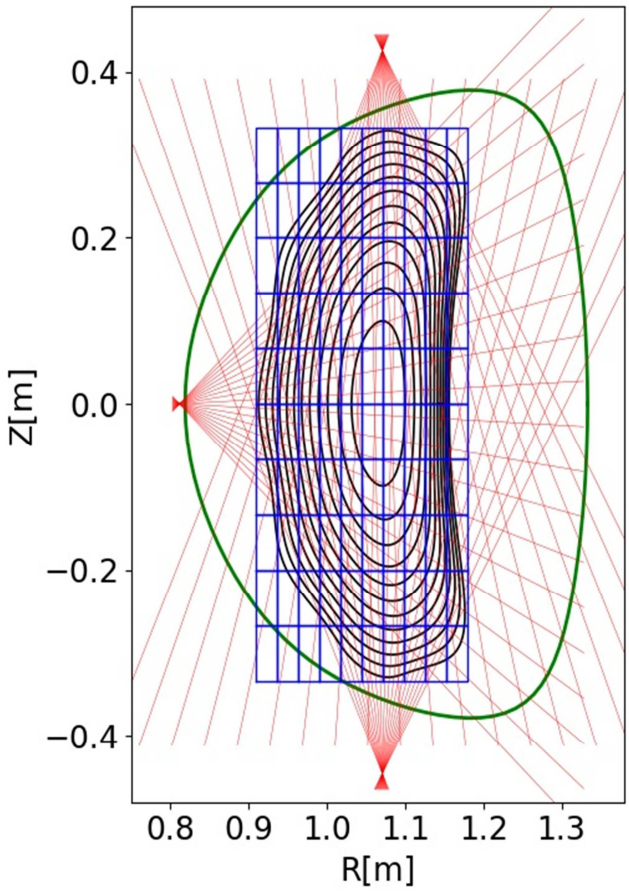


Figure 5: The viewing geometry for current SX design at H-J. Pixel grid (blue) shows the reconstruction area along with the vacuum vessel boundary (green). The LOS of individual detector red lines (red) views the plasma completely.

The SXT system is installed at $\varphi$ = 45$^{o}$ toroidal angle[10,11]. The AXUV20ELG arrays are employed in the H-J soft X-ray tomography system. This array harbors 22 detecting elements; however, only 20 elements participate in the SX measurements, leaving the edge detectors opaque. Thus, the system effectively offers a total of 60 lines of sight (LOS) for the SX measurements of H-J plasma (20 x 3 = 60)[12], shown with red color in figure 5. The detector array, engineering drawing is shown in figure 6 where each detecting element area is 0.75 *mm* x 4.1 *mm* = 3.075 $mm^2$. Interestingly there is a small gap between the two detecting elements 0.20 *mm*. An aluminum filter

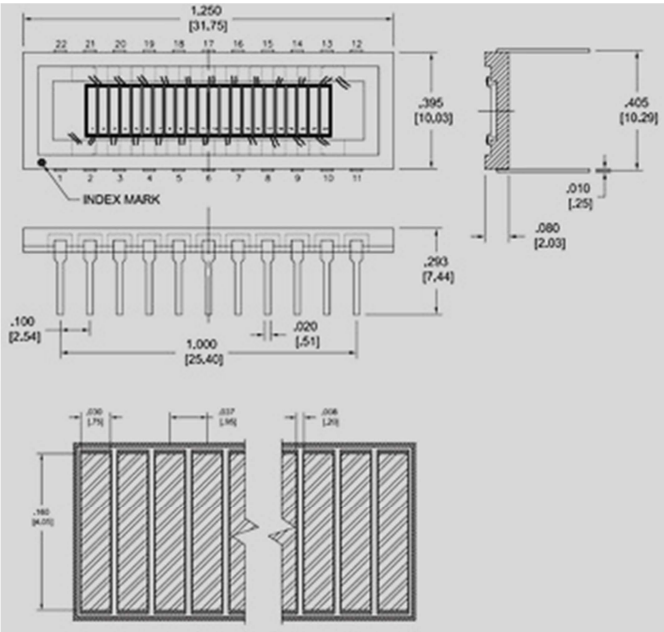


Figure 6: Engineering drawing for the AXUV20ELG.

is applied to these detectors for the low energy photons cut-off at ~0.75 keV. The detector arrays are connected with an efficient data acquisition system which converts the SX energy deposited in the detector into voltages as a function of time with an acquiring rate of 10 kHz.

## 4. Soft X-ray tomographic reconstructions

The typical Heliotron J discharge is shown in figure 7, for which the reconstruction is performed. The figure 7 represents time evolution of frequency spectrum of magnetic fluctuations obtained from the magnetic probe (MP1) (*a*), stored plasma energy, ECH, and two NBIs (*b*), line-averaged electron density and $H_\alpha$ (*c*), magnetic fluctuation amplitude for MP1 and plasma current (*d*), Carbon (III) and Oxygen (V) impurity (*e*), and SX signal bottom array (*f*) for H-J discharge No. #63300. Discharge is initiated with the introduction of ECH (0.17*s*) which can be seen as in the spike increase in the $H_\alpha$, $n_e$ signal. The frequency analysis (*a*) shows that high-frequency fluctuations ($f_{eq}$ > 20 kHz) appears from 0.19*s*. These fluctuations start reducing with the increase in the density and plasma internal energy, and eventually completely disappear by 0.22*s*. These fluctuations are most likely associated with the energetic ion-driven (EID) global

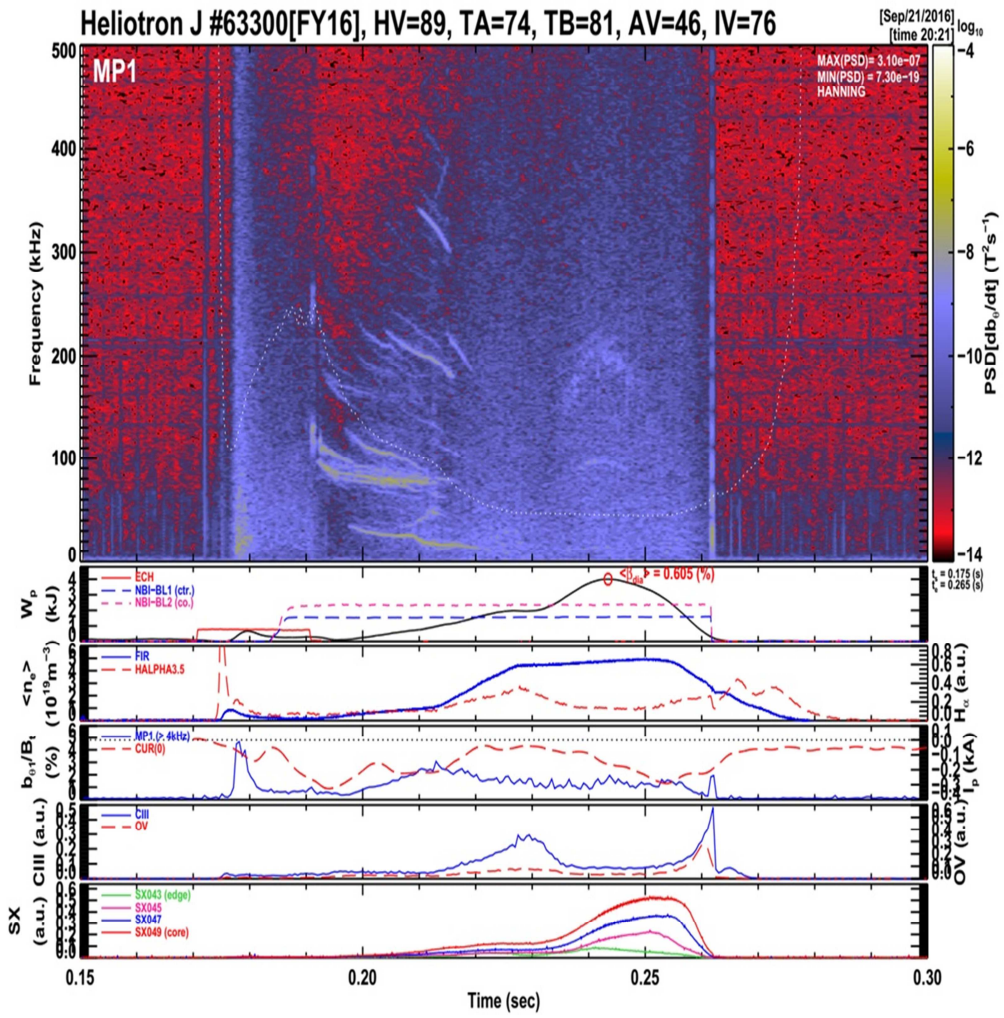


Figure 7: Time evolution of Heliotron J discharges #63300.

Alfvén eigenmodes. The two NBIs are employed ~0.185*s*, resulting in causing the plasma density to rise ~0.20*s*. As density starts increasing (0.20*s*) the soft X-ray signal improves and peaks at ~0.25*s*. The tomographic reconstruction is made at two different locations in time-space, first at 0.23*s* where the soft X-ray signal is quite low and second at 0.25*s* where the soft X-ray signal strength is considerably high, higher beta value. Referring to figure 7(*a*), Energetic ion driven fluctuations have frequencies greater than 20 kHz. Considering the fact that the SX diagnostic data acquiring rate is 10 kHz, the recovery of these mode structures is not possible with the current data set.

The Soft X-ray signals obtained from the experiments consist of high-frequency noise, and filtering is required for quality tomographic reconstruction. The Fast-Fourier

transform filters the SX signals. The filtered signals can be seen in figure 8, where the raw signal (blue) from the central channel of the lower SX array and filtered signal (orange).

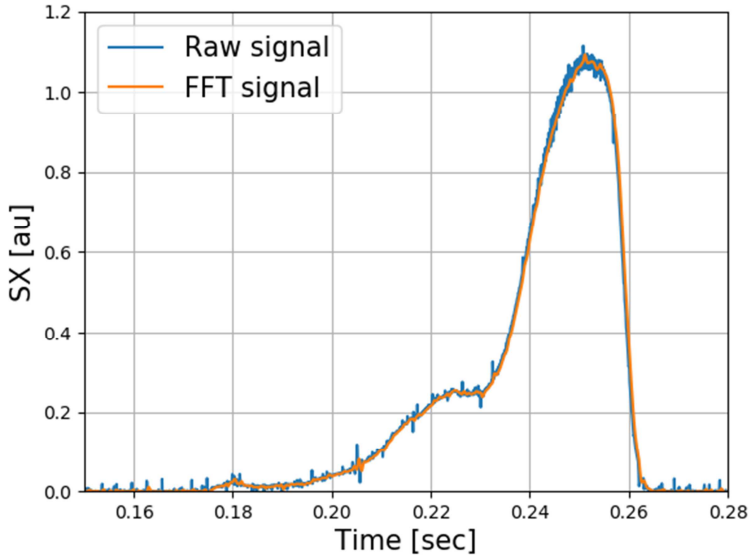


Figure 8: Raw signal (blue) and FFT based filtered SX signal (orange) from the central channel of lower detector array.

The application of the LEF based tomographic reconstruction is performed for the Heliotron J plasma. The reconstruction results are compared with the standard Phillips-Tikhonov (PT) regularization reconstruction method. The prime objective is to judge the performance of the LEF, by evaluating the location of the magnetic axis at two different plasma emission conditions, 0.23 *s* and 0.25 *s*, respectively. The soft X-ray line integrated data, after filtering, at these time location is shown in figure 9. The emission at 0.23 *s* is considerably low whereas at 0.25 *s* the plasma density and temperature is relatively high.

As the chronology of the reconstruction discussed in the previous chapter, first the LEF patterns are calculated for the Heliotron J plasma on the flux surface coordinates via estimating the 2D kernel. The typical kernel calculation shown in figure 10 (A) and the obtained patterns for first 12 Eigen values are shown in figure 10(B). These are the patterns which constitute the fundamental elements of the 2D emission profile determined by the LEF series expansion method.

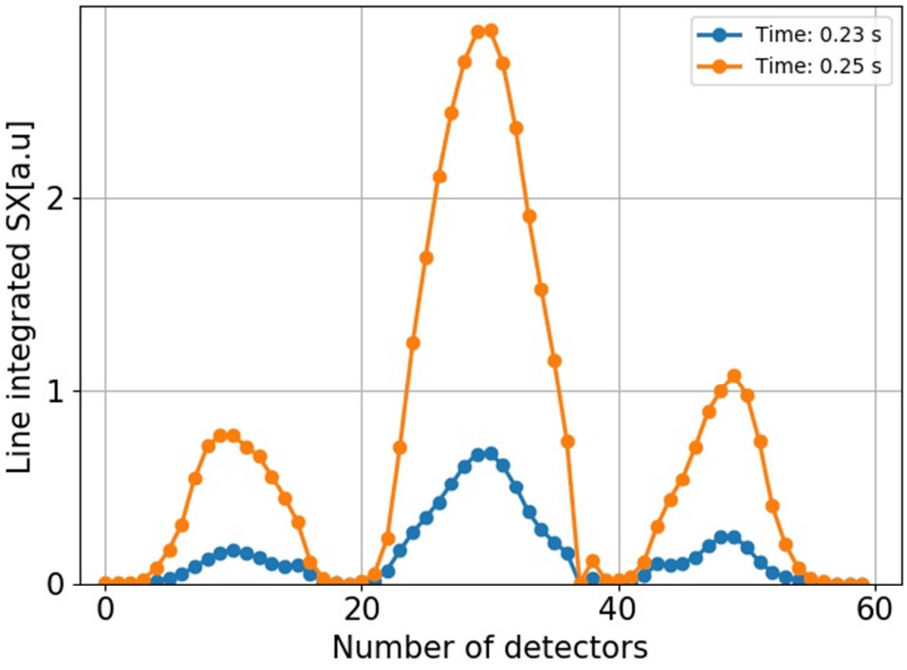


Figure 9: Line integrated soft X-ray at 0.23 *s* and 0.25 *s* as a function of channel number.

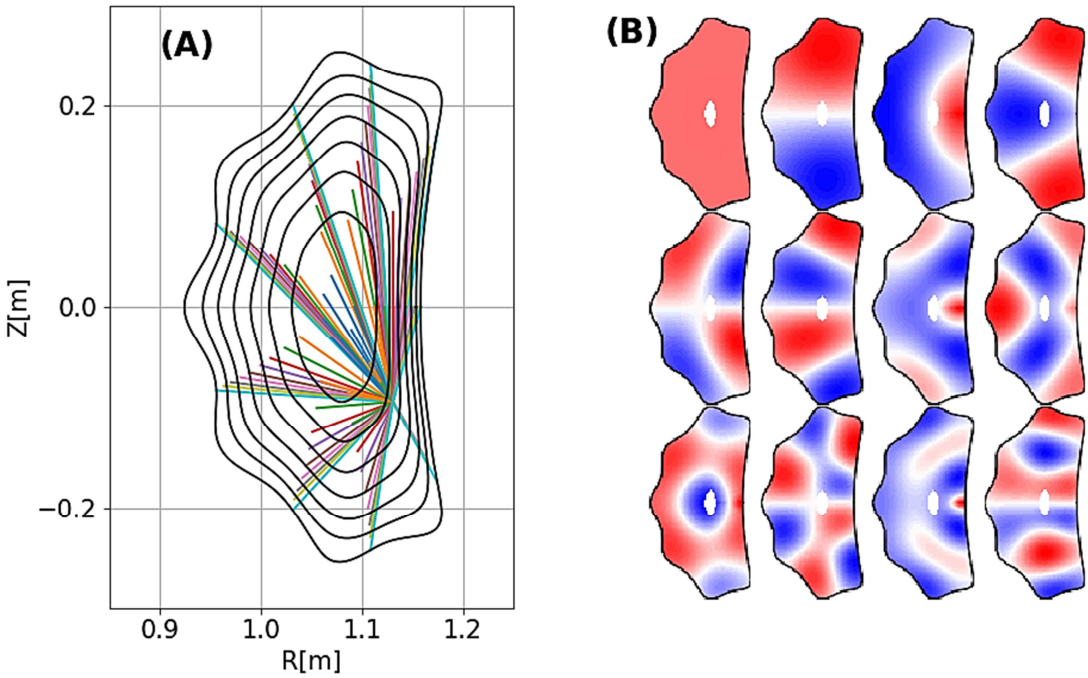


Figure 10: The kernel estimation over the H-J flux surfaces (A) and the subsequent generated LEF patterns corresponding to the 12 Eigen values.

The reconstruction results at 0.23 *s* are shown in figure 11, where the soft X-ray emission is low. The tomographic reconstruction via PT is shown in figure11 (B). The reconstructed image is made over a 20x20 pixel grid. The lower pixel grid is considered due to the fact that with higher pixel grid number over smoothening is expected.

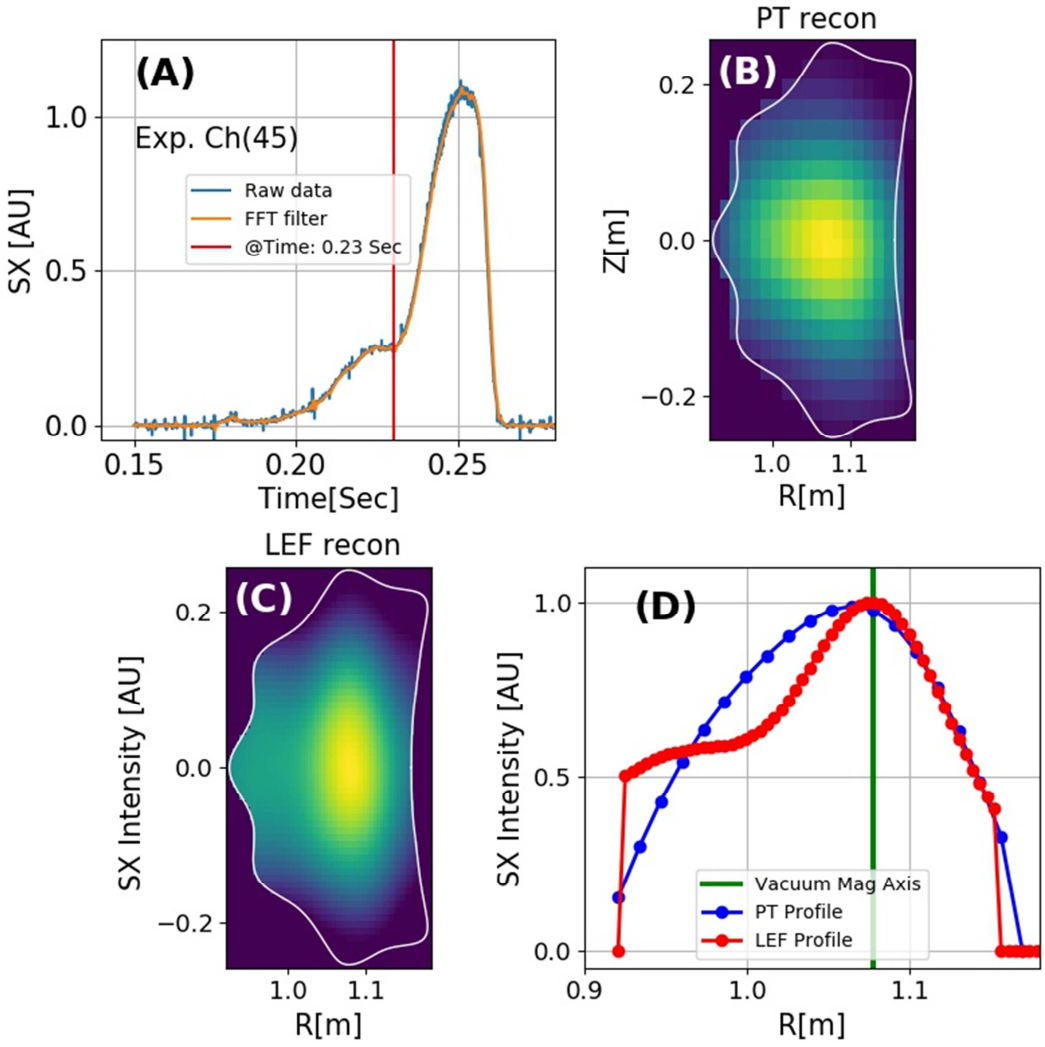


Figure 11: The reconstruction for time location, (A), by Phillips-Tikhonov, (B), and the LEF, (C) shown. The respective profile and vacuum magnetic axis is shown in (D)

The LEF tomographic reconstruction is shown in figure 11(C) and the image is made over 60x60 pixel grid. The LEF reconstruction is basically independent of the pixel

grid number, however, to recover the 2D emission profile the Eigenfunction patterns are discretized. Thus in principle the fine discretization of the patterns do not influence the results, unlike the PT. The 1D soft X-ray emission profiles recovered from PT and LEF are presented in figure 11 (D) along with the vacuum magnetic axis, estimated via VMEC code[13] . Both methods are able to recover the 2D plasma emission profile successfully. The 1D profile, in figure 11(D), the two methods are showing the magnetic axis location almost at the vacuum magnetic axis. Qualitatively speaking, the magnetic axis is expected to be almost at the vacuum magnetic axis location considering plasma conditions, lower density, temperature and plasma $<\beta_{dia}>$.

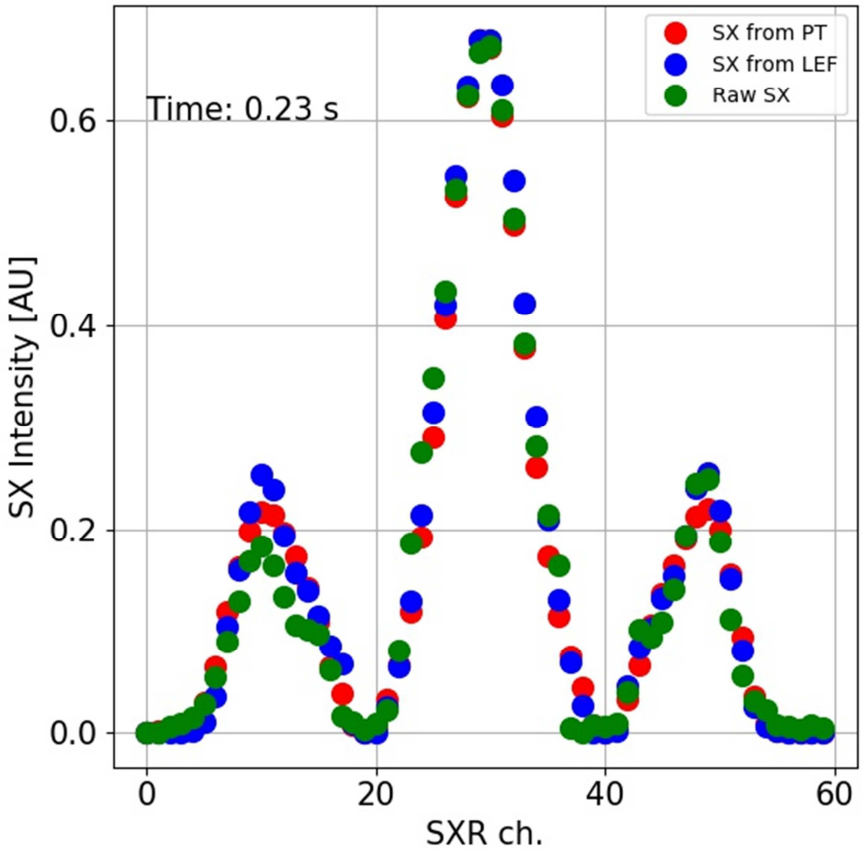


Figure 12. The comparison between line integrated soft X-ray data set from PT (red), LEF (blue) and the experimental (green) values.

The quantitative reliability of the reconstructions, PT and LEF, has to be evaluated. One of the approach to quantify the quality is the recovery of the line integrated soft

X-ray data from the two images considering the viewing geometry and comparing with the experimental data set. The comparison of the recovered line integrated soft X-ray signals with the integrated data from the two reconstructed images is presented in figure 12. The line integrated data from the two methods are comparable to the experimental soft X-ray data at time 0.23 *s*. This figure suggests that both the reconstruction possess the 'quantitative reliability'.

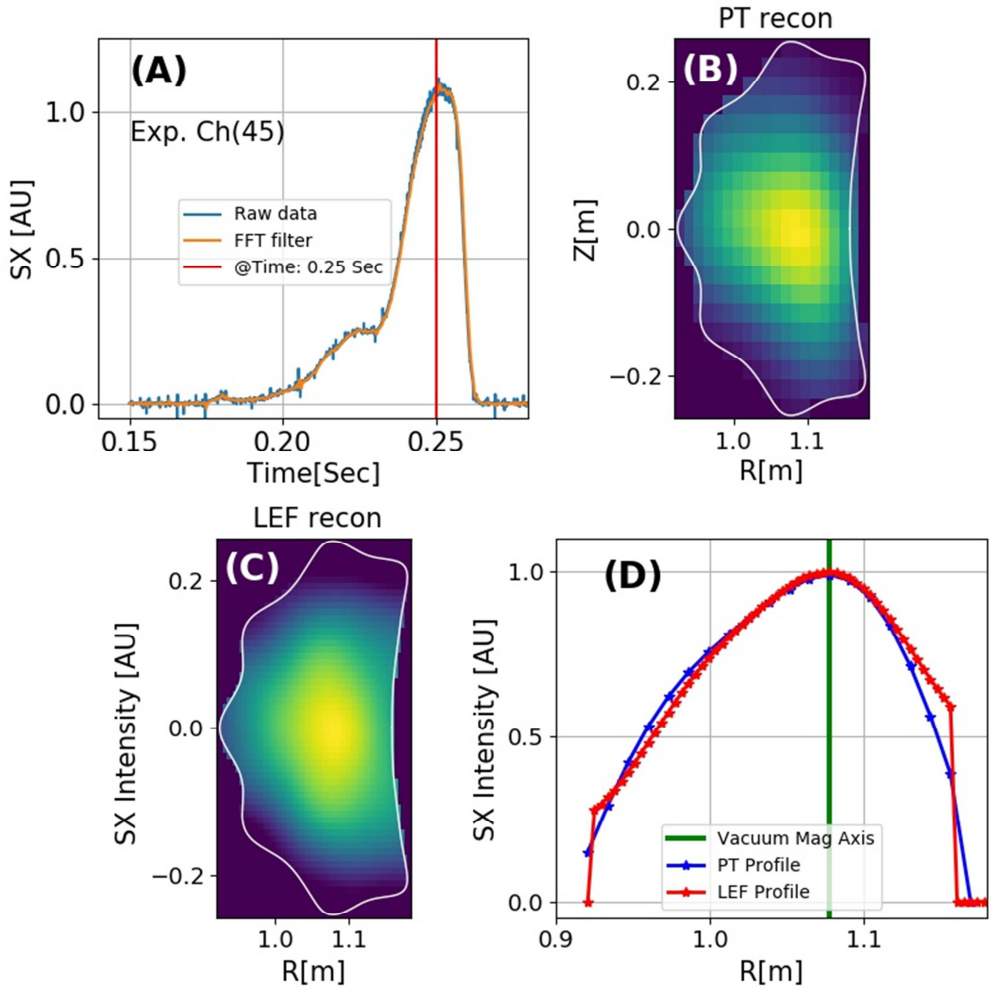


Figure 13: The reconstruction for time location, (A), by Phillips-Tikhonov, (B), and the LEF, (C) shown. The respective profile and vacuum magnetic axis is shown in (D)

The tomographic reconstruction at time location 0.25 *s*, where $<\beta_{dia}>$ *~0.6*% and plasma density $n_e$ ~4x$10^{19}$ $m^{-3}$, is shown in figure 13. The reconstruction from PT (20x20 pixel grid), figure 13(B) and LEF (60x60 pixel grid), figure 13 (C) shown respectively. The 1D emission profiles recovered from the two reconstructed images are shown in figure 13(D), along with the vacuum magnetic axis. The $<\beta_{dia}>$ ~0.605 %, at this time location suggests that the magnetic field geometry has not changed significantly from the vacuum magnetic geometry. Thus it is expected that the magnetic axis at this time has not moved very far from the vacuum magnetic axis location, ~1.077 *m*. Considering this important fact the two profile should predict the magnetic axis location near to the vacuum magnetic axis. The Thomson scattering data, for temperature and density, has a spatial resolution of 1 cm and with $<\beta_{dia}>$

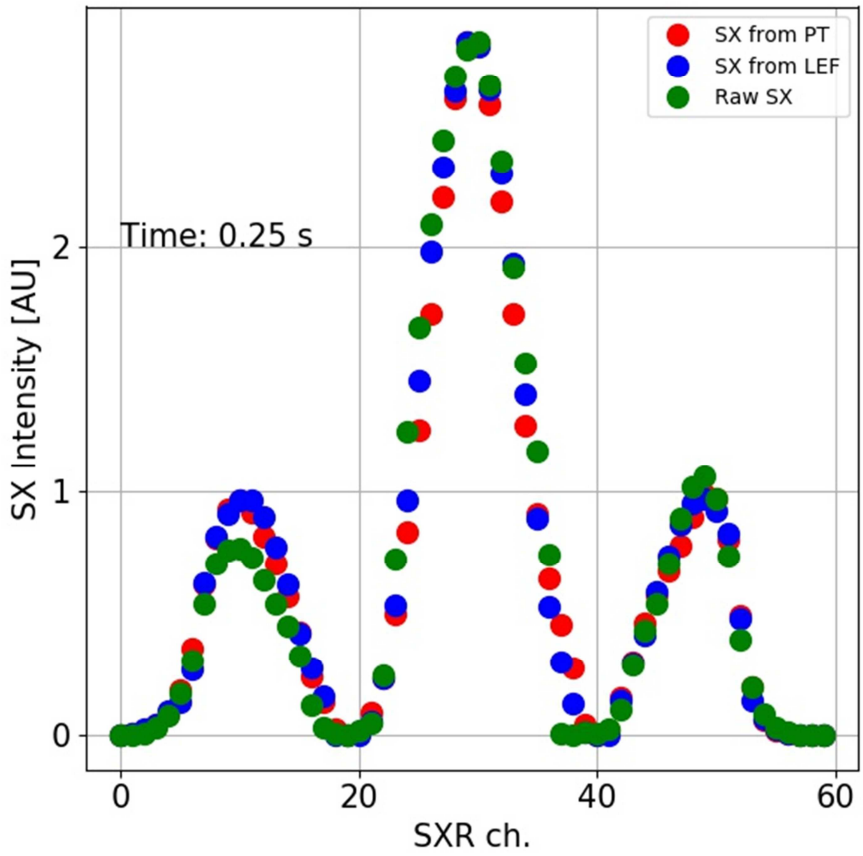


Figure 14. The comparison between line integrated soft X-ray data set from PT (red), LEF (blue) and the experimental (green) values.

~0.605 % it will be difficult to observe the magnetic axis shift. Thus such data set is not employed here to compare with the profile recovered from the Heliotron –J experimental results. Referring to figure 13 (D), both the 1D emission profiles are exhibiting the magnetic axis location near to the vacuum magnetic axis location. This result suggests the qualitative reliability of the reconstruction by the two methods.

The quantitative reliability is understood by again comparing the experimental line integrated soft X-ray data with the data recovered from the two reconstructed images and the comparison is shown in figure 14. The recovered line integrated data from the two reconstructions matches with the experimental SX values and strongly suggest that the construction is quantitatively reliable.

The normalized profiles from LEF are shown in figure 11 and figure 13. The emission profiles without normalization for LEF at two-time locations are shown in figure 15. The figure clearly establishes the difference between the emission profiles at these tow time location. The profile at 0.25 shows a clear higher emission at the center of the Heliotron J plasma.

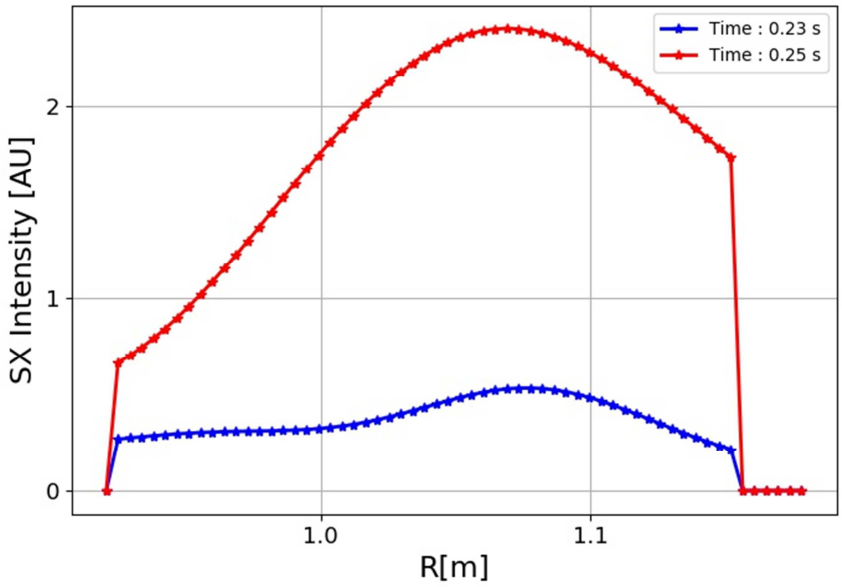


Figure 15: The 1D emission profile from LEF method at two time locations.

The first application of the LEF based reconstruction to the Heliotron J experimental data set and compared the performance with the standard Phillips-Tikhonov regularizations method is performed. The performance of LEF based reconstruction is found to be comparable to the standard Phillips-Tikhonov regularizations method. The LEF method was able to determine the magnetic axis location reliably along with the PT.

## References

[1] Wakatani M, Nakamura Y, Kondo K, Nakasuga M, Besshou S, Obiki T, Sano F, Hanatani K, Mizuuchi T, Okada H, Nagasaki K, Inoue N and Yokoyama M 2000 Study of a helical axis heliotron *Nucl. Fusion* **40** 569–73

[2] Mikhailov M I, Isaev M Y, Subbotin A A, Shafranov V D, Nührenberg C, Nührenberg J, Zille R and Cooper A *Quasi-isodynamic Configuration With N = 12 and High β*

[3] Obiki T, Sano F, Wakatani M, Kondo K, Mizuuchi T, Hanatani K, Nakamura Y, Nagasaki K, Okada H, Nakasuga M, Besshou S and Yokoyama M 2000 Goals and status of Heliotron J *Plasma Phys. Control. Fusion* **42** 1151–64

[4] Boozer A H 1982 Establishment of magnetic coordinates for a given magnetic field *Phys. Fluids* **25** 520

[5] Yamamoto S, Mizuuchi T, Nagasaki K, Okada H, Minami T, Kado S, Kobayashi S, Ohshima S, Nakamura Y, Konoshima S, Weir G M, Hada ) K, Kenmochi N, Otani Y, Lu X, Harada T, Hong Z, Kishikawa H, Isono R, Jinno Y, Kirimoto M, Kitani S, Matsuda H, Morimura T, Motoshima M, Murakami K, Nakano Y, Nakayama Y, Nishikawa K, Nuttasart A, Oda D, Suzuki A, Tei S, Yasueda M and Sano F 2015 Diagnostics Overview of Heliotron J *14th Coordinated Working Group Meeting* (Warsaw, Poland)

[6] Kenmochi N, Minami T, Takahashi C, Tei S, Mizuuchi T, Kobayashi S, Nagasaki K, Nakamura Y, Okada H, Kado S, Yamamoto S, Ohshima S, Konoshima S, Shi N, Zang L, Ohtani Y, Kasajima K and Sano F 2014 First measurement of time evolution of electron temperature profiles with Nd:YAG Thomson scattering system on Heliotron J *Rev. Sci. Instrum.* **85** 11D819

[7] Minami T, Arai S, Kenmochi N, Yashiro H, Takahashi C, Kobayashi S, Mizuuchi T, Ohshima S, Yamamoto S, Okada H, Nagasaki K, Nakamura Y, Hanatani K, Konoshima S and Sano F 2013 Present Status of the Nd:YAG

Thomson Scattering System Development for Time Evolution Measurement of Plasma Profile on Heliotron J *Plasma Sci. Technol.* **15** 240–3

[8] Lee H, Kobayashi S, Minami T, Kado S, Mizuuchi T, Nagasaki K, Okada H, Minami T, Yamamoto S, Murakami S, Nakamura Y, Hanatani K, Konoshima S, Ohshima S, Mukai K, Kagawa T and Sano F 2012 Measurement of Ion Temperature and Toroidal Rotation Velocity Using Charge Exchange Recombination Spectroscopy in Heliotron J *Plasma Fusion Res.* **7** 1402019–1402019

[9] Kobayashi S, Ohshima S, Kado S, Lee H Y, Minami T, Kagawa T, Mizuuchi T, Nagasaki K, Yamamoto S, Okada H, Murakami S, Suzuki Y, Nakamura Y, Hanatani K, Konoshima S, Toushi K and Sano F 2010 Development of Highly Spectral-Resolved Charge Exchange Recombination Spectroscopy in Heliotron J *J. Plasma Fusion Res. Ser.* **9** 59

[10] Nishikawa K, Yamamoto S, Mizuuchi T and Nagasaki K 2014 Studies of Magnetohydrodynamics Equilibrium and Stability by Using Soft X-ray CT in High Density Plasmas of Heliotron J *PLASMA CONFERENCE* ( Niigata , Japan) pp 19PA – 027

[11] Purohit S, Suzuki Y, Ohdachi S and Yamamoto S 2018 Improved design for Heliotron J soft X-ray diagnostic for tomographic reconstruction studies *Rev. Sci. Instrum.* **89** 10–102

[12] Anon AXUV20ELG Opto Diode Corp | Sensors, Transducers | DigiKey

[13] Hirshman S P and Whitson J C 1983 Steepest-descent moment method for three-dimensional magnetohydrodynamic equilibria *Phys. Fluids* **26** 3553

# Chapter VI

# LEF for LHD

Abstract

This chapter provides the discussion for the implementation of the LEF based reconstruction with tangential viewing geometry for the Large Helical Device (LHD) plasma, 3D plasma.

## 1. Introduction

Implementation of the Laplacian's Eigenfunction [1–4] for the tomographic reconstruction is discussed in the previous sections for the Heliotron J device, where the diagnostic is looking to the plasma perpendicularly to the magnetic field direction, and for tokamak (tangential viewing), which was symmetrical plasma. The discussion presented in this chapter is attributed implementation of tomographic reconstruction with tangential viewing geometry for the Large Helical Device (LHD)[5]. LHD plasma is a 3D helical plasma. The plasma is having a 3D nature and therefore, the Eigenfunction patterns have to be calculated in 3D.

## 2. Large Helical Device (LHD)

The Large Helical Device (LHD) machine aimed to study current less plasma with high temperature and density plasma and can attain $\langle\beta\rangle$ greater than 5%. Generation of such plasma offers a unique opportunity to understand the issue related to particle/ energy transport within the plasma and such understanding are intended to be extrapolated to the fusion grade plasma, the eventual convergence. Along with the stated objective other areas of interest covered by the LHD plasma physics study is the steady-state operations with the diverter configuration. LHD plasma also facilitates the study of high energy particles in the helical magnetic field which is helpful in conduct simulation experiments of $\alpha$ particles in reactor plasmas.

The magnetic coil configuration of LHD is shown in figure 1 where a pair of $L/M$ = 2/10 helical coils (H1; H2) [6] and three sets of poloidal coils, including the inner vertical (IV), inner shaping (IS) and outer vertical (OV) coils, are employed in LHD. These coils are superconducting coils, liquid helium cooling. Specifications of LHD and the main parameters of the superconducting coil system are listed in table 1.[7]

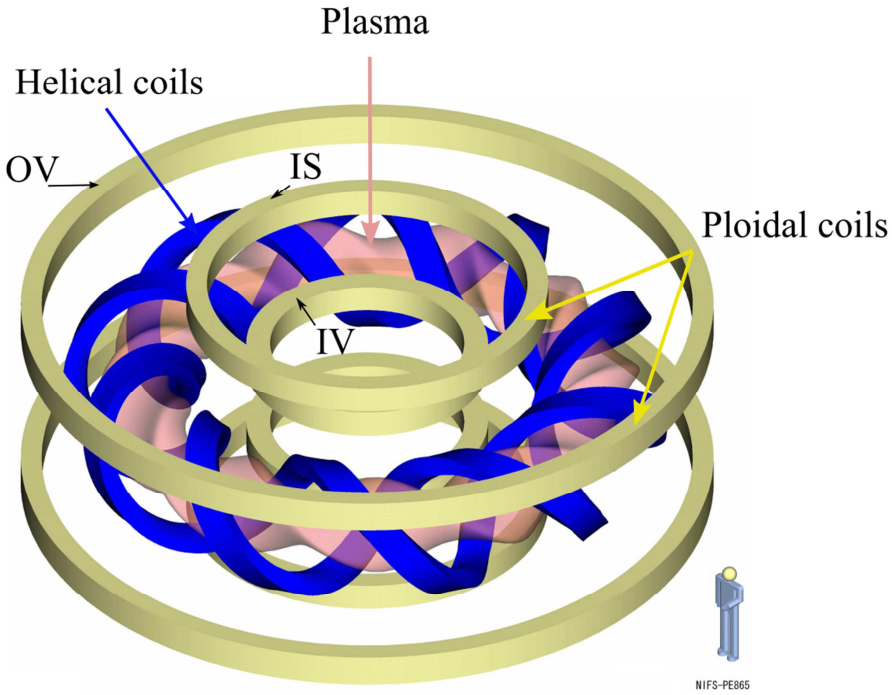


Figure 1: Bird view of the superconducting coil system and plasma shape of LHD

The LHD machine is having a range of diagnostic for the measurements of vital plasma parameters, like temperature ($T_e/T_i$), density ($n_e/n_i$), and MHD studies. Namely Thomson Scattering ($T_e$:5 *eV*-20 *keV* / $n_e$: $\geq 10^{18}$ $m^3$)[8], Electron cyclotron Emission (ECE)[9], Far-infrared laser and millimeter-wave interferometers, Soft X-ray diagnostic[10] Magnetic diagnostic[11]. The studies of plasma impurities are carried out by the spectroscopy diagnostic in the range of visible/ VUV range. Along with these interesting diagnostic LHD is also having a high-speed VUV telescope system which primarily provides the plasma images in the VUV range[12]. The tomographic reconstructions from line integrated VUV signals have shed light to plasma fluctuation studies for the LHD plasma and impurity transport studies[7]. The main goal of this chapter is to implement the LEF based reconstruction methodology for the LHD plasma, 3D plasma. In order to achieve the stated goal a step by step recipe is elaborated now.

Table 1: The LHD device parameters

| **Parameter** | **Unit** | **Value** |
|---|---|---|
| External Diameter | *m* | 13.5 |
| Major Radius | *m* | 3.9 |
| Minor Radius | *m* | 0.65 |
| Plasma Volume | $m^3$ | 30 |
| Magnetic Field | *T* | 3.0 |
| Total Weight | ton | 1500 |
| Heating power | MW | |
| ECH | | 10 |
| NBI | | 21 |
| ICRF | | 3-12 |

| **Coil Parameter** | | | | |
|---|---|---|---|---|
| | **Poloidal Coil** | | | **Helical coil** |
| | **IV** | **IS** | **OV** | **H1,H2** |
| Major Radius (*m*) | 1.80 | 2.82 | 5.55 | 3.9 |
| Maximum Magnetic field(*T*) | 6.5 | 5.4 | 5.0 | 6.9 |
| Number of turns | 240 | 208 | 144 | 450 |

## 3. Laplacian Eigenfunctions (LEF)

The first step of the LEF based reconstruction is the estimation of the Eigenfunction patterns by which the emission profile is recovered. The Eigenfunction are calculated on the LHD vacuum flux surfaces provided via VMEC code [13]. Estimation of the LEF patterns aligned to the flux surfaces makes the tomographic reconstruction smooth. The LHD plasma is 3D in nature, spinning oval in the toroidal space, thus the

Eigenfunction are estimated from the 3D kernel definition, refer to the third line of equation 3.3. Although the estimation is quite simple in its nature but presents expensive computing. In order to reduce the computations time the LHD plasma flux surfaces are configured in 16 (poloidal) x 16 (radial) x 160 (toroidal) grid, which can be considered as a low-resolution case. The Eigenfunction patterns corresponding to the first 16 Eigenvalues are shown in figure 2. The linear combination of such patterns is then employed for the tomographic reconstruction from the line integrated VUV / Visible / Soft X-ray data obtained from the imaging diagnostic.

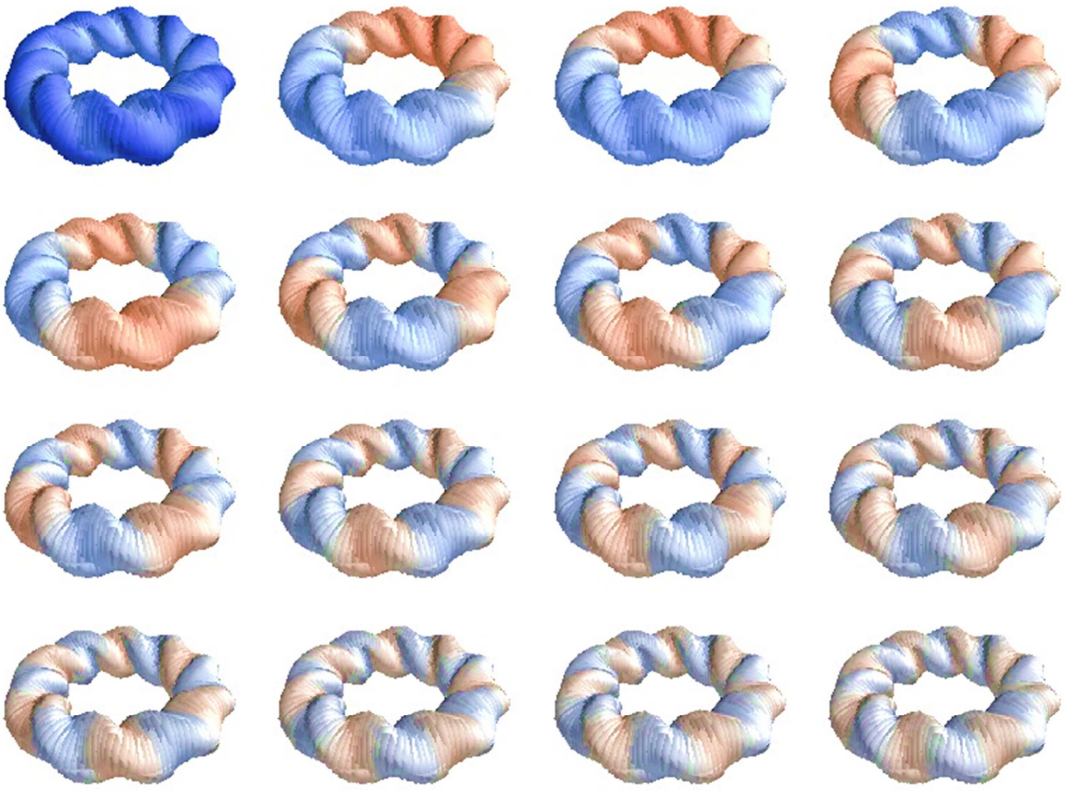

Figure 2: Eigen function patterns corresponding to the first 16 Eigen values for the LHD.

## 4. LEF capability estimation

Thus the first step is to check if the LEF are capable enough to build a simple Gaussian type of plasma emission profile. This step gives us the necessary confidence for attempting the reconstruction for any viewing geometry.

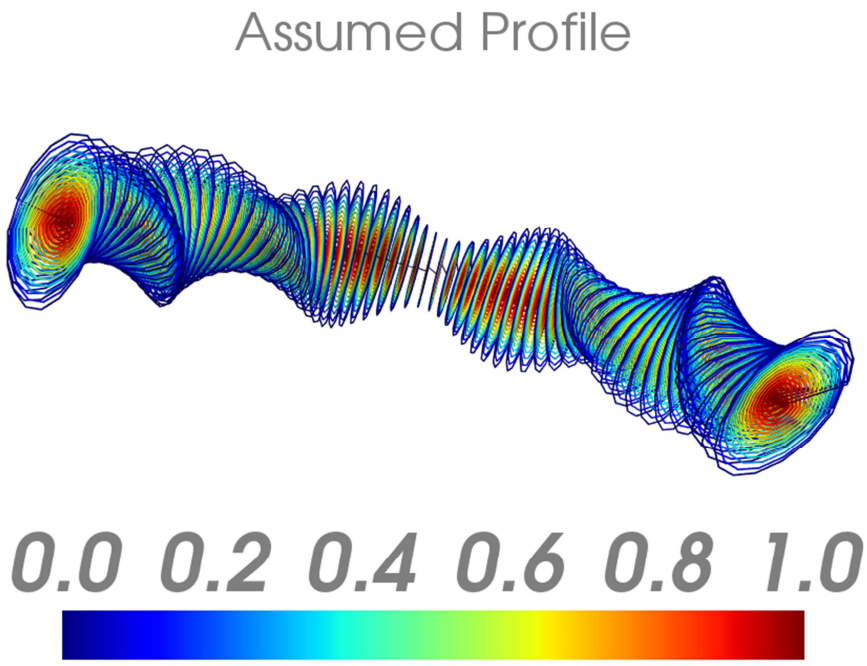


Figure 3: Assumed 3D emission profile

A simple Gaussian type emission profile is assumed for the LHD plasma, see figure 3. This 3D emission information is then employed along with the Eigen-function patterns, as shown in figure 2, to estimate the coefficients which can facilitate the recovery of the 3D emission profile, via equation 3.9. Since here we are not considering any viewing geometry so in equation 3.9 the contribution matrix information is omitted. The coefficients, first 1000 coefficients out of 40000, are shown in figure 4.

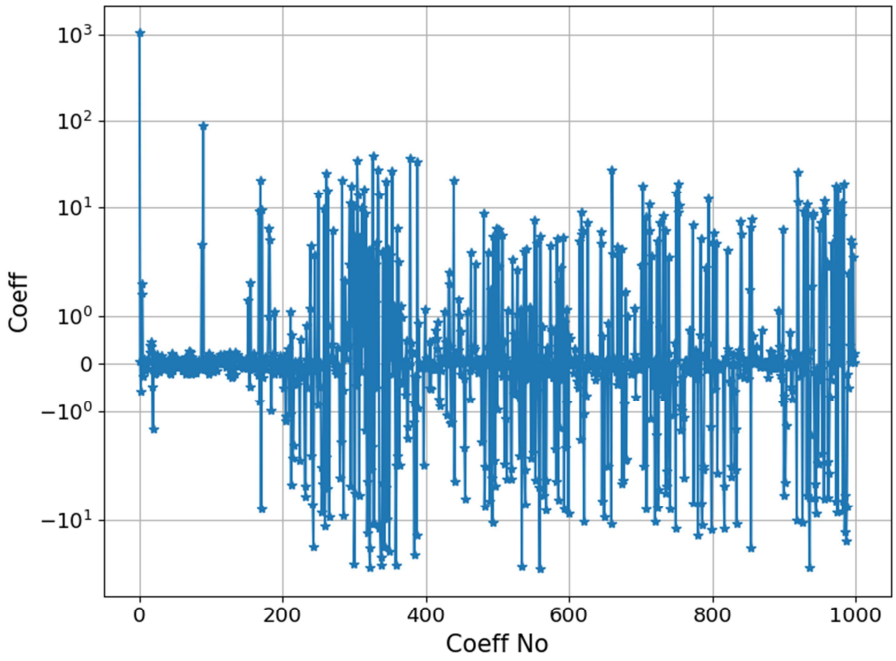


Figure 4: First 1000 coefficients for the recovery of the emission

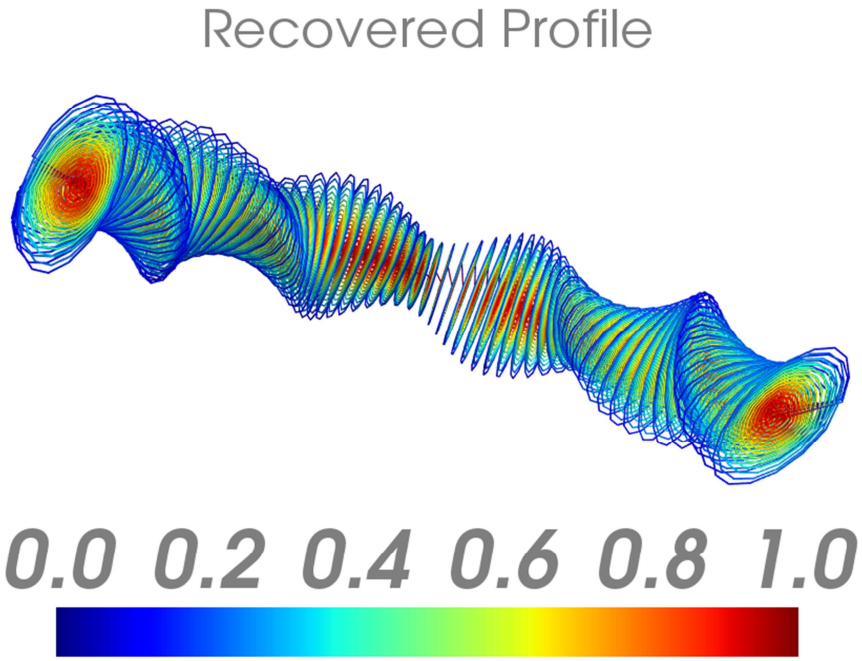


Figure 5: The recovery 3D emission profile.

Employing these coefficients and almost 20000 Eigenfunction patterns, the recovered 3D emission profile is shown in figure 5. The comparison of the assumed and the recovered profile is shown in figure 6.

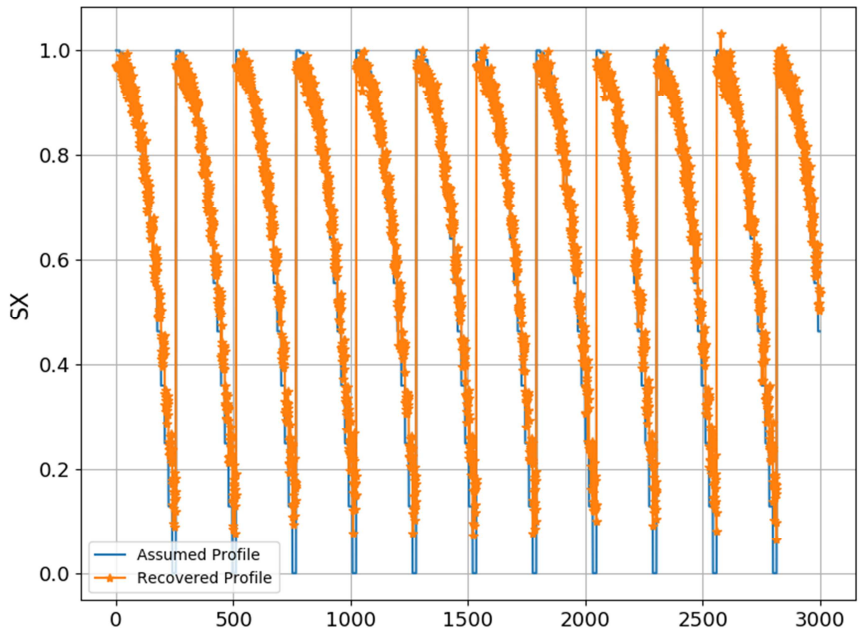


Figure 6: Comparison of the assumed profile and recovered 1D emission profile.

It can be said with confidence, from figure 5 and 6, that the LEF is capable enough to recover the emission profile, efficiently.

## 5. LEF reconstruction

The ultimate goal of this thesis is the implementation of the LEF based reconstruction for the 3D plasma with restricted viewing. Large Helical Device (LHD) is one of the eye-catching options to demonstrate LEF reconstruction. In the previous section we establish the fact that the LEF is capable enough to recover the 3D plasma shape. This section explores the reconstruction with proper viewing geometry. The reconstruction with the viewing geometry is divided into two sections. The first one is having the viewing geometry which views the complete plasma and second section

the viewing geometry is considered for the LHD VUV imaging diagnostic, which is having restricted plasma viewing.

## 5.1 Complete view

The viewing geometry of the imaging diagnostic for LHD plasma is shown in figure 7. The imaging diagnostic is considered to have a 30x30 pixel 2D detector array, offering 900 lines of sights.

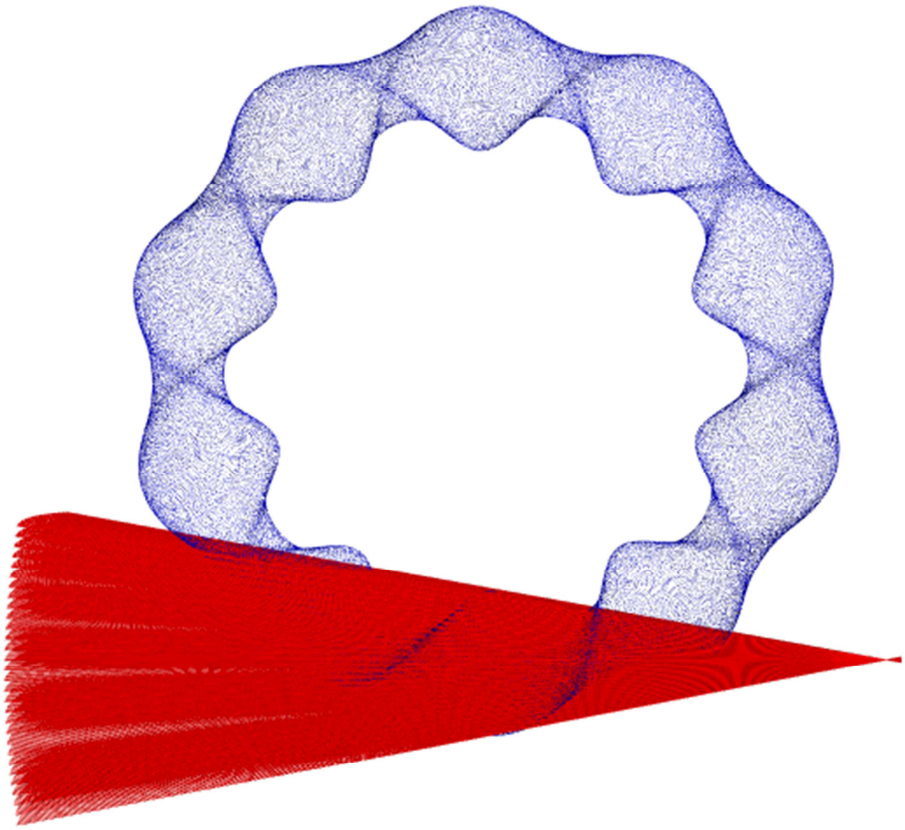

Figure 7: The viewing geometry, 30x30 pixel grid.

The 3D plasma shape is realized by the following steps

- Line integrated LEF is estimated

- Line integrated LEF are employed to fit with the line integrated data for the recovery of the expansion coefficients.
- Once the coefficients are available the linear combination of the LEF is performed to recover the 3D plasma shape and subsequent the line integrated image.

The line integrated LEF is basically the integration of a 3D pattern along a given line of sight. So in this case there are 900 lines of sights and we are having nearly 40000 LEF patterns so the line integrated LEF data will be a matrix, **X** in equation 7.1, with 900 rows and 40000 columns. Here we are using 16x16x160 LEF calculation grid, the line integration can be visualized by the figure 8.

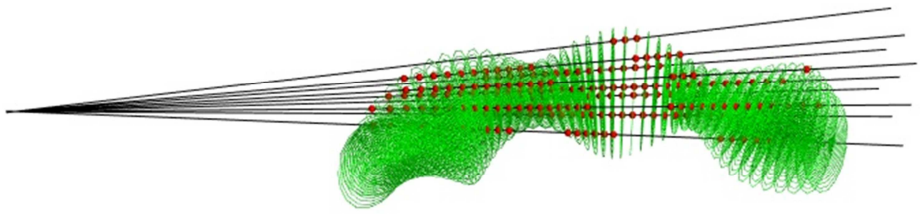

Figure 8: The integration of LEF along the line of sight.

The L1 type of regularization is employed here, $\alpha$=1, for the estimation of the expansion coefficients. L1 regularization optimizes the selection of the patterns and their weight in the realization of the plasma 3D shape. The expansion coefficients ($\beta$) is estimated via minimization of the following equation.

$$\underset{\beta}{\operatorname{agr\,min}}\left\{\sum_i (B_i - \beta_i \boldsymbol{X}_i)^2 + \gamma \sum_i |\beta_i|^{\alpha}\right\} \qquad (7.1)$$

The magnitude and the polarity of the coefficients are the deciding factors of the preciseness of the final results.

A Gaussian-like emission profile which represents a soft X-ray kind of emission was considered for the reconstruction of the LHD plasma via LEF based reconstruction method. The results for the reconstruction is shown in figure 9.

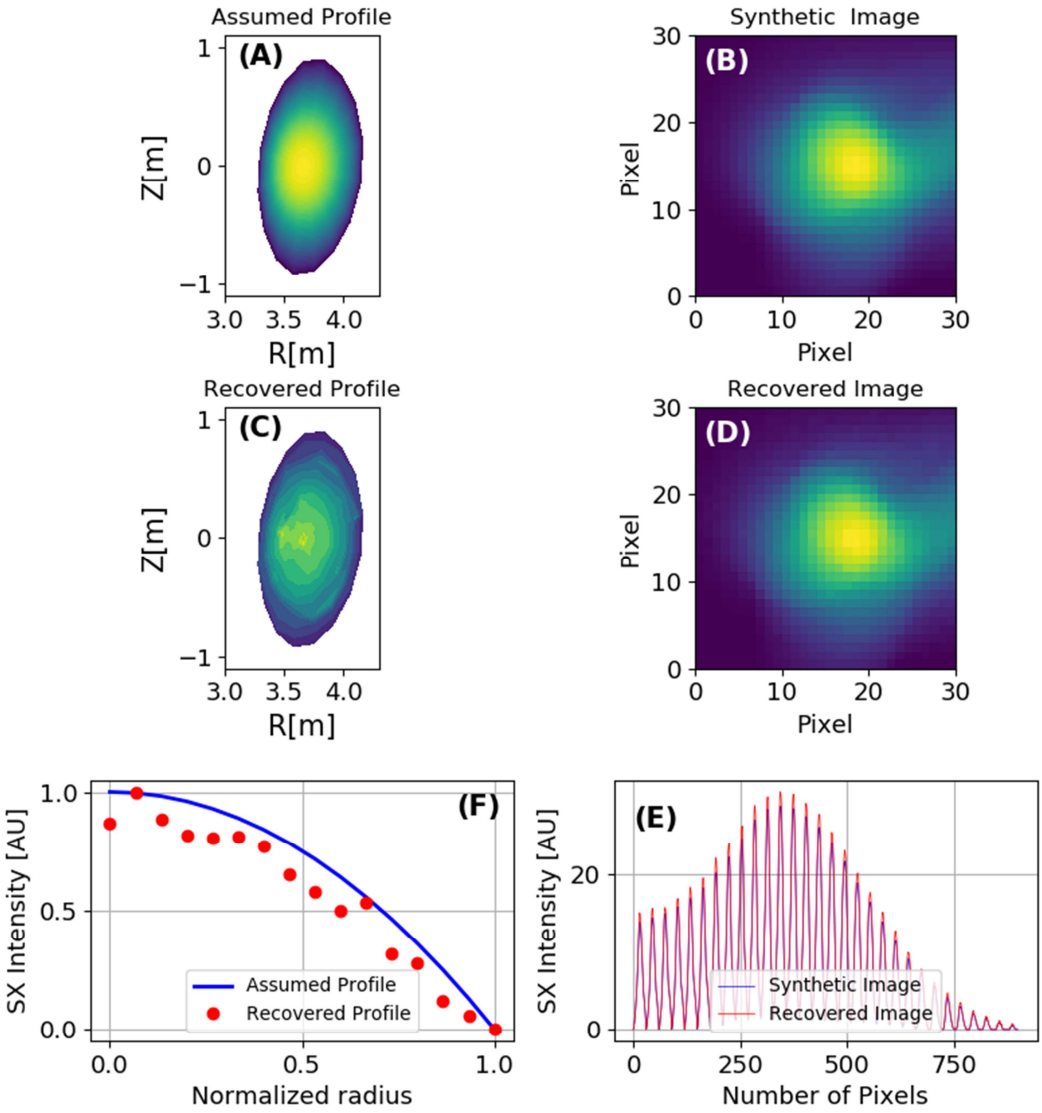


Figure 9: LEF reconstruction for LHD plasma Assumed Gaussian like emission profile (A), Synthetic Image(B), Recovered 2D emission profile (C), Line integrated image from the recovered 3D plasma emission (D), comparisons 1D emission profile(E), comparison between Synthetic Image and recovered line integrated image (F).

Where figure 9(A) shows assumed Gaussian-like 2D emission profile. Estimated synthetic image for the assumed profile considering viewing geometry is shown in figure 9(B). Figure 9(C) represents the recovered 2D emission profile and the line integrated image from the recovered 3D plasma emission in figure 9(D). The assumed 1D profile and recovered 1D profile are shown in figure 9(E). The synthetic image and recovered line integrated image are compared pixel-wise in figure 9(F). The LEF based reconstruction was capable enough to give a general realization of the plasma emission profile and subsequently the boundary shape. Considering the figure 9(E) and 9(C), the 1D/2D profile gives a general sense of the emission profile shape however, matching with the assumed profile is not very impressive unlike the previous cases with the tokamak. One of the argument which can be placed to explain such a result is, the relatively lower poloidal resolution of the LEF patterns. The LEF patterns considered here contains 16 poloidal points and 16 radial point, which seems to be not sufficient to have impressive poloidal/radial profile recovery. Comparing line integrated images pixel-wise, figure 9(F), the results are encouraging both the synthetic image and the recovered line integrated data are in a fair agreement. Although being insufficient poloidal /radial resolution of patterns the toroidal resolution is relatively high, 160 toroidal points, almost 10 times more, which is most likely the reason behind such encouraging results. Thus a key takeaway from these results is to increase the poloidal resolution of the LEF patterns in order to achieve a better understanding of the plasma emission and realization of the boundary shape.

## References

[1] Saito N *MAT 280: Harmonic Analysis on Graphs & Networks Lecture 6: Graph Laplacian Eigenvalues II*

[2] Saito N 2008 Data analysis and representation on a general domain using eigenfunctions of Laplacian *Appl. Comput. Harmon. Anal.* **25** 68–97

[3] SAITO Naoki 2016 Laplacian Eigenfunctions and Their Application to Image Data Analysis *J. Plasma Fusion Res. (in Japanese)* **92** 904–11

[4] Ohdachi S, Yamamoto S, Suzuki Y and Purohit S 2019 Tomographic inversion technique using orthogonal basis patterns *Plasma Fusion Res.* **14** 3402087

[5] Fujiwara M, Yamada H, Ejiri A, Emoto M, Funaba H, Goto M, Ida K, Idei H, Inagaki S, Kado S, Kaneko O, Kawahata K, Kobuchi T, Komori A, Kubo S, Kumazawa R, Masuzaki S, Minami T, Miyazawa J, Morisaki T, Morita S, Murakami S, Muto S, Mutoh T, Nagayama Y, Nakamura Y, Nakanishi H, Narihara K, Nishimura K, Noda N, Ohdachi S, Ohyabu N, Oka Y, Osakabe M, Ozaki T, Peterson B ., Sagara A, Sakakibara S, Sakamoto R, Sasao H, Sasao M, Sato K, Sato M, Seki T, Shimozuma T, Shoji M, Suzuki H, Takeiri Y, Tanaka K, Toi K, Tokuzawa T, Tsumori K, Tsuzuki K, Watanabe K ., Watari T, Yamada I, Yamaguchi S, Yokoyama M, Akiyama R, Chikaraishi H, Haba K, Hamaguchi S, Iima M, Imagawa S, Inoue N, Iwamoto K, Kitagawa S, Kodaira J, Kubota Y, Maekawa R, Mito T, Nagasaka T, Nishimura A, Takahashi C, Takahata K, Takita Y, Tamura H, Tsuzuki T, Yamada S, Yamauchi K, Yanagi N, Yonezu H, Hamada Y, Matsuoka K, Murai K, Ohkubo K, Ohtake I, Okamoto M, Satoh S, Satow T, Sudo S, Tanahashi S, Yamazaki K, Motojima O and Iiyoshi A 1999 Plasma confinement studies in LHD *Nucl. Fusion* **39** 1659–66

[6] Imagawa S, Masuzaki S, Yanagi N, Yamaguichi S, Satow T, Yamamoto J, Motojima O and Group L 1998 Design and construction of helical coils for LHD *Fusion Eng. Des.* **41** 253–8

[7] Tingfeng M 2012 *Development of High-speed Vacuum Ultraviolet Imaging Camera System for High-temperature Plasma Diagnostics* (The Graduate University for Advanced Studies, Japan)

[8] Yamada I, Narihara K, Funaba H, Yasuhara R, Kohmoto T, Hayashi H, Hatae T, Tojo H, Sakuma T, Yoshida H, Fujita H and Nakatsuka M 2012 Current status of the LHD Thomson scattering system *J. Instrum.* **7** C05007–C05007

[9] Kogi Y, Sakoda T, Mase A, Ito N, Yamaguchi S, Nagayama Y and Kawahata K 2007 Development of ECE Imaging System on LHD **2** 1032

[10] Bando T, Ohdachi S and Suzuki Y 2016 Developments of scintillator-based soft x-ray diagnostic in LHD with CsI:Tl and P47 scintillators *Rev. Sci. Instrum.* **87** 11E317

[11] Narushima Y, Watanabe K, Sakakibara S, Ohyabu N, Yamada H, Narihara K, Yamada I, Morisaki T, Inagaki S, Nagayama Y, Komori A, exp group L and Cooper W 2007 Magnetic Diagnostics of Magnetic Island in LHD **2** 1094

[12] Ming T F, Ohdachi S, Sakakibara S and Suzuki Y 2012 High speed vacuum ultraviolet telescope system for edge fluctuation measurement in the large helical device *Rev. Sci. Instrum.* **83** 10E513

[13] Hirshman S P and Whitson J C 1983 Steepest-descent moment method for three-dimensional magnetohydrodynamic equilibria *Phys. Fluids* **26** 3553

[14] Bayford R H, Gibson A, Tizzard A, Tidswell T and Holder D S 2001 Solving the forward problem in electrical impedance tomography for the human head using IDEAS (integrated design engineering analysis software), a finite element modelling tool *Physiol. Meas.* **22** 55–64

[15] Ferreira D R, Carvalho D D, Carvalho P J, Fernandes H and Contributors J *Regularization extraction for real-time plasma tomography at JET*

# Chapter VII

# Conclusion

The present tomographic reconstruction techniques like the Least –Squares Approximation or series expansion have their short-comings in handling irregular plasma cross-section, recovering the plasma emission profile with the restricted view of the imaging diagnostic, complex computing, inability to address the edge plasma reconstruction where high anisotropy is observed between parallel and perpendicular transport. With such short-comings it will be difficult for the present tomographic reconstruction methodologies to recover meaningful emission information for the future fusion reactors. Therefore a new method was designed and developed in this thesis to address the mentioned complexities of the tomographic reconstruction. The new reconstruction process is based on the laplacian Eigenfunctions which is employed for the 2D tokamak and 3D, Heliotron /Stellarator plasma

The series expansion method of tomographic reconstruction is considered for the new method, in which the emission is expanded into orthogonal functions. The Laplacian Eigenfunctions (LEF) is considered as the orthogonal patterns for which the linear combination of such patterns recovers the emission profile. The LEF holds eye-catching features which make the selection of LEF a good choice. The LEF is plasma domain/shape independent, can handle any type of plasma shape, due to the fact that these LEF are only the function of the distance between two points over the domain. Therefore LEF based reconstruction does not require the flux surface information in a prior to the reconstruction, only a rough domain boundary is required to realize the emission profile. As the LEF is the function of the distance, the high anisotropic region of the edge can be constructed conveniently.

The LEF reconstruction is applied to the tokamak type of plasma with a tangential viewing imaging diagnostic. The performance of LEF reconstruction was comparable with the standard Phillips-Tikhonov (PT) regularization. It was demonstrated that the LEF based reconstruction process is able to recover the emission profile for different wavelengths like the soft X-ray / VUV /Visible, even with the non-circular cross-section plasma. The most eye-catching feature on the LEF

was to address the restricted viewing geometry. The LEF was capable enough to recover the emission profile successfully where the standard Phillips-Tikhonov (PT) regularization methodology fails to perform. This is one of the key conclusion of this thesis.

The LEF based reconstruction procedure is applied to the Heliotron plasma, experimental soft X-ray data for the Heliotron J device for the realization of the magnetic axis location at different time location. The diagnostic viewing geometry is perpendicular to the magnetic field direction. The LEF performance was comparable with the Phillips -Tikhonov (PT) regularization, especially at higher $\beta$ plasma. LEF based reconstruction procedure is able to recover the emission profile and determined the magnetic axis location efficiently. The reconstruction was also able to reproduce the line integrated data which matched well with the experimental input SX data.

The LEF based reconstruction procedure is employed for the 3D Heliotron plasma, for the LHD device to realize the 3D plasma emission shape. The LEF was found to be suitable for such application as 3D LEF patterns were able to constitute the 3D plasma emission shape for LHD. This was possible due to the 3D nature of the LEF patterns. The reconstruction and subsequent realization of the emission profile via tangential viewing geometry was performed.

The LEF based reconstruction procedure with tangential viewing geometry, gives a general realization of the emission profile shape however matching with the assumed profile shape is not very impressive unlike the previous cases with the tokamak. The most likely reason for such a result is the relatively lower poloidal resolution of the LEF patterns (16 poloidal points and 16 radial point). Thus a key takeaway from these results is to increase the poloidal resolution of the LEF patterns. This argument is supported while comparing synthetic image and the recovered line integrated image pixel-wise, shows a fair agreement with each other as, the toroidal resolution of LEF patterns relatively high, 160 toroidal points, almost 10 times higher. So high-resolution LEF patterns are key to successful reconstruction.

Finally it can be said with confidence that the Laplacian Eigen Function (LEF) based tomographic reconstruction is capable enough to recover the plasma emission shape in 1D/2D/3D. For the first time the LEF is successfully implemented for tokamak plasma / Heliotron plasma. LEF efficiently handle the restricted viewing geometry, where the standard method fails. This is one of the strongest points of this method. However lengthy calculation, although easy and straight-forward, demand expensive computing. The thesis provides a base tool for the study of MHD equilibrium via tomographic reconstruction. This is also the first step towards the study of plasma instability as the tomographic reconstruction tool is now available.

## Future work

The Laplacian Eigenfunction (LEF) based reconstruction procedure proposed in this thesis is tested with different number of situations, which gives certain confidence to us to extend the study to more challenging problems. The future work in line with this thesis is elaborated below.

The leaking of impurities from walls or deliberated impurity seeding to fusion plasma is seen very often. The introduction of such impurities modifies the transport properties within the plasma. Especially the low '*Z*' impurities, like Carbon. This situation may lead to a minor temperature quench and enhanced radiation emission. These effects greatly depend on the penetration of the impurities within the plasma. Addressing such situation LEF based tomographic reconstruction can shed light to the characteristic of the impurity penetration within the plasma. One of the eye-catching proposals will be LHD, VUV camera which is designed to view the specific Carbon emission lines in VUV band. LEF based reconstruction will be helpful in the study for the LHD carbon pellet injection experiments. The LEF reconstruction in this thesis is mainly concentrated on the equilibrium plasma reconstruction. One of the important task for future is to extend the LEF reconstruction for the studies of the plasma instabilities for different plasma devices.

# Appendix I

# New design of SX system for Heliotron J

Abstract

Soft X-ray tomography system currently installed in Heliotron J is constrained in providing the quality images from the tomographic reconstructions for higher poloidal mode number structures. The chapter provides the modification aspect in the current design. The chapter also provides a new design for the SXT diagnostic for better performance.

## 1. Introduction

The Heliotron J soft X-ray tomographic diagnostic requires some improvements in order to develop a reliable tomographic image for the different mode structures. Different design and tomographic reconstruction aspects are addressed to explore the improvement possibilities. The efforts are divided into three sections. The first section deals with different reconstruction techniques, regularization assisted least squares approximations, and explores the best possible procedure for the H-J device. The second section addresses some modification in the current design in order to improve the reconstruction. The last section gives new designs for the H-J soft X-ray tomographic system.

## 2. Reconstruction procedure

The tomographic reconstruction can be performed by different procedures. A detailed discussion is given in chapter-II. The regularization-based reconstruction procedures like L1[1], Phillips-Tikhonov regularizations[2,3], Minimum Fisher Information (MFI)[4], and Maximum entropy regularizations (MEM)[5–7] are tested for the current SXT system of H-J. This testing is performed for low beta equilibrium plasma at lower (10 x 10) and higher pixel densities(40 x 40). The reconstructed images from different procedures are shown in figure 1. The top row of figure 1 represents the low pixel density, (10 x10) and the bottom row is for the higher pixel density (40 x 40). The plasma equilibrium flux surfaces are over-plotted, with black color in figure 1, on the reconstructed images for references. The reconstruction results for the L1 type regularization where the absolute values of emissions are considered as the penalty function P(E) = |E|, with no filter is shown in figure 1 (A) and (E). The L1 regularization at low pixel density completely fails to reproduce any shape of the plasma poloidal cross-section, figure 1(A). At higher pixel density, figure 1(E), the image is better in comparison with low pixel density but not qualified enough to be accepted. The reconstruction results from Phillips-Tikhonov regularizations, P(E) =

$|\nabla^2 E|^2$[8], is shown in figure 1 (B) and (F), reconstruction results at lower and higher pixel densities are able to give a realization of the plasma poloidal cross-section. The low pixel density image is unable to clearly locate the magnetic axis.This phenomenon is associated with the bigger pixel size. The reconstruction with higher pixel density is capable of realizing the magnetic axis within the error bar (pixel dimensions). The Maximum entropy regularizations (MEM) based reconstruction, P(E) = E ln (E), do not employes any filter unlike the Phillips-Tikhonov or Minimum Fisher thus the output images do show a bit noisy image. The results are given in figure 1(C) and (G), which shows that the process fails at the lower as well as at

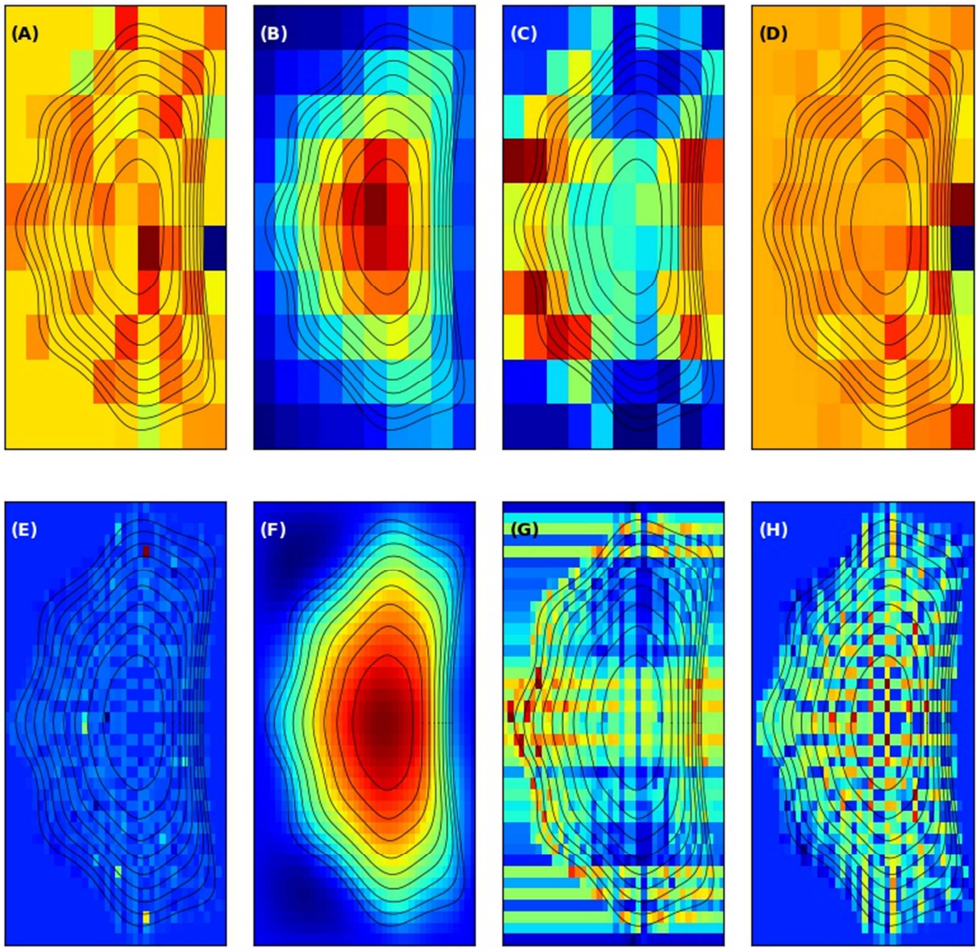


Figure 1: Reconstruction procedures, L1(A and E), Phillips-Tikhonov (B and F), Minimum Fisher Information (C and G), and Maximum entropy (D and H)

higher pixel density in reproducing the 2D plasma emission image. The Minimum Fisher information (MFI) regularizations, which is an extension of the Phillips-Tikhonov regularization, $P(E) = |\nabla^2 E|^2/E$, includes the Laplacian filter along with nonlinearity in the penalty function gives the reconstruction as shown in figure 1(D) and (H). As seen the procedure fails at lower density however, gives a proper realization of the plasma cross-section/plasma boundary shape. The reconstruction at higher pixel density is in-sufficient of giving a proper emission profile. Considering these facts the recommended reconstruction procedure for the H-J soft X-ray tomographic reconstruction is the Phillips-Tikhonov regularizations assisted least-square –error fitting

## 3. Design Modification

The modifications in the existing design of the soft X-ray tomographic system is addresses to some of the possible changes which can improve the reconstructed image quality. One of the drawbacks of the current design is about the fewer numbers of lines of sight which results in insufficient resolution. This section explores different aspects of increasing lines of sights to improve the quality of the image.

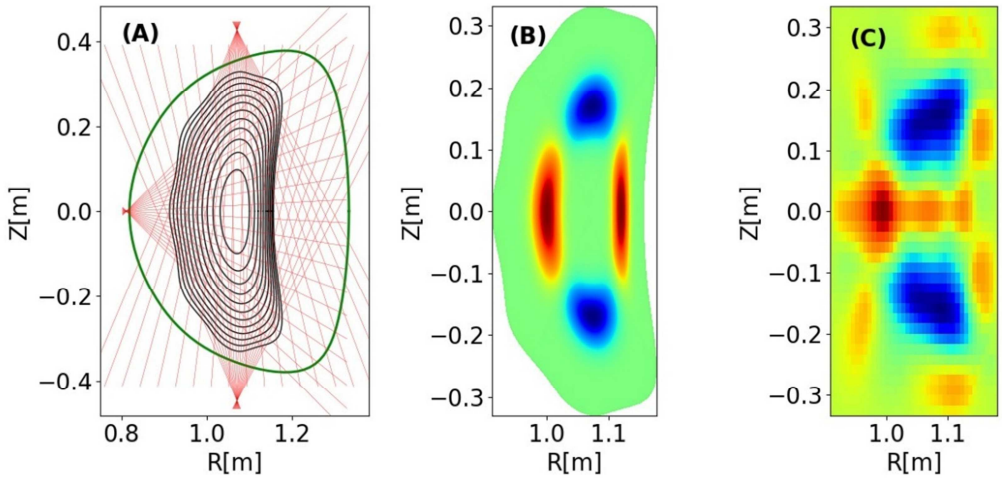


Figure 2: The viewing geometry (A), assumed emission profile of $m$=2/$n$=1 (B) and the reconstructed image(C) for the current SX tomography system.

For the reference the viewing geometry of the current design, in figure 2 (A), the assumed mode structure of $m$=2/$n$=1 emission profile, in figure 2 (B) and the reconstructed image shown in figure 2(C), respectively.

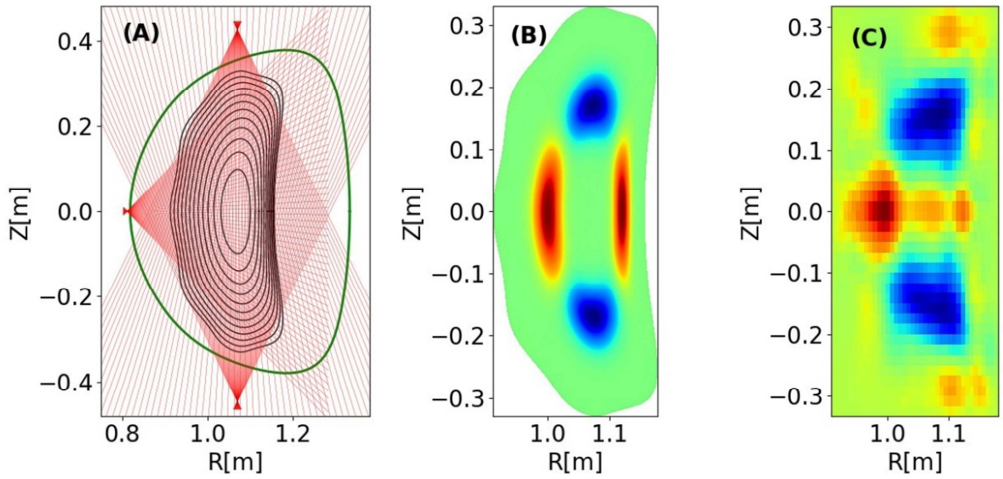


Figure 3: The viewing geometry (A), assumed emission profile of $m$=2/$n$=1 (B) and the reconstructed image(C) for DLC configuration of SX tomography system.

The dense LOS configuration (DLC) is devised for exploring the effect of the increase of lines of sights for the current design. The DLC includes three Soft X-ray arrays viewing the plasma in the poloidal plane at $\varphi$= 45$^{o}$ degree[9]. The three arrays are almost 90$^{o}$ degree apart as shown in figure 3(A). The difference between the current design and the DLC is the number of LOS per detector. DLC considers 60 LOS per detector thus effectively the system offers 60 x 3 = 180 LOS whereas in the current design only 60 LOS are present. The tomographic reconstruction with DLC for $m$=2/$n$=1 mode is shown in figure 3(C). The image is constructed with 40 x 40 pixel configurations. The image with DLC has not improved much although, the effective LOS has increased three times. The tomographic reconstruction with dense LOS configurations has failed to impress. The most probable reason for this failure lies in the fact that the LOS carries the maximum information of the plasma while traveling tangentially to the flux surfaces[10]. Thus just increasing the LOS may

increase the data points but it is not increasing the measurements tangential to the flux-surfaces.

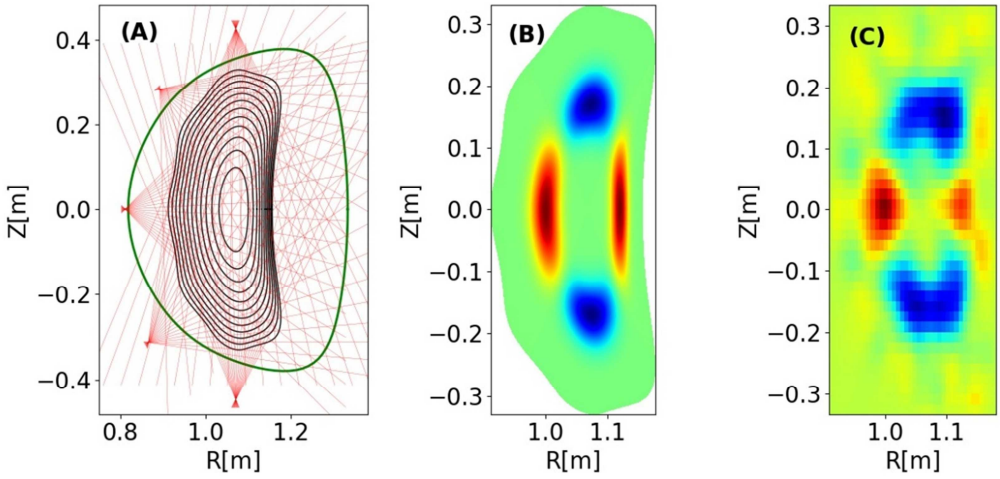


Figure 4: The viewing geometry (A), assumed emission profile of $m$=2/$n$=1 (B) and the reconstructed image(C) for five array configuration of SX tomography system.

Considering the mentioned fact a new configuration is devised in which two more arrays with the same detector system are added to the current soft X-ray tomographic diagnostic which is 90$^{o}$ degree poloidally apart. This configuration will offer 20 x 5 = 100 LOS effectively. The LOS is less than the DLC but it will be taking measurements with different poloidal locations honoring the fact that more number of LOS will be tangential to the flux surfaces. The viewing geometry is shown in figure 4(A). The two detectors are added between the three existing detector arrays. The assumed $m$=2/$n$=1 emission profile is shown in figure 4(B) and the reconstructed image is presented in figure 4(C). Comparing the results from the DLC, figure 3(C), and from the existing design figure 2(C), the reconstructed image quality has improved and a banana-shaped like structure is also realized for the negative portion of the mode structure, blue color. The reconstructed image, figure 4(C), has not reproduced the mode structure's positive part (with red color) satisfactorily. The mode structure positive portion is elongated horizontally in the reconstructed image, resulting in a triangle like shape.

Addition of the arrays have improved quality of the image.However, the mode structurehas not been realized efficiently. The inclusion of more arrays is one of the choices to improve further the quality of the image. Keeping that objective two more arrays are included in the system to investigate any possible improvement in the reconstructed image. The viewing geometry with seven arrays soft X-ray system is shown in figure 5(A). Effectively the system now holds 20 x 7 = 140 lines of sight at different poloidal locations. However it is still less than the DLC configuration. The assumed $m$=2/$n$=1 emission profile is shown in figure 5(B) and the reconstructed image is presented in figure 5(C).The inclusion of two more arrays, a total of seven arrays, has not significantly improved the quality of the mode structure image especially the positive portion, red color in figure 5(C). The negative portion, blue color, is almost similar to five arrays.

The reconstruction image for the mode $m$=3/$n$=2 with seven arrays is shown in figure 6(C) and the respective assumed profile is in figure 6(B). The reconstruction

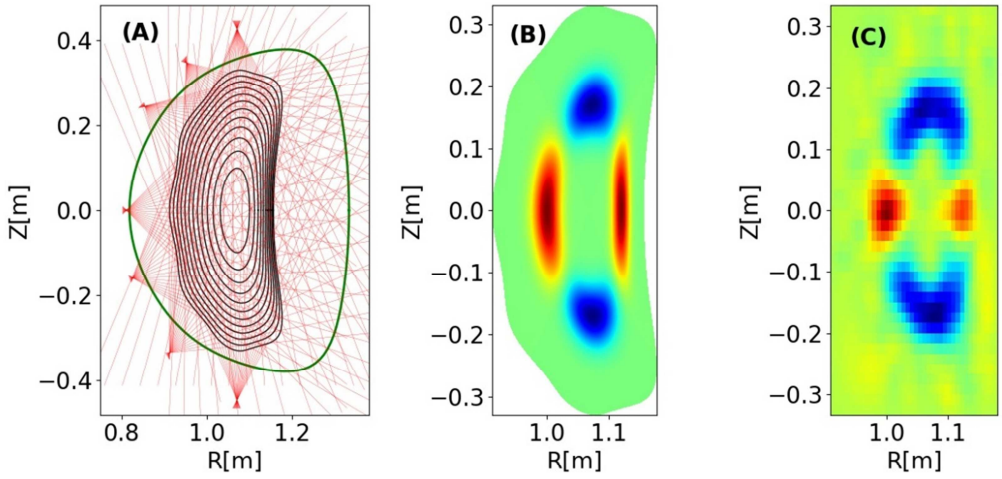


Figure 5: The viewing geometry (A), assumed emission profile of $m$=2/$n$=1 (B) and the reconstructed image(C) for seven array configuration of SX tomography system.

fails to reproduce the proper mode structures. However with seven arrays it is expected to have really good results for the mode $m$=3/$n$=2. The most likely reason is related to the flux –surface shape. The poloidal locations where the reconstruction

fails are subjected to the almost straight flux-surface shape and the LOS are not specifically tangential to them. Moreover there is a considerable amount of the flux compression at the inward location, above R = 1.01 *m*. This compression reduces the sensitivity of the tomographic diagnostic.

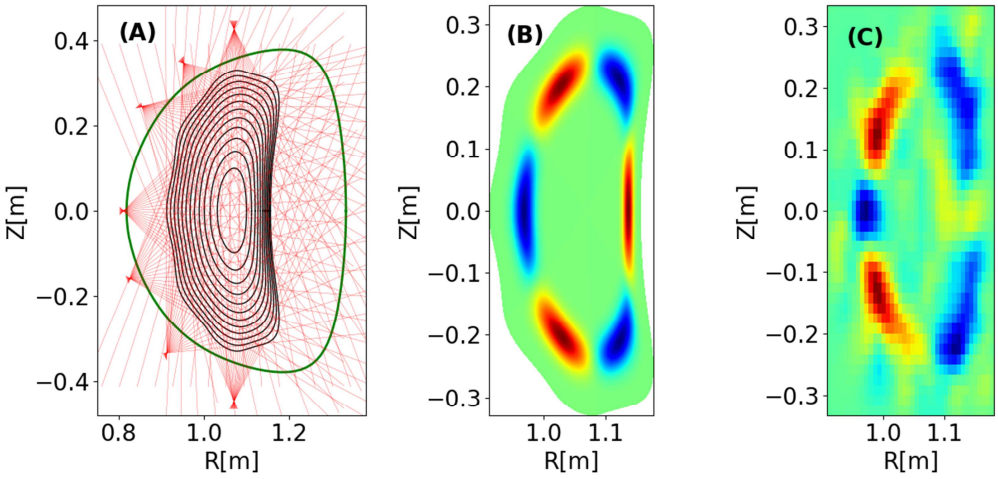


Figure 6: The viewing geometry (A), assumed emission profile of *m*=3/*n*=2 (B) and the reconstructed image(C) for seven array configuration of SX tomography system.

The modifications are subjected to physical limitations too, which are introduced by the machine design point of view. The toroidal location $\varphi = 45^{o}$ only have 5 ports in the poloidal plane. This means that only five arrays can be installed. Further installation of the detector arrays has to take unconventional approaches. The discussion in this section suggests that modifications in soft X-ray tomographic system for H-J are constrained with respect to the device as well as from the plasma shape. The reconstructed images can only be improved up to some extent with five arrays. The best possible results here, do not ensure a proper study of the mode structures like *m*=4/*n*=2 or *m*=5/*n*=2 which are often reported for the H-J plasma[11]. Thus a new design is required for the soft X-ray tomographic system.

## 4. New Design

The current design of the soft X-ray tomographic diagnostic is constrained and modifications suggested in the previous section partially improves the reconstructed image quality. Therefore a new design for the tomography diagnostic has to be devised to overcome present constraints. In this section a designs is discussed, based on the perpendicular viewing tomography, PVT, (inline to the current viewing scheme).

### 4.1 Design Details

The modification suggested in section 3 are greatly influenced by the flux-surface shape, which are more straight and somewhat compressed on inward side, see figure 7(B). With the intention of avoiding such situation the flux-surfaces, provided by VMEC code[12], for the Heliotorn J device, are scanned for identifying uniform flux-surfaces without or least straightness in the shape. The scanning suggests that at $\varphi = 0^{o}$ degree the flux surfaces are uniform and minimum straightness is observed as shown in figure 7(C). The absense of flux copression and striaghtness ensures tomographic diagnostic's constant sensitivity across the poloidal plane at this location. Considering a favorable flux-surface shape, toroidal location $\varphi = 0^{o}$ degree is

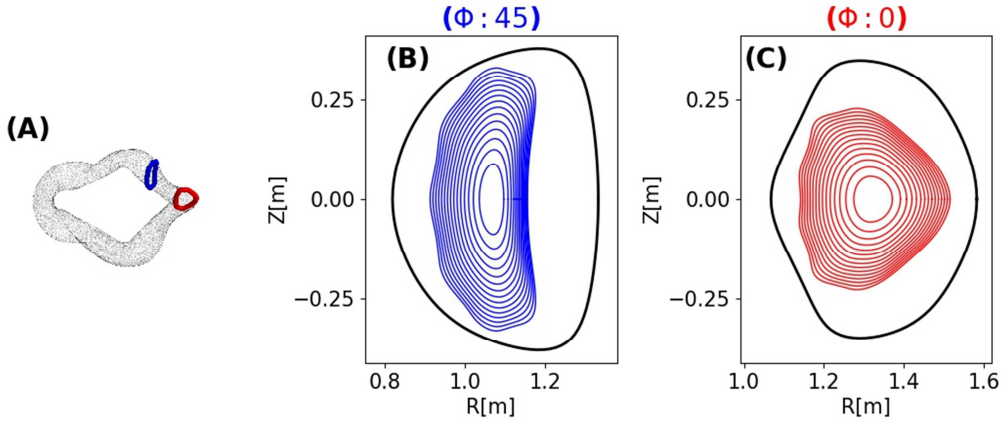


Figure 7: The two location $\varphi = 0^{o}$ (red) and $\varphi = 45^{o}$ (blue) (A) and respective flux surfaces shape $\varphi = 45^{o}$ (B) and $\varphi = 0^{o}$ (C).

fixed for the soft X-ray tomographic system installation.

The second component of the new design is the selection of the number of soft X-ray detector arrays. As seen in previous section inclusion of arrays improves the reconstructed image quality, however, there is a physical limit/constraint over the inclusion of the detector arrays. One such limit/constraint is the availability of the ports at the respective poloidal location. The H-J vacuum vessel at $\varphi = 0^{o}$ posses only is five ports. Via some special arrangement, like extended in-vessel arm can enable more than five detectors hosting in the tomographic diagnostic system. The scope of this study does not include the design aspect of such a mechanical arrangement. The study only concentrates on the reconstructed image improvement due to the inclusion of more arrays, therefore the maximum number of arrays which the design can host is still open . However 5 array combination is at least possible without any special arrangement.

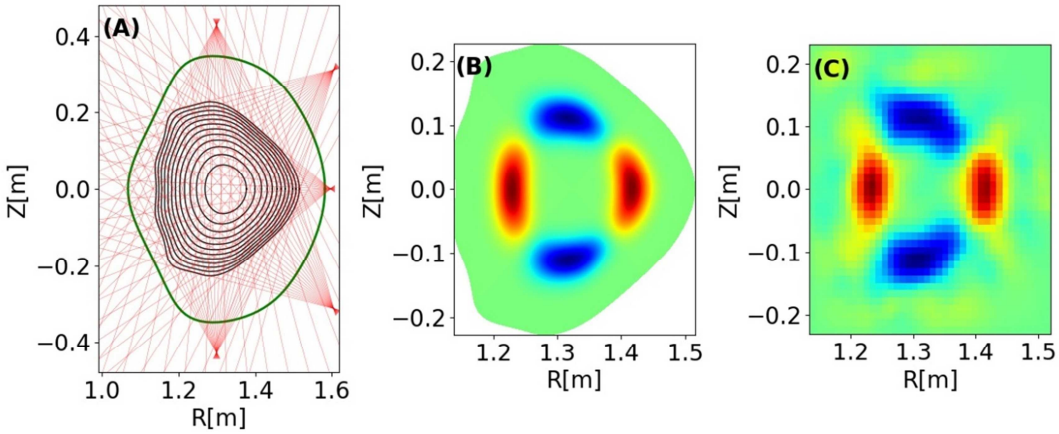


Figure 8: The viewing geometry (A), assumed emission profile of $m$=2/$n$=1 (B) and the reconstructed image(C) for five array configuration of SX tomography system.

The viewing geometry with five detector arrays, 20 x 5 = 100 LOS, is shown in figure 8(A). The assumed *m*=2/*n*=1 emission profile is shown in figure 8(B) and the reconstructed image is presented in figure 8(C). The image quality with five detectors is far better in comparison with reconstructed images including the modification for the current diagnostic system suggested in the previous section, see figure 6(C) and figure 5(C). Due to the uniform and compression-free flux – surfaces, the positive and the negative portions of mode structures are clearly visible along with the recognizable banana shape of the mode structure.

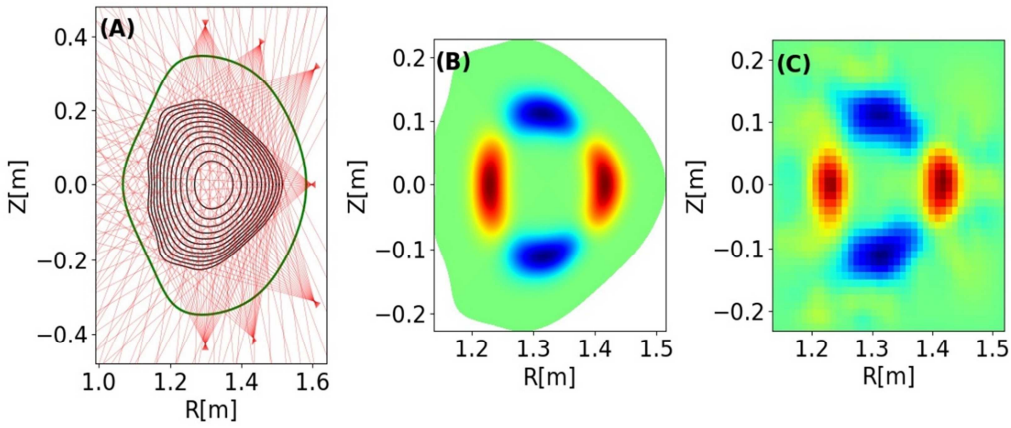


Figure 9: The viewing geometry (A), assumed emission profile of *m*=2/*n*=1 (B) and the reconstructed image(C) for seven array configuration of SX tomography system.

The Heliotorn J plasma contains higher poloidal mode structure like *m*=4/*n*=2 or *m*=5/*n*=2 and reconstruction of such structures required more detector[11]. The perpendicular viewing based new design for H-J soft X-ray tomographic diagnostic system should contain more detector arrays in order to recover such mode structures. An advanced design concept is laid for H-J with seven detector arrays at φ= $0^{o}$ degree. The viewing geometry, 20x 7=140 LOS, is shown in figure 9(A) with assumed *m*=2/*n*=1 emission profile figure 9(B) and the reconstructed image in figure 9(C), respectively.The reconstruction is fairly good in comparison to the current location.The image quality has not improved significantly from the five array configuration, figure 8(C). The reconstruction for *m*=3/*n*=2 with seven array

configuration is shown in figure 10. The mode structures are clearly visible. This situation is far better than the 7 even array configuration in figure 6(C), where the identification of such mode was not at all possible. The absence of straight flux-surfaces and a proper number of measurement tangential to the flux surfaces enabled a clear reconstruction for heliotron J mode structures. The new design for the soft X-ray tomography system for the Heliotorn J machine should include seven or more arrays perpendicularly viewing the plasma at the toroidal location $\varphi = 0^{o}$ degree.

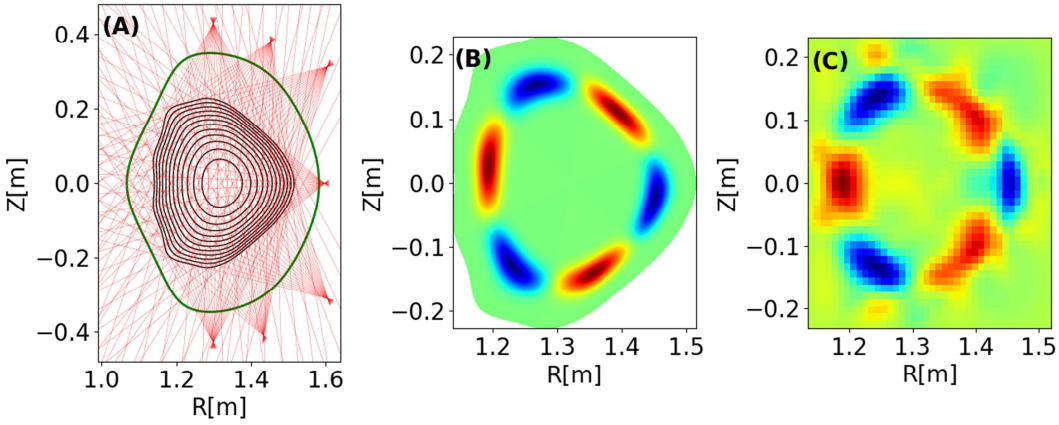


Figure 10: The viewing geometry (A), assumed emission profile of $m$=3/$n$=2 (B) and the reconstructed image(C) for seven array configuration of SX tomography system.

Considering the available ports at this location the seven detector array design is not directly possible. One of the bright ideas to have seven arrays for observations will be the extended arm entering the vessel from one port holding the detector arrays. In this situation more than seven arrays can be accommodated. However the plasma to detector distance will be different and in order to have a proper plasma viewing the pinhole size has to be judiciously decided. In case of more than seven arrays higher mode number can be realized in the tomographic reconstruction.

## References

[1] Terasaki N, Hosoda Y, Teranishi M and Iwama N 1997 Linear algebraic algorithms for high speed and stable reconstruction of plasma image *Fusion Eng. Des.* **34**–**35** 801–4

[2] Iwama N, Yoshida H, Takimoto H, Shen Y, Takamura S and Tsukishima T 1989 Phillips–Tikhonov regularization of plasma image reconstruction with the generalized cross validation *Appl. Phys. Lett.* **54** 502–4

[3] Wingen A, Shafer M W, Unterberg E A, Hill J C and Hillis D L 2015 Regularization of soft-X-ray imaging in the DIII-D tokamak *J. Comput. Phys.* **289** 83–95

[4] Gao J M, Liu Y, Li W, Lu J, Dong Y B, Xia Z W, Yi P and Yang Q W 2013 Minimum Fisher regularization of image reconstruction for infrared imaging bolometer on HL-2A *Rev. Sci. Instrum.* **84** 093503

[5] Ertl K, Linden W von der, Dose V and Weller A 1996 Maximum entropy-based reconstruction of soft X-ray emissivity profiles in W7-AS *Nucl. Fusion* **36** 1477–88

[6] Livesey A K and Brochon J C 1987 Analyzing the distribution of decay constants in pulse-fluorimetry using the maximum entropy method. *Biophys. J.* **52** 693–706

[7] Iwama N, Hosoda Y, Kitahashi K, Sato J and Kosugi T 2005 Maximum Entropy Algorithm of Image Reconstruction by SMW Formula and Its Application to Satellite Yohkoh Hard X-ray Telescope Imaging *A Bull. Daido Tech. Coll.* **41** 105–21

[8] Ming T, Ohdachi S and Suzuki Y 2013 Estimate of the deposition profile of carbon pellets using a high-speed VUV imaging system in the LHD *Plasma*

*Sci. Technol.* **15** 1178–83s

[9] Purohit S, Suzuki Y and Yamamoto S 2017 Soft X-ray tomographic reconstruction of Heliotron-J plasma for the study of Magnetohydrodynamics Equilibrium and Stability *26th International Toki Conference (ITC-26) 5-8 December, Toki, JAPAN* (Toki) pp P1-37

[10] Goeler S von, Kaita R, Bitter M, Fuchs G, Poier M, Bertschinger G, Koslowski H R, Toi K, Ohdachi S and Donné A 1999 High speed tangential soft x-ray camera for the study of magnetohydrodynamics instabilities *Rev. Sci. Instrum.* **70** 599

[11] Yamamoto S, Nagasaki K, Suzuki Y, Mizuuchi T, Okada H, Kobayashi S, Blackwell B, Kondo K, Motojima G, Nakajima N, Nakamura Y, Nührenberg C, Torii Y, Watanabe S and Sano F 2007 Observation of Magnetohydrodynamic Instabilities in Heliotron J Plasmas *Fusion Sci. Technol.* **51** 92–6

[12] Hirshman S P and Whitson J C 1983 Steepest-descent moment method for three-dimensional magnetohydrodynamic equilibria *Phys. Fluids* **26** 3553